Targeted photoredox catalysis in cancer cells

Huaiyi Huang, Samya Banerjee, Kangqiang Qiu, Pingyu Zhang, Olivier Blacque, Thomas Malcomson, Martin J Paterson, Guy J Clarkson, Michael Staniforth, Vasilios G Stavros, et al.

Targeted photoredox catalysis in cancer cells

Huaiyi Huang[1,2], Samya Banerjee[2], Kangqiang Qiu[3], Pingyu Zhang[4], Olivier Blacque[5], Thomas Malcomson[6], Martin J. Paterson[6], Guy J. Clarkson[2], Michael Staniforth[2], Vasilios G. Stavros[2], Gilles Gasser[7]*, Hui Chao[3]* and Peter J. Sadler[2]*

[1]School of Pharmaceutical Science (Shenzhen), Sun Yat-sen University, Guangzhou, 510275, China

[2]Department of Chemistry, University of Warwick, Coventry, CV4 7AL, UK

[3]MOE Key Laboratory of Bioinorganic and Synthetic Chemistry, School of Chemistry, Sun Yat-sen University, Guangzhou, 510275, China

[4]College of Chemistry and Environmental Engineering, Shenzhen University, Shenzhen, 518060, China

[5]Department of Chemistry, University of Zurich, Zurich, CH-8057, Switzerland

[6]School of Engineering and Physical Sciences, Heriot-Watt University, Edinburgh, EH4 4AS, UK

[7]Chimie ParisTech, PSL University, CNRS, Institute of Chemistry for Health and Life Sciences, Laboratory for Inorganic Chemical Biology, Paris, F-75005, France

These authors contributed equally: Huaiyi Huang and Samya Banerjee

Hypoxic tumours are a major problem for cancer photodynamic therapy. Here we show that photo-redox catalysis can provide an oxygen-independent mechanism of action to combat this problem. We have designed a highly oxidative Ir(III) photo-catalyst, $[Ir(ttpy)(pq)Cl]PF_6$ ([**1**]PF6, ttpy = 4'-(p-tolyl)-2,2':6',2''-terpyridine, pq = 3-phenylisoquinoline), which is photo-toxic towards both normoxic and hypoxic cancer cells. Complex **1** photo-catalytically oxidizes nicotinamide adenine dinucleotide (NADH), an important coenzyme in living cells, generating NAD$^{\bullet}$ radicals with high turnover frequency in biological media. Moreover, complex **1** and NADH synergistically photo-reduce cytochrome c under hypoxia. Density

functional theory calculations reveal π-stacking in adducts of **1** and NADH, facilitating photo-induced single electron transfer. In cancer cells, **1** localizes in mitochondria and disrupts electron transport via NADH photo-catalysis. Upon light irradiation, **1** induces NADH depletion, intracellular redox imbalance, and immunogenic-apoptotic cancer cell death. This photo-catalytic redox imbalance strategy offers a new approach for efficient cancer phototherapy**.**

Platinum compounds are the most widely used anticancer drugs in the clinic[1]. However, new generations of metal-based anticancer agents are urgently needed to combat drug resistance and reduce side-effects[2,3]. Photo-activated metal complexes can provide both temporal and spatial control over drug activation and show remarkable potential for cancer treatment[4-8]. Tin, lutetium, palladium and ruthenium based photosensitizers (PSs) are, or were, currently in clinical trials for cancer photodynamic therapy (PDT)[9,10]. The catalytic nature of PDT can achieve high therapeutic efficacy at low doses[11], and, in general, does not show cross resistance to chemotherapy, helpful for overcoming drug resistance[12]. However, a few cases of clinical resistance to PSs are emerging[13-21].The mechanisms of PDT resistance include hypoxia[13], detoxification by intracellular antioxidant systems,[14,15] induction of stress response genes,[16-20] and drug efflux by P-glycoprotein[21]. These considerations indicate the urgency of developing new generations of PSs and novel mechanisms of action (MOA) for cancer phototherapy. The high dependence of the MOA of PDT on oxygen restricts its application, since cancer cells grow mostly under hypoxia[22]. We have therefore investigated novel PSs with new MOAs against hypoxic cancer cells.

Although most tumours adopt a Warburg-type glycolytic metabolism, Reactive Oxygen Species (ROS) released from the mitochondrial electron transport chain (ETC) are essential for cell proliferation and redox regulatory functions of cancer cells under hypoxia[23]. The electron source in the ETC is 1,4-dihydronicotinamide adenine dinucleotide (NADH, Fig. 1a), which participates in the maintenance of the intracellular redox balance and as a coenzyme in >400 oxidoreductases[24]. We hypothesise that selective induction of NADH depletion and of ETC disruption in cancer cells may destroy the intracellular redox balance

and kill cancer cells under hypoxia.

Photo-catalysts which induce single electron transfer (SET) between substrates have achieved great success in organic synthesis[25]. It is notable that most reported photoredox catalysis has been carried out in degassed organic solvents[26]. An oxygen-independent MOA is appealing for NADH photo-catalysis in hypoxic cancer cells. However, strong triplet excited-state quenching by water and oxygen severely limits the application of traditional photo-catalysts in biological systems[27].

Here we have synthesised and characterised a novel stable iridium photo-catalyst (**1**, Fig. 1b) with an unusually high excited state reduction potential compared to common PSs[25]. Strikingly, upon light irradiation in biological media, complex **1** shows more than two orders of magnitude higher NADH oxidation turnover frequency (TOF) than organometallic half-sandwich catalysts[28]. Moreover, **1** can photo-catalyse cytochrome c (cyt c) reduction in the presence of NADH under hypoxia. We have carried out detailed experimental and computational studies on photo-catalytic NADH oxidation in aqueous media, involving the trapping of $NAD^{\bullet}$ radicals and their characterisation. In addition, complex **1** targets mitochondria in cancer cells, and, importantly, shows almost equivalent photo-cytotoxicity under normoxia and hypoxia, as well as low toxicity to unirradiated normal cells.

Results

Photosensitizer design and characterisation

Complex **1** was characterised by analytical and spectroscopic data, and x-ray crystallography (Fig. 1c, Supplementary Tables 1, 2). Ir(III) photoredox catalysts with bidentate ligands often exist as a mixture of enantiomers[29]. The incorporation of tridentate ligands can avoid chirality[30], as in the present case (Fig. 1c). Density functional theory (DFT) calculations confirmed that the

trans C-Cl isomer found in the crystal structure is 33.5 kJ mol^{-1} more stable than the *cis* C-Cl isomer. Complex **1** showed absorption between 350-480 nm (Supplementary Fig. 1), which matched well with spectra calculated by time-dependent DFT (TD-DFT; Supplementary Fig. 2), with low-lying metal-to-ligand charge-transfer states (MLCT, Supplementary Table 3).

The phosphorescence of complex **1** was sensitive to solvent polarity (Supplementary Fig.3, Supplementary Table 4) with emission at ca. 562 nm similar to the calculated data (567 nm, Supplementary Table 3) at 293 K. Moreover, oxygen strongly influenced the phosphorescence intensity and lifetime of **1** (Supplementary Figs. 4,5, Supplementary Table 4), being longer in acetonitrile (743.7/1390.3 ns, air/N_2) than in phosphate buffered saline (PBS, 330.8/382.3 ns, air/N_2). The lowest energy singlet excited state S_1 arises from LUMO ← HOMO excitation and showed both ligand-to-ligand charge-transfer and MLCT character (Supplementary Table 3, Supplementary Fig. 6). Upon light excitation, the excited triplet transition "hole" (Fig. 2a) is localised on the π-system of the C^N ligand, while the "particle" is localised on the N^N^N ligand. In addition, complex **1** exhibited strong two-photon absorption (TPA) (Fig. 2b), observed with a maximum at ca. 760 nm (Supplementary Fig. 7) and a two-photon absorption cross section of 160 Goeppert-Mayer (GM).

Ideally, efficient photo-catalytic drugs should exhibit high dark- and photo-stability. Complex **1** showed excellent stability in both organic solvents, e.g. DMSO (Supplementary Fig. 8), RPMI-1640 cell culture medium (Fig. 2c), and human serum (Supplementary Fig. 9) on prolonged incubation. Additionally, **1** also exhibited no photo-degradation under 463 nm blue-light irradiation in PBS (Fig. 2d).

Cyclic voltammetry revealed a significantly different redox behavior in the ground and excited states of **1** (Supplementary Table 5). The excited-state reduction potential of **1** ($E_{1/2}^{*III/II}$ = +1.22 V vs SCE) is higher than for reported Ru(II) or Ir(III) photocatalysts (Supplementary Fig. 10, Supplementary Table 5)[25]. DFT calculations also confirmed that the triplet excited state of **1** switched character with the ground state (Supplementary Fig. 11) in

terms of reductant-to-oxidant behavior (Supplementary Table 6), and thus is a strong excited-state oxidant (Supplementary Table 7).

Photo-catalytic oxidation of NADH under normoxia

The catalytic photo-oxidation of NADH (3 mM) by **1** (0.25 mM) in $H_2O/D_2O/CD_3OD$ (0.5/49.5/50, v/v, 4 mM NaCl) was monitored by ^1H NMR spectroscopy at 298 K. In the dark, the sample remained unchanged for 24 h. In contrast, ca. 95% of the NADH was oxidised to NAD^+ after irradiation (463 nm, 30 min), while **1** remained intact (Supplementary Fig. 12).

The photo-catalytic efficiency of **1** (6 μM) towards NADH (240 μM) in PBS was quantified by UV-vis spectroscopy (Supplementary Fig. 13). Upon photoirradiation (463 nm) in air, the absorbance of NADH at 339 nm decreased gradually (Fig. 3a), and the conversion of NADH to NAD^+ was confirmed by mass spectrometry (Supplementary Fig. 14). A plot of lnA_{339} versus time revealed first-order kinetics with a rate constant k of 1.77×10^{-2} min^{-1} (Supplementary Fig. 15). The highest observed NADH oxidation turnover number (TON) was 50.2 with a turnover frequency (TOF) of 100.4 h^{-1} (Supplementary Table 8), much higher than the reported (non-photoactivated) Ir(III) half-sandwich catalyst [(η^5-Cp^{xbiph})Ir(phpy)py]PF_6 (TON=7.6 after 20 h)[28]. Moreover, complex **1** was stable during long-term photo-catalysis (2 h, Supplementary Fig. 16). Importantly, the reaction rate was not affected by NaN_3 ($^1O_2$ scavenger), and was similar in deionised water (Supplementary Fig. 13). After irradiation of **1** and NADH in PBS in air, H_2O_2 was generated as detected by peroxide detection strips (Fig. 3a), and the pH of the reaction solution increased by ca. 2 units (Supplementary Fig. 17).

A Stern−Volmer titration[31] was used to study the mechanism of the photcatalytic oxidation of NADH. When the NADH concentration was increased, the phosphorescence intensity of **1** decreased gradually with a dynamic quenching rate coefficient of 6.8×10^6 (Fig. 3b). The phosphorescence lifetime of **1** in air-saturated PBS (330 ns) decreased by ca. 50% after addition of NADH (171 ns, Supplementary Fig. 5).

Electron paramagnetic resonance (EPR) was used to trap radical intermediates during photo-catalytic oxidation of NADH (Fig. 3c) using 5-(2,2-dimethyl-1,3-propoxycyclo-phosphor-yl)-5-methyl-1-pyrroline-N-oxide (CYPMPO) as the spin trap[32]. In the presence of CYPMPO, a carbon-centred NAD$^{\bullet}$ radical was detected as CYPMPO-NAD together with CYPMPO-CH_3 after irradiation in PBS/methanol (1:1 v/v, 463 nm, 10 min, 293 K). The $^{\bullet}CH_3$ radical was generated by a photo-reaction between H_2O_2 and methanol (Supplementary Fig. 18). Singlet oxygen production was also detected by EPR, and the quantum yield in acetonitrile (0.71) was 7x higher than in PBS (Φ = 0.11; Supplementary Fig. 19). This is due to the longer lifetime of the triplet state in acetonitrile compared to PBS, typical for metal complexes having a triplet excited state[7,9].

Molecular adducts of NADH and excited-state ***1** were investigated by DFT calculations. Stable minima were observed for structures with NADH clamped by π-π interactions over the triplet hole orbital localized on the pq ligand (Fig. 3d), and over the triplet particle orbital localized on the ttpy π-system (Fig. 3e), structures which would facilitate electron transport from NADH to ***1**.

Photoreduction of cytochrome c under hypoxia

Under nitrogen, the photo-catalytic activity of **1** decreased significantly compared to under air (TON = 3.8, Supplementary Fig. 20) due to the absence of a terminal electron acceptor. In the mitochondrial electron transport chain (ETC), the 12.3 kDa heme protein cyt c transfers electrons between Complex III (Coenzyme Q-cyt c reductase) and Complex IV (cyt c oxidase)[33]. Release of cyt c from the mitochondria into the cytoplasm induces cell apoptosis[34].

The oxidation state of cyt c (Fe^{2+}/Fe^{3+}) can readily be monitored by the β and α bands at 520 and 550 nm, respectively[35]. NADH (50 μM) slowly reduced Fe^{3+}-cyt c (11.2 μM; 293 K, Supplementary Fig. 21). The reaction was slightly accelerated upon 463 nm light irradiation (Supplementary Fig. 21) with low TOF (2.8 h^{-1}, Supplementary Fig. 22). In the absence of NADH, **1** (0.6 μM) did not reduce Fe^{3+}-cyt c, even under light irradiation (Supplementary Fig. 21). After adding NADH, the rate of photo-reduction of Fe^{3+}-cyt c increased significantly

(Fig. 3f), with the TOF increasing to 16.7 h^{-1}. When CYPMPO was added to trap NAD$^{\bullet}$, the reduction rate decreased (Supplementary Figs. 21, 22), indicating that NAD$^{\bullet}$ was involved in Fe^{3+}-cyt c photoreduction.

Photo-cytotoxicity and cell death mechanism

The dark- and photo-cytotoxic activity of **1** was investigated against a range of cancer cell lines, and normal cells MRC-5 (human lung fibroblasts) and LO2 (human hepatocyte cell line), (Supplementary Figs. 23-26, Supplementary Table 9). Cisplatin and 5-aminolevulinic acid (5-ALA) were used as controls (Supplementary Fig. 24). Low dark toxicity was observed for both A549 human lung carcinoma (IC_{50} 43.6 μM) and MRC-5 cells (43.2 μM) after 2 h drug exposure and 46 h recovery. Complex **1** also showed low dark toxicity towards normal LO2 human hepatocyte cells (IC_{50} = 32 μM). For photo-cytotoxicity screening, A549 cells were treated with **1** for 2 h, washed, placed in fresh medium, then irradiated with blue light for 30 min under normoxia (20% O_2, 465 nm, 8.9 J/cm^2) or hypoxia (1% O_2, 450 nm, 10 J/cm^2), and left for 46 h to recover. Under normoxia, **1** (1.6 μM) exhibited high photo-cytotoxicity with a photo-cytotoxicity index (PI = dark IC_{50}/light IC_{50}) of 27.2. Interestingly, **1** exhibited similar photo-cytotoxicity (dark/light 42.5/2.3 μM, PI = 18.5) under hypoxia. In addition, we found that complex **1** is active against NCI-H460 (lung), HeLa (cervix), Hep G2 (liver) and SGC-7901 (gastric) cancer cell lines upon light irradiation under both 20% and 1% oxygen concentrations with sub-micromolar IC_{50} values (Supplementary Table 9, Supplementary Fig. 23). However, the clinical pro-drug 5-ALA, a precursor of the photosensitizer protoporphyrin, was totally inactive under hypoxia after irradiation (Supplementary Table 9, Supplementary Fig. 24). The photo-cytotoxicity of complex **1** under normoxia was reduced in the presence of NaN_3 ($^1O_2$ scavenger) and D-mannitol (hydroxyl radical scavenger) for A549 cells. However, these ROS inhibitors had no significant influence on photo-cytotoxicity under hypoxia (Supplementary Fig. 25, Supplementary Table 9), suggesting a different cellular response to photo-catalysis. It should be noted that cytotoxicity experiments are very sensitive to experimental conditions, including incubation time, irradiation time, light dose, and mode of treatment. Changes in the cytotoxicity of **1,**

cisplatin and 5-ALA were observed with change in the incubation time and mode of treatment. As most of complex **1** was taken up by the cells within 2 h of incubation time, in all our photocytotoxicity experiments, 2 h of incubation with **1** was used prior to photoirradiation.

To investigate the phototherapeutic efficiency on a solid tumour model, the photocytotoxicity of **1** towards A549 lung cancer multicellular spheroids (MCS)[36] of diameter ca. 800 μm was studied (Supplementary Fig. 27, Supplementary Table 9). Remarkably, using two-photon red light irradiation (760 nm, 12 J/cm^2), **1** gave a PI of 9.7 (dark/light 12.6/1.3 μM). Under the same conditions, 5-ALA and cisplatin did not exhibit any significant photocytotoxicity[37].

Inductively coupled plasma-mass spectrometry (ICP-MS) confirmed the high cellular uptake of **1** (162 ± 6 ng Ir × 10^6 cells, 5 μM treatment, 2 h,). Furthermore, co-localization imaging and quantification by ICP-MS[38] (Fig. 4a and Supplementary Fig. 28) showed that ca. 90% of Ir from **1** localized in mitochondria. Importantly, pulsed laser phosphorescence lifetime imaging[39] (Fig. 4b) revealed that **1** has an extremely long phosphorescence lifetime in A549 cancer cells (1100 ns, Supplementary Fig. 29).

Next, we investigated photo-induced intracellular NADH depletion in A549 cells. Under normoxia, the intracellular NADH concentration was unaffected after incubation with increasing concentrations of **1** in the dark (Fig. 4c). Upon light irradiation, **1** induced a dramatic depletion in NADH (ca. 4x at 2 μM) and decreased the concentration of adenosine triphosphate (ATP) (Fig. 4d). In addition, the irradiated cells lost their ability to generate formazan from 3-(4,5-dimethylthiazol-2-yl)-2,5-diphenyltetrazolium bromide (MTT), a reaction which requires NAD(P)H-dependent oxidoreductase enzymes (Supplementary Fig. 30)[40].

We also explored cellular oxidative stress induced by **1**. After light irradiation, a strong green fluorescence was observed from the ROS probe DCFH-DA under both normoxia and hypoxia (Supplementary Fig. 31). A549 lung cancer multicellular spheroid models (ca. 800 μm in diameter) showed that ROS were generated only in the outer regions of the MCS after irradiation with 760 nm two-photon light (Supplementary Fig. 32), indicating the formation

of a hypoxic core in the internal region of the spheroids. These results suggested that diffusible ROS species[41] such as H_2O_2 were generated. Indeed, the intracellular H_2O_2 concentration increased ca. 2.5x (Fig. 4e) compared to unexposed cells. Moreover, the cellular H_2O_2 concentration was significantly lower in the presence of N-acetyl-L-cysteine (Fig. 4f), a known ROS scavenger[42].

A decrease in the mitochondrial membrane potential (MMP) was observed in **1**-treated A549 cells after irradiation under both normoxia and hypoxia (Supplementary Figs. 33, 34), indicating disruption of the mitochondrial ETC[43]. However, **1** did not induce any significant change in MMP in MRC-5 normal cells in the dark. Furthermore, staining of cells with the green fluorescent FTIC-Annexin V conjugate was observed (Supplementary Fig. 35), indicating cell apoptosis. Moreover, these cells also showed red fluorescence on co-staining with propidium iodide (PI). Apoptotic cells would not allow PI to enter cells, and hence cell death may involve an immunogenic-apoptotic mechanism[44]. We also performed cell membrane calreticulin immunofluorescence and an Enzyme-linked Immunosorbent Assay (ELISA) for high mobility group box 1 protein (HMGB1) (Supplementary Fig. 36). Calreticulin transfer to the outer cell membrane and release of HMGB1 are well known markers of immunogenic cell death[44]. Calreticulin transfer to the outside of the cell membrane, detected by Alexa Fluor 488 linked calreticulin antibody, was observed in the **1**-treated A549 cancer cells upon light irradiation. We also detected release of HMGB1 at the same time. Both these findings, along with the Annexin V /PI assay, confirmed that complex **1** induces immunogenic-apoptotic cell death upon light irradiation.

Discussion

Catalytic metallodrugs activated at low doses have the potential to increase the efficacy of cancer therapy[45]. However, controlling catalytic activity in complicated tissue and cell environments as well as selectivity between normal and cancer cells is extremely challenging. In contrast to chemotherapy, PDT provides light-directed cancer-cell-targeted treatment and can avoid drug resistance[12]. However, cancer cells grow under hypoxia and thus the oxygen-

dependent MOA of PDT remains a problem, as is photo-degradation of photosensitisers[46]. Hence we have now designed a stable photo-redox catalyst with an oxygen-independent MOA as a new strategy to overcome these problems.

Our photo-redox catalytic approach recognises two key vulnerabilities in cancer cells. Firstly, the mitochondrial ETC contributes to tumourigenic phenotype amplification, cell proliferation, and especially cell survival under hypoxia[23]. Secondly cancer cells are under constant oxidative stress[47]. Coenzyme NADH not only provides electrons for the ETC, but also maintains the cellular redox balance and participates in enzyme reactions[24]. Photo-catalytic NADH depletion and ETC disruption can therefore achieve selective attack on cancer cells and high anticancer activity under hypoxia.

The novel octahedral Ir(III) photocatalyst **1** was synthesised as a single isomer driven by the tridentate ligand ttpy. The X-ray structure and DFT calculations show formation of the *trans* C-Cl isomer, with the negatively-charged C ligand exerting a strong *trans* influence on the Ir-Cl bond. The special ligand coordination architecture tunes the Ir(III) coordination sphere, and ensures well-partitioned HOMO and LUMO within the structure, thus significantly enhancing dark- and photo-stability[48]. In contrast, the Ir(III) photo-catalyst $[Ir(ppy)_2(bpy)]^+$ (ppy = 2-phenylpyridine, bpy = 2,2'-bipyridine) is not photo-stable and undergoes photodecomposition during long-term light irradiation[49]. Moreover, the presence of a single cyclometalated chelated ligand decreases the electron density at Ir(III), thereby significantly increasing the excited-state reduction potential of **1**.

NADH oxidation is usually associated with one-step hydride transfer to substrates, as observed for example in transfer hydrogenation using Cp*-iridium(III) catalysts[28]. However, initial one-electron transfer is also known[50], e.g. in thermal reactions of $[Ru(bpy)_3]^{3+}$ with NADH analogues BNAH (1-benzyl-1,4-dihydronicotinamide)[51], and UVA-induced electron transfer from NADH to generate superoxide for DNA cleavage[52]. Other reports have also used NADH as an electron donor in photosensitisation[53]; however, electron transfer between a PS and NADH has been little investigated. Our DFT calculations reveal the formation of "clamped" π-π adducts between excited-state ***1** and NADH which can facilitate photo-

induced single electron transfer. As a result, complex **1** achieves high TOF for catalytic NADH oxidation (100.4 h^{-1}) on light irradiation.

The mechanism of the photo-catalytic oxidation of NADH is consistent with the reductive quenching cycle shown in Figure 5. Upon light excitation, the highly oxidative excited state species ***1**(Ir^{III}) extracts an electron from 1,4-dihydronicotinamide, forming a highly reductive **1**(Ir^{II}) species and $NADH^{+\bullet}$ radicals. $NADH^{+\bullet}$ readily deprotonates to generate the neutral carbon-centred $NAD^{\bullet}$ radical. Under normoxia (Figure 5a), oxygen oxidises **1**(Ir^{II}) to form superoxide radicals and regenerates **1**(Ir^{III}), completing the photo-catalytic cycle. The superoxide radical extracts an electron from $NAD^{\bullet}$ and consumes two protons from the medium as evidenced by the pH increase, forming H_2O_2 and NAD^{+}. Under hypoxia, Fe^{3+}-cyt c is a terminal electron acceptor (Figure 5b). In previous reports, Ru(II)/Ir(III) bis-terpyridyl complexes and EDTA radicals exhibited a synergistic effect on Fe^{3+}-cyt c reduction[54], whereas here, we discovered that NADH can also serve as a biological electron donor in the synergistic reduction of Fe^{3+}-cyt c by complex **1** or the related complex $[Ir(tpy)_2]^{3+}$ (Supplementary Fig. 22). Thus, we confirmed that photo-reduction of Fe^{3+}-cyt c can arise from the synergistic action of $NAD^{\bullet}$ radicals and the highly reducing Ir^{II} species in a deoxygenated environment. This pathway provides a mechanism for oxygen-independent NADH depletion with its downstream effects on a wide variety of cellular redox enzymes and pathways, and plays an important role in hypoxic photoredox catalysis in cancer cells.

Although mitochondria are dysfunctional in cancer cells, ROS released from the ETC under hypoxia are essential for cancer cell survival and redox regulatory functions[55]. In our system, complex **1** induces significant NADH depletion and ETC disruption only in irradiated cancer cells, as indicated by the MMP decrease under both normoxia and hypoxia. Moreover, ROS generation in cancer cells indicates oxygen consumption during photo-catalysis by **1** which can cut off essential mitochondrion-to-cell redox communication for cell survival under hypoxia[56]. These events lead to the induction of cell apoptosis and necrosis by complex **1**, features of immunogenic apoptosis[57]. Calreticulin immunofluorescence and HMGB1 ELISA assays confirmed this hypothesis[44]. Immunogenic cell death provides a

potentially powerful strategy for anticancer therapy[58], reinstating the body's defense against cancer.

In addition, both DFT calculations and experimental data reveal strong near infrared two-photon absorption of **1**, and we have demonstrated promising phototherapeutic effects on A549 multicellular lung cancer spheroids. These one-photon and two-photon light activation properties of **1** will facilitate a broad application from superficial lesions to solid tumours.

Conclusions

We report for the first time both aqueous and in-cell photo-catalytic oxidation of coenzyme NADH by a metal complex, with a very high TOF. The novel octahedral cyclometalated Ir^{III} photoredox catalyst, complex **1**, is highly photostable with a long phosphorescence lifetime. This catalyst, with its unusually high excited state reduction potential, not only generates $NAD^{\bullet}$ radicals, but also perturbs electron transfer pathways in mitochondria by reduction of Fe^{3+}-cytochrome c, inducing redox imbalance in cancer cells. The photoredox catalyst is equipotent towards normoxic and hypoxic adherent cancer cells, disrupting the mitochondrial membrane potential and inducing immunogenic apoptotic cell death. In contrast, current clinical photo-chemotherapeutic agents are less effective in hypoxic environments. Moreover, photo-catalyst **1** exhibits low toxicity towards normal cells in the dark, a favorable profile for reducing the side-effects of treatment. Complex **1** with its photo-controlled oxygen-independent immunogenic-apoptotic mechanism of cancer cell death is promising for further evaluation as a novel targeted anticancer agent.

Methods

UV-vis studies of complex 1 and NADH reactions. Reactions between complex **1** and NADH in various mol ratios were monitored by UV-vis spectroscopy at 310 K in the dark and on irradiation with 463 nm light. Turnover number (TON) is defined as the number of moles of NADH that a mole of complex **1** can convert within 30 min. Turnover frequency (TOF) was calculated from the difference in NADH concentration after 30 min divided by the concentration of complex **1**. The concentration of NADH was obtained using the extinction

coefficient ε_{339} = 6220 $M^{-1}cm^{-1}$.

Electron paramagnetic resonance (EPR). EPR spectra were recorded at ambient temperature (ca. 293 K) on a Bruker Model A300 ESR spectrometer equipped with a Bruker ER 4122 SHQ resonator using 1.0 mm quartz tubes. Typical instrument settings were: modulation amplitude 2.0 G and microwave power 0.63 mW, X-band frequency ca. 9.88 GHz. Spectra were acquired at 20 dB microwave attenuation (non-saturating 2 mW microwave power) with modulation amplitude of 0.2 mT peak-to-peak, time constant of 1.28 ms, receiver gain, 50–200; sweep time, 30 s and conversion time of 5.12 ms. The spin trap 5-(2,2-dimethyl-1,3-propoxycyclo-phosphoryl)-5-me-thyl-1-pyrroline N-oxide (CYPMPO 1 mM) was used for $NAD^{\bullet}$ radicals in PBS/methanol (1:1 v/v) containing complex **1** (500 μM, methanol) and NADH (10 mM, PBS) under 463 nm irradiation.

Electrochemistry

Cyclic voltammograms were recorded using a CH Instrument model 600D Electrochemical Analyzer/Workstation (Austin, TX). The electrochemical measurements were performed on complex **1** (1.0 mM) in acetonitrile solutions containing tetrabutylammonium hexafluorophosphate (0.1 M) as supporting electrolyte. The solutions were degassed under nitrogen and cyclic voltammograms were scanned from -2.3 V to +2.3 V (three complete scans for each experiment). In a typical electrochemical experimental set up, a three-electrode system was used: a glassy carbon electrode as the working electrode, saturated calomel electrode as the reference electrode, and platinum wire as the counter electrode. CV was performed at a scan rate of 100 mV/s. The excited state redox potentials were calculated from the ground state redox potentials and the emission maxima to aid evaluation of the photosensitization properties of complex **1**. Excited state reduction potentials: $E([M^*]^+/[M]^{2+}) = E_{ox} - E_{\lambda em}$. Excited state oxidative potentials: $E([M^*]^+/[M]^0) = E_{red} + E_{\lambda em}$. $E_{\lambda em} = 1240\ eV\ nm / \lambda_{em}$.

Data availability

The data that support the findings of this study are available within the paper and its Supplementary Information files, or from the corresponding authors on reasonable request. Crystallographic data for the complex [**1**]PF_6·(1.5 toluene) reported in this Article have been deposited at the Cambridge Crystallographic Data Centre, under deposition numbers CCDC 1840366). After the Open Access agreement has been established, underpinning datasets will be deposited in Warwick's Institutional Repository: Warwick Research Archive Portal (WRAP), according to the Open Access Agreement.

References

1. Riddell, I. A. & Lippard, S. J. Cisplatin and oxaliplatin: Our current understanding of their actions. *Met Ions Life Sci.* **18**, 1-42 (2018).
2. Meier-Menches, S. M. Gerner, C. Berger, W. Hartinger, C. G. & Keppler, B. K. Structure–activity relationships for ruthenium and osmium anticancer agents–towards clinical development. *Chem. Soc. Rev.* **47**, 909-928 (2018).
3. Bergamo, A. Dyson, P. J. & Sava, G. The mechanism of tumour cell death by metal-based anticancer drugs is not only a matter of DNA interactions. *Coord. Chem. Rev.* **360**, 17-33 (2018).
4. Farrer, N. J. Salassa, L. & Sadler, P. J. Photoactivated chemotherapy (PACT): the potential of excited-state d-block metals in medicine. *Dalton Trans.* **48**, 10690-10701 (2009).
5. Banerjee, S. & Chakravarty, A. R. Metal complexes of curcumin for cellular imaging, targeting, and photoinduced anticancer activity. *Acc. Chem. Res.* **48**, 2075-2083 (2015).
6. Lo, K. K. W. Luminescent rhenium(I) and iridium(III) polypyridine complexes as biological probes, imaging reagents, and photocytotoxic agents. *Acc. Chem. Res.* **48**, 2985-2995 (2015).
7. Knoll, J. D. & Turro, C. Control and utilization of ruthenium and rhodium metal complex excited states for photoactivated cancer therapy. *Coord. Chem. Rev.* **282**, 110-126 (2015).
8. Liu, J. *et al* Harnessing ruthenium(II) as photodynamic agents: Encouraging advances in cancer therapy. *Coord. Chem. Rev.* **363**, 17-28 (2018).
9. Heinemann, F. Karges, J. & Gasser, G. Critical overview of the use of Ru (II) polypyridyl complexes as photosensitizers in one-photon and two-photon photodynamic therapy. *Acc. Chem. Res.* **50**, 2727-2736, (2017).
10. Shi, G. *et al*. Ru(II) dyads derived from α-oligothiophenes: A new class of potent and versatile photosensitizers for PDT. *Coord. Chem. Rev.* **282**, 127-138 (2015).
11. Meggers, E. Asymmetric catalysis activated by visible light. *Chem. Commun.* **51**, 3290-3301 (2015).
12. Spring, B. Q. Rizvi, I. Xu, N. & Hasan, T. The role of photodynamic therapy in

overcoming cancer drug resistance. *Photochem. Photobiol. Sci.* **14**, 1476-1491 (2015).

13. Teicher, B. A. Hypoxia and drug resistance. *Cancer Metast. Rev.* **13**, 139-168 (1994).
14. Wang, H. P. *et al.* Phospholipid hydroperoxide glutathione peroxidase protects against singlet oxygen-induced cell damage of photodynamic therapy, *Free Radical Biol. Med.* **30** 825–835 (2001).
15. Henderson, B. & Miller, A. Effects of scavengers of reactive oxygen and radical species on cell survival following photodynamic treatment *in vitro*: comparison to ionizing radiation. *Radiat. Res.* **108**, 196-205 (1986).
16. Gomer, C. *et al.* Photodynamic Therapy-mediated oxidative stress can induce the expression of heat shock proteins. *Cancer Res.* **56**, 2355-2360 (1996).
17. Ruhdorfer, S. Sanovic, R. Sander, V. Krammer, B. & Verwanger, T. Gene expression profiling of the human carcinoma cell line A-431 after 5-aminolevulinic acid-based photodynamic treatment. *Int. J. Oncol.* **30**, 1253-1262 (2007).
18. Tong, Z. Singh, G. & Rainbow, A. J. Sustained activation of the extracellular signal regulated kinase pathway protects cells from photofrin-mediated photodynamic therapy. *Cancer Res.* **62**, 5528-5535 (2002).
19. Edmonds, C. Hagan, S. Gallagher-Colombo, S. M. Busch, T. M. & Cengel, K. A. Photodynamic therapy activated signaling from epidermal growth factor receptor and STAT3: Targeting survival pathways to increase PDT efficacy in ovarian and lung cancer, *Cancer Biol. Ther.* **13**, 1463-1470 (2012).
20. Assefa, Z. *et al.* The activation of the c-Jun N-terminal kinase and p38 mitogen-activated protein kinase signaling pathways protects HeLa cells from apoptosis following photodynamic therapy with hypericin, *J. Biol. Chem.* **274**, 8788–8796 (1999).
21. Kessel, D. & Erickson, C. Porphyrin photosensitization of multi-drug resistant cell types. *Photochem. Photobiol.* **55**, 397-399 (1992).
22. Hockel, M. & Vaupel, P. Tumor hypoxia: definitions and current clinical, biologic, and molecular aspects. *J. Natl. Cancer Inst.* **93**, 266-276 (2001).
23. Klimova, T. & Chandel, N. S. Mitochondrial complex III regulates hypoxic activation of HIF. *Cell Death Differ.* **15**, 660-666 (2008).

24. Chiarugi, A. Dölle, C. Felici, R. & Ziegler, M. The NAD metabolome-a key determinant of cancer cell biology. *Nat. Rev. Cancer* **12**, 741-752 (2012).
25. Prier, C. K. *et al.* Visible light photoredox catalysis with transition metal complexes: applications in organic synthesis. *Chem. Rev.* **113**, 5322-5363 (2013).
26. Huo, H. *et al.* Asymmetric photoredox transition-metal catalysis activated by visible light. *Nature* **515**, 100-103 (2014).
27. Demas, J. N. *et al.* Peer Reviewed: Oxygen Sensors Based on Luminescence Quenching. *Anal. Chem.* **71**, 793A-800A (1999).
28. Liu, Z. *et al.* The potent oxidant anticancer activity of organoiridium catalysts. *Angew. Chem. Int. Ed.* **53**, 3941-3946 (2014).
29. Ma, J. *et al* Preparation of chiral-at-metal catalysts and their use in asymmetric photoredox chemistry. *Nat. Protoc.* **13**, 605-632 (2018).
30. Peterson, J. R. Smith, T. A. & Thordarson, P. Synthesis and room temperature photo-induced electron transfer in biologically active bis (terpyridine) ruthenium(II)–cytochrome c bioconjugates and the effect of solvents on the bioconjugation of cytochrome c. *Org. Biomol. Chem.* **8**, 151-162 (2010).
31. Boaz, H. & Rollefson, G. K. The quenching of fluorescence. Deviations from the Stern-Volmer law. *J. Am. Chem. Soc.* **72**, 3435-3443 (1950).
32. Matsuzaki, S. Kotake, Y. & Humphries, K. M. Identification of mitochondrial electron transport chain-mediated NADH radical formation by EPR spin-trapping techniques. *Biochemistry* **50**, 10792-10803 (2011).
33. Lapuente-Brun, E. *et al*. Supercomplex assembly determines electron flux in the mitochondrial electron transport chain. *Science* **340**, 1567-1570 (2013).
34. Li, H. *et al*. Cytochrome c release and apoptosis induced by mitochondrial targeting of nuclear orphan receptor TR3. *Science*, **289**, 1159-1164 (2000).
35. Margoliash, E. & Frohwirt, N. Spectrum of horse-heart cytochrome c. *Biochem. J.* **71**, 570-572 (1959).
36. Huang, H. *et al.* Highly charged ruthenium(ii) polypyridyl complexes as lysosome-localized photosensitizers for two-photon photodynamic therapy. *Angew. Chem. Int. Ed.*

54, 14049-14052 (2015).

37. Peng, Q. *et al*. 5-Aminolevulinic acid-based photodynamic therapy. *Cancer* **79**, 2282-2308 (1997).
38. Huang, H. *et al*. Real-time tracking mitochondrial dynamic remodeling with two-photon phosphorescent iridium(III) complexes. *Biomaterials* **83**, 321-331 (2016).
39. Berezin, M. Y. & Achilefu, S. Fluorescence lifetime measurements and biological imaging. *Chem. Rev.* **110**, 2641-2684 (2010).
40. Berridge, M. V. Herst, P. M. & Tan, A. S. Tetrazolium dyes as tools in cell biology: new insights into their cellular reduction. *Biotechnol. Annu. Rev.* **11**, 127-152 (2005).
41. Waghray, M. *et al*. Hydrogen peroxide is a diffusible paracrine signal for the induction of epithelial cell death by activated myofibroblasts. *FASEB J.* **19**, 854-856 (2005).
42. He, Y. Y. & Häder, D. P. UV-B-induced formation of reactive oxygen species and oxidative damage of the cyanobacterium Anabaena sp.: protective effects of ascorbic acid and N-acetyl-L-cysteine. *J. Photochem. Photobiol. B* **66**, 115-124 (2002).
43. Ricci, J. E. *et al*. Disruption of mitochondrial function during apoptosis is mediated by caspase cleavage of the p75 subunit of complex I of the electron transport chain. *Cell*, **117**, 773-786 (2004).
44. Tesniere, A. *et al*. Immunogenic death of colon cancer cells treated with oxaliplatin. *Oncogene* **29**, 482-491 (2010).
45. Coverdale, J. P. *et al*. Asymmetric transfer hydrogenation by synthetic catalysts in cancer cells. *Nat. Chem.* **10**, 347-354 (2018).
46. Moan, J. Effect of bleaching of porphyrin sensitizers during photodynamic therapy. *Cancer lett.* **33**, 45-53 (1986).
47. Gorrini, C. Harris, I. S. & Mak, T. W. Modulation of oxidative stress as an anticancer strategy. *Nat. Rev. Drug Discov.* **12**, 931-947 (2013).
48. Porras, J. A. Mills, I. N. Transue, W. J. & Bernhard, S. Highly Fluorinated Ir(III)-2,2′:6′,2″-Terpyridine–Phenylpyridine–X Complexes via Selective C–F Activation: Robust Photocatalysts for Solar Fuel Generation and Photoredox Catalysis. *J. Am. Chem. Soc.* **138**, 9460-9472 (2016).

49. Tinker, L. L. *et al*. Visible light induced catalytic water reduction without an electron relay. *Chem. Eur. J*. **13**, 8726-8732 (2007).
50. Gębicki, J. Marcinek, A. & Zielonka, J. Transient species in the stepwise interconversion of NADH and NAD^+. *Acc. Chem. Res.* **37**, 379-386 (2004).
51. Fukuzumi, S. Inada, O. & Suenobu, T. Mechanisms of electron-transfer oxidation of NADH analogues and chemiluminescence. Detection of the keto and enol radical cations. *J. Am. Chem. Soc.* **125**, 4808-4816 (2003).
52. Tanaka, M. Ohkubo, K. & Fukuzumi, S. DNA cleavage by UVA irradiation of NADH with dioxygen via radical chain processes. *J. Phys. Chem. A* **110**, 11214-11218 (2006).
53. Lee, H. Y. Chen, S. Zhang, M. H. & Shen, T. Studies on the synthesis of two hydrophilic hypocrellin derivatives with enhanced absorption in the red spectral region and on their photogeneration of O_2^- and O_2 ($^1\Delta_g$). *J. Photochem. Photobiol. B* **71**, 43-50 (2003).
54. Hvasanov, D. Mason, A. F. Goldstein, D. C. Bhadbhade, M. & Thordarson, P. Optimising the synthesis, polymer membrane encapsulation and photoreduction performance of Ru(II)-and Ir(III)-bis(terpyridine) cytochrome c bioconjugates. *Org. Biomol. Chem.* **11**, 4602-4612 (2013).
55. Sabharwal, S. S. & Schumacker, P. T. Mitochondrial ROS in cancer: initiators, amplifiers or an Achilles' heel? *Nat. Rev. Cancer* **14**, 709-721 (2014).
56. Wenzel, C. *et al.* 3D high-content screening for the identification of compounds that target cells in dormant tumor spheroid regions. *Exp. Cell Res.* **323**, 131-143 (2014).
57. Ji, J. Zhang, Y. Chen, W. R. Wang, X. DC vaccine generated by ALA-PDT-induced immunogenic apoptotic cells for skin squamous cell carcinoma. *Oncoimmunology* **5**, e1072674 (2016).
58. Galluzzi, L. Buqué, A. Kepp, O. Zitvogel, L. & Kroemer, G. Immunogenic cell death in cancer and infectious disease. *Nat. Rev. Immunol.* **17**, 97-111 (2017).

Acknowledgements

We thank the EPSRC (grants EP/G006792, EP/F034210/1 and EP/P030572/1 for P.J.S., platform grant EP/P001459/1 for M.J.P, EPSRC DTP studentship for T.M., EP/N010825/1

for M.S., and EP/N010825 for V.G.S.), MRC (grant G0701062 for P.J.S.), The Royal Society (Newton International Fellowship NF160307 for H.H., Newton-Bhahba International Fellowship NF151429 for S.B.), Leverhulme Trust (Senior Research Fellowship for V.G.S.), National Science Foundation of China (grants NSFC, 21701113 for P.Z., 21525105, 21471164, 21778079 for H.C.), 973 Program (2015CB856301 for H.C.), The Fundamental Research Funds for the Central Universities (for H.C.), ERC (Consolidator Grant GA 681679 PhotoMedMet for G.G.), and French Government (Investissementsd'Avenir grant ANR-10-IDEX-0001-02 PSL for G.G.). The Sun Yat-sen University Startup fund 75110-18841213 for H.H. We also thank W. Zhang, Dr. L. Song and P. Aston for assistance with mass spectrometry; Dr. J. P. C. Coverdale for assistance with ICP-MS experiments; and Dr. I. Prokes for assistance with NMR spectroscopy.

Correspondence and requests for materials should be addressed to P. J. S. (p.j.sadler@warwick.ac.uk), H. C. (ceschh@mail.sysu.edu.cn) or G. G. (gilles.gasser@chimieparistech.psl.eu)

Author Contributions

All authors were involved with the design and interpretation of experiments and with the writing of the script. H. H. and S. B. contributed equally to this work. Chemical and biological experiments were carried out by H. H., S. B., K. Q. and P.Z. X-ray crystallography was carried out by S. B. and G. J. C. DFT calculations were carried by O. B., T. M. and M. J. P. M. S. and V. G. S. carried out the excited state photochemistry experiments and analyzed the data. H. H., S. B., H. C., G. G. and P. J. S analyzed the data and co-wrote the paper. All authors discussed the results and commented on the manuscript. All authors have given approval to the final version of the manuscript.

Competing interests

The authors declare no competing financial interests.

Additional information

***e-mail:**

p.j.sadler@warwick.ac.uk; ceschh@mail.sysu.edu.cn; gilles.gasser@chimieparistech.psl.eu

Supplementary Information is available with the online version of this paper.

Figure Captions

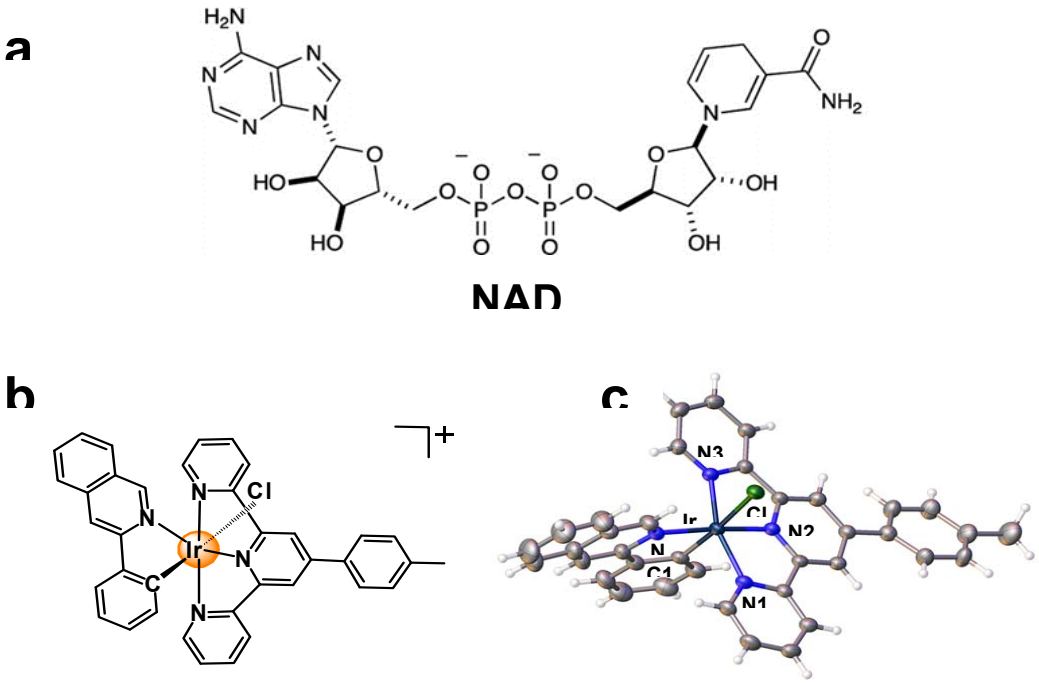

Figure 1. Structures of compounds. a) NADH. b) Complex **1**, line structure, and c) X-ray crystal structure; the counter ion PF_6^- has been omitted for clarity.

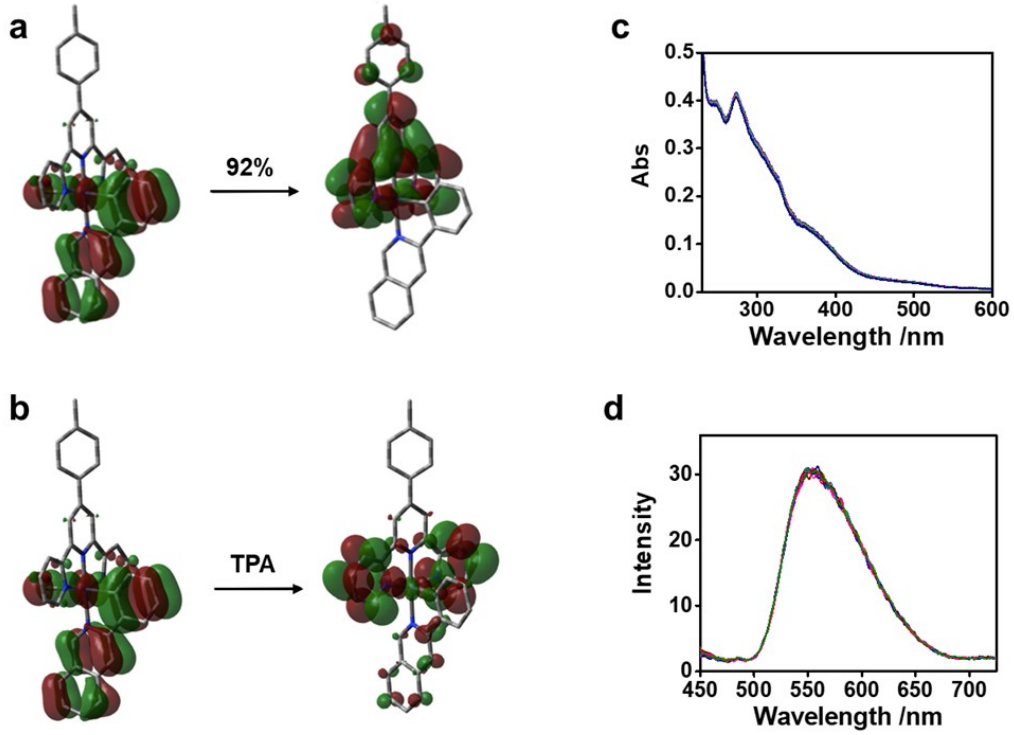

Figure 2. DFT calculations and stability of complex 1. a) Dominant canonical particle-hole orbitals with overall contribution to the lowest first triplet state of **1**. b) Dominant canonical particle-hole orbital representation of the strong TPA intermediate state by non-resonant 3-state model. c) UV-vis spectra showing the dark stability of **1** in RPMI-1640 cell culture medium at 293 K for 24 h. The experiment was repeated three times independently with similar results. d) Photostability of the emission of **1** in PBS under continuous 463 nm light irradiation for 30 min at 293 K. The experiment was repeated three times independently with similar results.

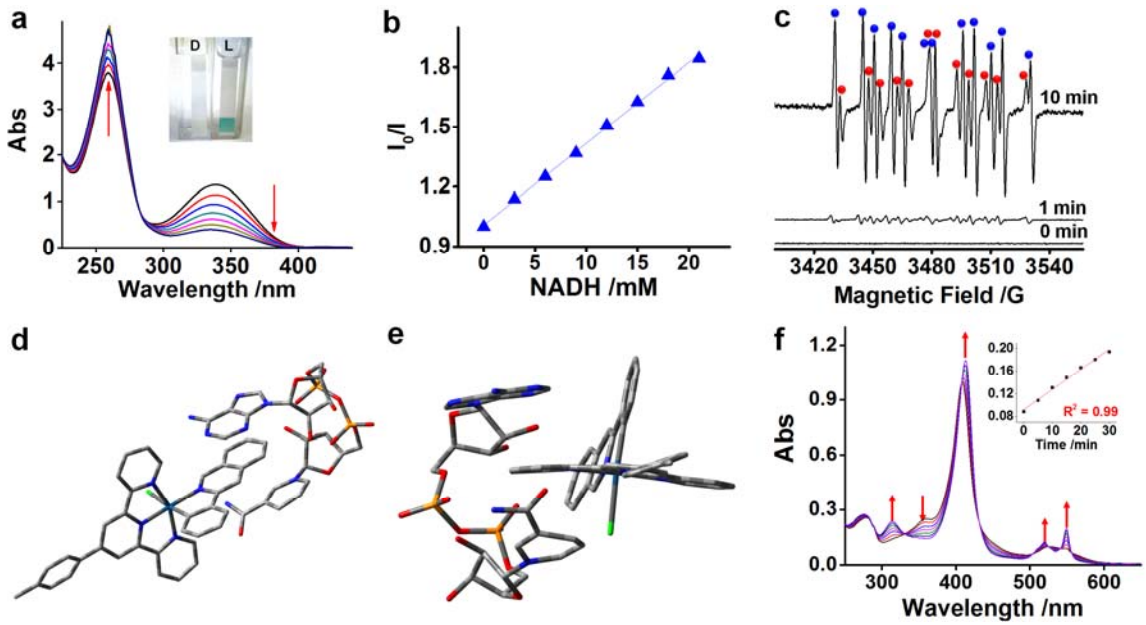

Figure 3 Photoredox reaction between NADH and complex 1 under 463 nm blue-light irradiation. a) Photo-catalytic oxidation of NADH (240 μM) by complex **1** (6 μM) in PBS monitored by UV-vis spectroscopy; inset: detection of H_2O_2 after irradiation (D = dark, L = light). The coloured lines represent spectra recorded every 5 min for 0.5 h. The direction of change in absorbance with time is indicated by red arrows. The experiment was repeated five times independently with similar results. b) Stern−Volmer plot showing NADH interacts with the excited state of complex **1**. The experiment was repeated three times independently with similar results. c) X-band EPR spectrum of $NAD^{\bullet}$ radicals trapped by CYPMPO at various times after irradiation with 463 nm light: CYPMPO-NAD (blue circles, α_N = 14.43 G, α_H = 20.35 G, α_P = 50.72 G), CYPMPO-CH_3 (red circles, α_N = 14.67 G, α_H = 20.25 G, α_P = 48.92 G, where α is the hyperfine coupling constant for coupling of the unpaired electron with 14N, 1H or 31P, where 14, 1 and 31 are superscripts). The experiment was repeated five times independently with similar results. d) Optimized DFT stable minima for NADH-**1** (triplet state**)** structures with NADH clamped around pq or e) ttpy ligands. f) Photo-catalytic

reduction of oxidised cyt c (11.2 μM) by NADH (50 μM) and complex **1** (0.6 μM), inset: dependence of absorbance at 550 nm on irradiation time. R^2 is the coefficient of determination (goodness of fit). The experiment was repeated three times independently with similar results.

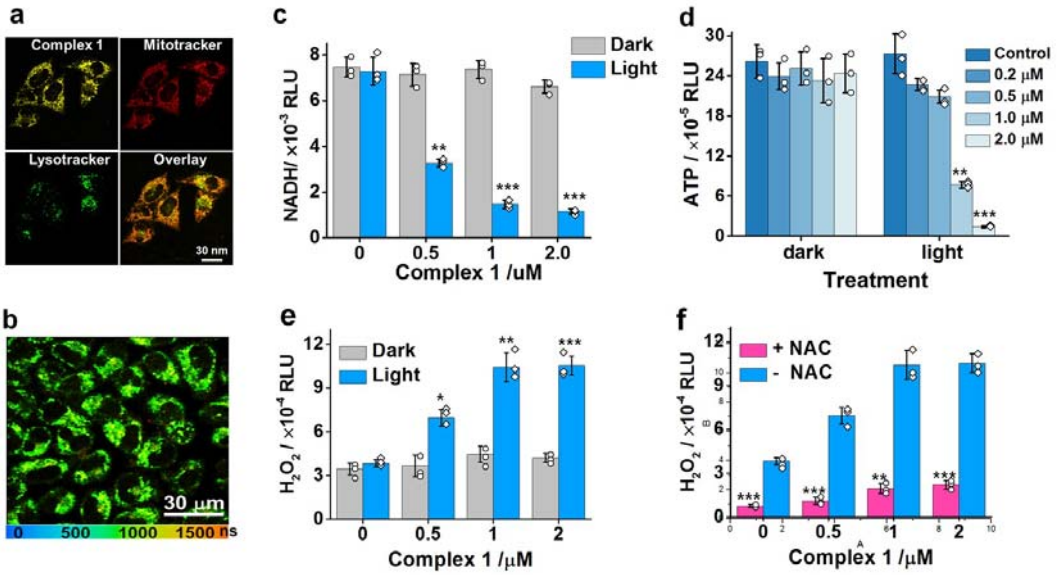

Figure 4 Cellular localization and cellular response after irradiation. a) One- and two-photon images of A549 lung cancer cells treated with **1** (5 μM) for 1 h and co-stained with mitochondrial and lysosomal dyes. $\lambda_{ex}/\lambda_{em}$: **1** 405/562 nm, lysotracker 488/520 nm, mitotracker 633/660 nm. The experiment was repeated three times independently with similar results. b) Phosphorescence lifetime images of living A549 cells treated with **1** (5 μM), $\lambda_{ex}/\lambda_{em}$: 760/562 nm. The experiment was repeated twice independently with similar results. c) NADH concentration, d) ATP concentration, and e) H_2O_2 concentration, in A549 cells treated with various doses of **1** in the dark or light. f) H_2O_2 concentration in A549 cells after light irradiation in the presence or absence of 5 mM N-acetyl-L-cysteine (NAC; cell exposure to **1** for 2 h, washed, followed by 465 nm light irradiation 8.9 J/cm^2). RLU: relative luminescence unit. Figure 4c-4f: All the experiments were performed as duplicates of triplicates (n=6 biologically independent experiments). Error bars show ±1 s.d. from the mean. Statistics were calculated using the two-tailed t-test with unequal variances (Welch's unpaired t-test) by comparing sample treated with the same dose in the presence or absence of light irradiation. $^{*}p < 0.05$, $^{**}p < 0.01$ $^{***}p < 0.001$. p values:

4c: NADH 0.5 μM (p = 0.0029), 1.0 μM (p = 0.0003), 2.0 μM (p = 0.0002)

4d: ATP light 1.0 μM (p = 0.0132), 2.0 μM (p = 0.0052)

4e: H_2O_2 0.5 μM (p = 0.0048), 1.0 μM (p = 0.0025), 2.0 μM (p = 0.0009)

4f: +NAC 0.0 μM (p = 0.0009), 0.5 μM (p = 0.0003), 1.0 μM (p = 0.0035), 2.0 μM (p = 0.0003).

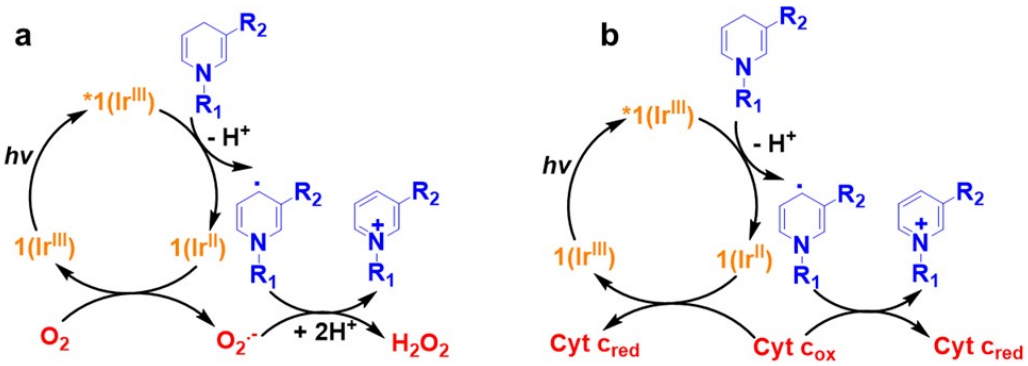

Figure 5. Photo-catalytic cycle for oxidation of NADH by complex 1 showing the production of NAD· radicals, involvement of oxygen, and reduction of cytochrome c. a) The reductive catalytic cycle under normoxia. b) Catalytic cycle under hypoxia in the presence of Fe^{3+}-cyt c as electron acceptor.

Table of contents graphic

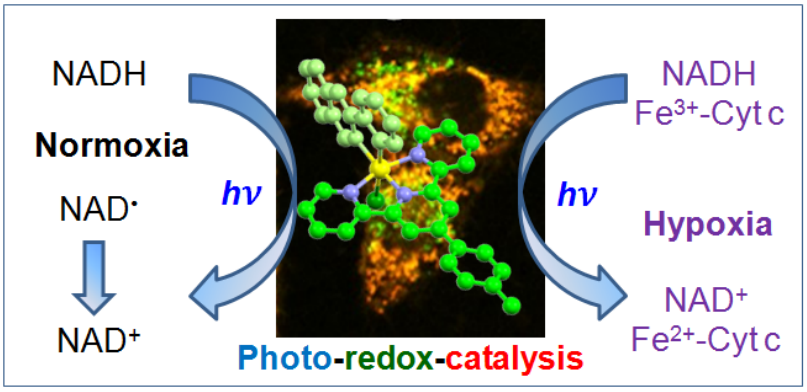

Current photodynamic therapy photosensitizers require oxygen, while tumours are often hypoxic. An organo-iridium complex with an unusually high redox potential is equally effective in normoxia and hypoxia, and kills cancer cells by a unique immunogenic-apoptotic mechanism involving efficient photocatalytic oxidation of NADH to NAD radicals, and reduction of cytochrome c.

Supplementary Information

Targeted photoredox catalysis in cancer cells

Huaiyi Huang, Samya Banerjee, Kangqiang Qiu, Pingyu Zhang, Olivier Blacque, Thomas Malcomson, Martin J. Paterson, Guy J. Clarkson, Michael Staniforth, Vasilios G. Stavros, Gilles Gasser, Hui Chao and Peter J. Sadler

Contents

1. Materials

2. Instruments and methods

2.1 X-ray crystallography

2.2 Electrochemistry

2.3 NMR spectroscopy

2.4 Electrospray ionization mass spectrometry (ESI-MS)

2.5 Elemental analysis

2.6 pH measurement

2.7 UV-vis spectroscopy

2.8 Phosphorescence spectra

2.9 Phosphorescence quantum yield and lifetimes

3. Synthesis of [Ir(ttpy)(pq)Cl]PF_6 ([**1**]PF_6)

4. Photo-catalytic reactions of complex **1** with NADH

4.1 ^{1}H NMR spectra

4.2 UV-vis spectra

4.3 Detection of H_2O_2 generation

4.4 UV-vis spectra for reactions of complex **1**, NADH and cytochrome c

5. Electron paramagnetic resonance (EPR).

6. Determination of singlet oxygen quantum yield

7. Computational Details

7.1 Density functionals

7.2 Ground and excited state geometries

7.3 Two-photon absorption cross section measurement

7.4 Redox and photo-redox chemistry calculations

7.5 Calculation of interaction between complex **1** and NADH

7.6. Photocatalytic reduction of Fe^{3+}-cyt c by complex **1** and NADH

8. Cell culture and cell assays

8.1 Cell culture

8.2 Dark- and photo-cytotoxicity assays

8.3 Cellular localization assays

8.4 ICP-MS assays

8.5 Phosphorescence lifetime imaging microscopy (PLIM)

8.6 Intracellular ROS measurement

8.7 Two-photon induced ROS generation in A549 MCS

8.8 Intracellular NADH concentration

8.9 Intracellular ATP concentration

8.10 Intracellular H_2O_2 concentration

8.11 Formazan formation assay

8.12 Evaluation of mitochondrial membrane potentials ($\Delta\Psi_m$)

8.13 Annexin V/PI assay

8.14 Calreticulin immunofluorescence assay

8.15 HMGB1 ELISA assay

Supplementary Tables

Supplementary Tables 1, 2 Crystallographic data for complex **1**

Supplementary Table 3 Singlet-singlet and singlet-triplet excitations calculated with TD-DFT

Supplementary Table 4 Photophysical properties of complex **1**

Supplementary Table 5 Electrochemical properties of complex **1** and related complexes

Supplementary Table 6 DFT optimized parameters for the singlet ground state and first triplet excited state of complex **1**

Supplementary Table 7 Calculated redox potentials of complex **1**

Supplementary Table 8 Photocatalytic oxidation of NADH by complex **1**

Supplementary Table 9 Dark- and photo-toxicity of complex **1**

Supplementary Figures

Supplementary Figure 1 UV–vis spectra of complex **1** in various solvents.

Supplementary Figure 2 Calculated electronic absorption spectrum of complex **1**

Supplementary Figure 3 Phosphorescence spectra of complex **1**

Supplementary Figure 4 Phosphorescence spectra of complex **1** under air and N_2

Supplementary Figure 5 Phosphorescence lifetime spectra of complex **1**

Supplementary Figure 6 Frontier orbitals of the DFT optimized ground state of complex **1**

Supplementary Figure 7 Two-photon absorption cross sections of complex **1**

Supplementary Figure 8 Dark stability of complex **1** in a d_6-DMSO stock solution

Supplementary Figure 9. Stability of complex **1** in human serum

Supplementary Figure 10 Cyclic voltammogram of complex **1** in N_2-saturated acetonitrile

Supplementary Figure 11 DFT optimized parameters for ground state of complex **1**.

Supplementary Figure 12 Catalytic photo-oxidation of NADH complex **1** monitored by ^{1}H NMR

Supplementary Figure 13 Catalytic photo-oxidation of NADH complex **1** monitored by UV-vis spectra

Supplementary Figure 14 Mass spectra of photocatalytic reaction between NADH and complex **1**

Supplementary Figure 15 Concentration dependence of photo-catalytic reaction of NADH with complex **1**

Supplementary Figure 16 Long-term catalytic photo-oxidation of NADH and complex **1**

Supplementary Figure 17 pH change during the photocatalytic reaction of NADH with complex **1**

Supplementary Figure 18 X-band EPR spectra of irradiated solutions of complex **1**, NADH and DMPO

Supplementary Figure 19 Singlet oxygen generation by complex **1**

Supplementary Figure 20 Photo-catalytic reaction of NADH with complex **1** under nitrogen

Supplementary Figure 21 Photocatalytic reduction of oxidized Fe^{3+}-cyt c by NADH and complex **1**

Supplementary Figure 22. Photo-reduction rate of Fe^{3+}-cyt c and complex **1** or

$[Ir(tpy)_2]^{3+}$ in the presence of radical trapping agent CYPMPO.

Supplementary Figure 23. Dose-response curves for dark- and photo-toxicity of complex **1** against various cancer cell lines under normoxia and hypoxia.

Supplementary Figure 24. Dose-response curves for dark- and photo-toxicity of cisplatin and 5-ALA towards various cancer cell lines under under normoxia and hypoxia.

Supplementary Figure 25. Dose-response curves for dark- and photo-toxicity of complex **1** towards A549 cancer cells in the presence of various ROS inhibitors under normoxia and hypoxia.

Supplementary Figure 26. Dose-response curves for dark- and photo-toxicity of cisplatin, complex **1** and 5-ALA towards MRC-5 and LO2 normal cell lines under normoxia.

Supplementary Figure 27. Dose-response curves for dark- and photo-toxicity of cisplatin, complex **1**, and 5-ALA towards A549 cancer spheroids under normoxia.

Supplementary Figure 28. ICP-MS quantification of the internalized Ir in A549 cells.

Supplementary Figure 29. Phosphorescence lifetime spectrum of complex **1** in A549 cancer cells.

Supplementary Figure 30. Formazan formation assay in A549 cancer cells.

Supplementary Figure 31. ROS generation in complex **1**-treated A549 cancer cells after light irradiation under normoxia and hypoxia.

Supplementary Figure 32. ROS generation in multicellular A549 spheroids treated with complex **1** upon two-photon light irradiation.

Supplementary Figure 33. Change in the mitochondrial membrane potential in A549 cancer cells induced by complex **1** on light irradiation.

Supplementary Figure 34. Unaltered mitochondrial membrane potentials in MRC-5 normal cells on treatment with complex **1** in the dark.

Supplementary Figure 35. Apoptosis of A549 cells under normoxia and hypoxia photo-induced by complex **1** detected by Annexin V/PI staining.

Supplementary Figure 36. Response to the immunogenic-apoptotic cell death mechanism in A549 cancer cells.

References

1. Materials

All solvents were of analytical grade. All buffer components were of biological grade and used as received. The cyclometalated ligand 3-phenylisoquinoline (3-pq), cisplatin, 5-aminolevulinic acid (5-ALA), oxidized cytochrome c (Cyt c) from beef heart, 5-(2,2-dimethyl-1,3-propoxycyclophosphoryl)-5-methyl-1-pyrroline N-oxide (CYPMPO), 5,5-dimethyl-1-pyrroline N-oxide (DMPO), 2,2,6,6-tetramethylpiperidine (TEMP), β-nicotinamide adenine dinucleotide, reduced disodium salt (NADH), $IrCl_3{\cdot}3H_2O$, and human serum were from Sigma-Aldrich. 5,5′,6,6′-tetrachloro-1,1′,3,3′-tetraethylbenzimidazolylcarbocyanine iodide (JC-1), Mitotracker Red FM (MTR), Lysotracker green DND-26 (LTG), 3-(4,5-dimethylthiazol-2-yl)-2,5-diphenyltetrazolium bromide (MTT), sulforhodamine B (SRB), 2′,7′-dichlorofluorescin diacetate (DCFH-DA) and cell apoptosis detection Annexin V/PI kit were bought from Life Technologies (USA). CellTitler-Glo® Cell Viability kit, CellTiter-Glo® 3D Cell Viability kit, ROS-Glo™ H_2O_2 kit and NAD/NADH-Glo™ kit were purchased from Promega (USA). Nucleus extraction kit, mitochondrial extraction kit and cytoplasm extraction kit were purchased from Thermo Scientific Pierce, Alexa Fluor 488 linked–Calreticulin antibody from Abcam, Cambridge (UK), and enzyme-linked immunosorbent test (ELISA) for high mobility group box 1 protein (HMGB1) from Cloud-Clone Corp (Wuhan, China).

2. Instruments and methods

2.1. X-ray crystallography

Single crystals of **1** were grown by slow evaporation of solvent from toluene and acetonitrile solutions. A suitable crystal of compound [**1**]$\mathbf{PF_6{\cdot}1.5(toluene)}$ $C_{47.5}H_{39}ClF_6IrN_4P$ was selected and mounted on a glass fibre with Fomblin oil and placed on a Rigaku Oxford Diffraction SuperNova diffractometer with a dual source (Cu at zero) equipped with an AtlasS2 CCD area detector. The crystal was kept at 150(2) K during data collection. Using Olex2[1], the structure was solved with Solve structure solution program[2] using Charge Flipping and refined with the ShelXL[3] refinement package using Least Squares minimization. X-ray crystallographic data for complex [**1**]$PF_6{\cdot}$(1.5 toluene) have been deposited in the CCDC under the accession number 1840366.

2.2. Electrochemistry[4]

Cyclic voltammogram (CV) experiments were carried out using a CH Instrument model 600D Electrochemical Analyzer/Workstation (Austin, TX). The electrochemical measurements were performed on complex **1** (1.0 mM) in acetonitrile solution containing tetrabutylammonium hexafluorophosphate (0.1 M) as supporting electrolyte. The solutions were degassed under nitrogen and cyclic voltammograms were scanned from -2.3 V to +2.3 V (three complete scans for each experiment). In a typical electrochemical experimental set up, the three-electrode system was used: a glassy carbon electrode as the working electrode, SCE as the reference electrode, and

platinum wire as the counter electrode. CV was performed at a scan rate of 100 mV/s. The excited state redox potentials were calculated from the ground state redox potentials and the emission maxima to aid evaluation of the photosensitization properties of complex **1**. Excited state reduction potentials: $E([M^*]^+/[M]^0) = E_{red} + E_{\lambda em}$. $E_{\lambda em} = 1240/\lambda_{em}$.[4] Throughout the manuscript, the American standard is followed to describe the electro-chemical parameters.

2.3. NMR spectroscopy

^{1}H NMR spectra were acquired in 5 mm NMR tubes at 293 K or 310 K on either Bruker DPX 400 (^{1}H = 400.03 MHz) or AVA 600 (^{1}H = 600.13 MHz) spectrometers. ^{1}H NMR chemical shifts were internally referenced to CHD_2OD (3.33 ppm) for d_4-CD_3OD. 2D ^{1}H–^{1}H COSY NMR spectra were recorded at 293 K in d_6-DMSO. All data processing was carried out using MestReC or TOPSPIN version 2.0 (Bruker UK Ltd.).

2.4. Electrospray ionization mass spectrometry (ESI-MS)

Electrospray ionization mass spectra were obtained by preparing the samples in 50% methanol and 50% H_2O (v/v) or using NMR samples for infusion into the mass spectrometer (Bruker Esquire 2000). The mass spectra were recorded with a scan range of m/z 400–1000 for positive ions or negative ions.

2.5. Elemental analysis

CHN elemental analyses were carried out on a CE-440 elemental analyzer by Warwick Analytical (UK) Ltd.

2.6. pH measurement

pH values during photoredox catalysis in H_2O at ca. 293 K were determined directly in 1-cm path-length quartz cuvettes (3 mL) during 460 nm light irradiation, using a Corning 240 pH meter equipped with a micro combination electrode calibrated with Aldrich buffer solutions of pH 4, 7 and 10.

2.7. UV-vis spectroscopy

A Cary 300 UV-vis spectrophotometer was used with 1-cm pathlength quartz cuvettes (3 mL) and a PTP1 Peltier temperature controller. Spectra were processed using UV Winlab software. Experiments were carried out at 293 K from 600 to 200 nm.

2.8. Phosphorescence spectra

Phosphorescence emission measurements were performed on a JASCO FP-6500 spectrofluorometer. Complex **1** (10 μM) in acetonitrile or phosphate buffer saline (PBS) was diluted from a stock solution in DMSO (1 mM). The complexes were excited at λ_{ex} = 405 nm in a 1-cm quartz cuvette at 298 K. Experiments were performed in air.

2.9. Phosphorescence quantum yield and lifetimes

Phosphorescence quantum yields were measured on a Fluorolog spectrofluorometer (Horiba Jobin Yvon) equipped with a 405 nm pulsed diode NanoLED light source. Ir(III) complexes were diluted from a stock solution in DMSO (1 mM) to achieve an absorbance = 0.1 at 405 nm in acetonitrile or PBS. The complexes were excited at λ_{ex} = 405 nm in a 1-cm quartz cuvette at 298 K. Experiments were performed in air and emission spectra were corrected for the spectral sensitivity of the detection system by standard correction curves. Quantum yields in aerated acetonitrile were determined by comparison with the emission of $[Ru(bpy)_3]Cl_2$ in aerated water (Φ = 0.040)[5]. Phosphorescence lifetime measurements used the same equipment and measurement was stopped after gathering 1000 counts of excited state species. The raw data were analyzed with OriginPro 2016 software by using exponential function to obtain the phosphorescence lifetime.

3. Synthesis of $[Ir(ttpy)(pq)Cl]PF_6$ ($[1]PF_6$)

The polypyridyl ligand 4′-p-tolyl-2,2′:6,2″-terpyridine (ttpy) was prepared as described by Wand and Hanan[6]. $[Ir(ttpy)Cl_3]$ was prepared based on the procedure reported by Porras et al[4].

A mixture of $[Ir(ttpy)Cl_3]$ (125 mg, 0.20 mmol) and excess 3-phenylisoquinoline (3-pq) (82 mg, 0.40 mmol) in glycol (10 mL) was stirred overnight at 453 K under nitrogen. The reaction mixture became a clear orange solution. After cooling to room temperature, the solution was poured into 50 mL saturated NH_4PF_6 solution to give an orange precipitate. The precipitate was isolated by filtration and washed with water and diethyl ether 3 times. The crude product was purified by column chromatography on neutral alumina oxide with methanol−dichloromethane (1:9 v/v) as the eluent. The solvent was removed under reduced pressure, and orange complex **1** was obtained.
Yield: 45%. ESI-MS [CH_3OH, m/z]: 755.5 ($[M\text{-}PF_6]^+$)。Anal. calcd. for $IrC_{37}H_{27}N_4ClPF_6$: C, 49.36; H, 3.02; N, 6.22; found: C, 49.25; H, 3.09; N, 6.24. ^{1}H NMR (400 MHz, d_6-$(CD_3)_2SO$) δ 10.66 (s, 1H), 9.28 (s, 2H), 9.00 (d, *J* = 9.6 Hz, 2H), 8.99 (s, 1H), 8.45 (d, *J* = 8.2 Hz, 1H), 8.31 (d, *J* = 8.4 Hz, 1H), 8.28 (d, *J* = 8.2 Hz, 2H), 8.23 (t, *J* = 8.0 Hz, 2H), 8.05 (t, *J* = 7.6 Hz, 1H), 8.00 (d, *J* = 7.6 Hz, 1H), 7.89 (t, *J* = 7.6 Hz, 1H), 7.81 (d, *J* = 5.4 Hz, 2H), 7.57 (d, *J* = 8.0 Hz, 2H), 7.48 (t, *J* = 6.4 Hz, 2H), 6.96 (t, *J* = 7.6 Hz, 1H), 6.75 (t, *J* = 7.2 Hz, 1H), 6.08 (d, *J* = 7.6 Hz, 1H), 2.50 (s, 3H). ^{13}C NMR (101 MHz, DMSO) δ 158.39, 157.90, 155.79, 155.40, 152.47, 151.74, 144.23, 141.83, 140.52, 139.72, 137.36, 134.07, 132.80, 130.62, 130.44, 129.82, 129.61, 129.43, 128.91, 128.57, 128.49, 127.48, 126.43, 124.51, 124.34, 121.61, 117.49, 21.45.

Crystals of complex **$1PF_6$ 1.5(toluene)** suitable for x-ray diffraction were grown by slow evaporation from a solution in toluene and acetonitrile (1:1 v/v).

X-ray data have been deposited as CCDC 1840366. The asymmetric unit contains the complex, a PF_6 counter ion, a toluene and a toluene on an inversion centre. The toluyl ring of the terpyridine was modeled as disordered over two positions related by

a rotation about the bond to the terpyridine. The occupancy of the two components was linked to a free variable which refined to 55:45. There was a toluene solvent disordered over two closely related positions. The occupancy of the two components was linked to a free variable which refined to 71:29. The minor component was refined isotropically. There was another toluene disordered about the inversion centre. It was refined behind a PART -1 instruction at 50% occupancy. Several DFIX and SIMU restraints and an AFIX 66 constraint were used to give the disordered components reasonable bond lengths, angles and thermal parameters.

4. Photocatalytic reactions of complex 1 with NADH

4.1. ^{1}H NMR spectra[7]

NADH (3.5 mol equiv) was added to an NMR tube containing a 0.25 mM of complex **1** in 50% CD_3OD/49.5% D_2O and 0.5% H_2O at ambient temperature. ^{1}H NMR spectra of the resulting solutions were recorded at 310 K after 5 min or 24 h in the dark, or after 10 min of 463 nm light irradiation.

4.2. UV-vis spectra

Reactions between complex **1** and NADH at different ratios were monitored by UV-vis at 310 K in the dark or on irradiation with 463 nm light. Turnover number (TON) is defined as the number of moles of NADH that a mole of complex **1** can convert within 30 min. Turnover frequency (TOF) was calculated from the difference in NADH concentration after 30 min irradiation divided by the concentration of complex **1**. The concentration of NADH was obtained using the extinction coefficient[7] $\varepsilon_{339} = 6220\ M^{-1}cm^{-1}$.

4.3. Detection of H_2O_2 generation

For the reaction of complex **1** (6 μM) with NADH (240 μM) in 0.5% DMSO/99.5% PBS (v/v) at 293 K in the dark or after irradiation, H_2O_2 was detected by Quantofix peroxide test sticks (Sigma).

4.4. UV-vis spectra for reactions of 1, NADH and cyt c

Reactions between complex **1** (0.6 μM), NADH (48 μM) and cyt c (11 μM) under hypoxia were monitored by UV-vis in the dark or on irradiation with 463 nm light. PBS solution in a special cuvette (3 mL) was degassed by bubbling N_2 for 15 min. Aliquots of stock solutions of cyt c (1 mM), NADH (10 mM) and complex **1** (1 mM) were added to the cuvette while continuously bubbling nitrogen into the PBS. The concentration of cyt c was obtained using extinction coefficients $\varepsilon_{550} = 8000\ M^{-1}cm^{-1}$ for oxidized cyt c, and $\varepsilon_{550} = 28000\ M^{-1}cm^{-1}$ for reduced cyt c[8].

5. Electron paramagnetic resonance (EPR)[9]

All EPR measurements were carried out at ambient temperature (ca. 293 K) on a Bruker Model A300 ESR spectrometer equipped with a Bruker ER 4122 SHQ

resonator, using 1.0 mm quartz tubes. Typical instrument settings were: modulation amplitude 2.0 G, microwave power 0.63 mW and X-band frequency ca. 9.88 GHz. Spectra were acquired at 20 dB microwave attenuation (non-saturating 2 mW microwave power) with modulation amplitude of 0.2 mT peak-to-peak, time constant of 1.28 ms, receiver gain 50–200; sweep time, 30 s and conversion time of 5.12 ms. The spin trap 2,2,6,6-tetramethylpiperidine (TEMP) was used to detect $^1O_2$ in acetonitrile. 5,5-dimethyl-1-pyrroline-N-oxide (DMPO 10 mM) was used to trap radicals in PBS/methanol (50/50/, v/v). 5-(2,2-dimethyl-1,3-propoxycyclo-phosphory-

l)-5-methyl-1-pyrroline N-oxide (CYPMPO, 1 mM) was used for $NAD^{\bullet}$ radicals in PBS/methanol (50/50/, v/v) solution containing complex **1** (50 μM, methanol) and NADH (10 mM, PBS) under 463 nm irradiation. 2,2,6,6–Tetramethyl-piperidine (TEMP 10 mM) was used to trap singlet oxygen from complex **1** in methanol upon 463 nm blue light excitation.

6. Determination of singlet oxygen quantum yield

An air-saturated acetonitrile solution, containing the tested compounds (A = 0.1 at irradiation wavelength), *p*-nitrosodimethyl aniline (RNO, 24 μM), imidazole (12 mM). An air-saturated PBS buffer solution, containing the complex (A = 0.1 at irradiation wavelength), RNO (20 μM), histidine (10 mM) were irradiated in a luminescence quartz cuvette at 420 nm, recording the absorbance at various time intervals. Plots of $A_0–A$ at 440 nm in PBS or at 420 nm in acetonitrile (where A_0 is the absorbance before irradiation) versus the irradiation time were prepared and the slope of the linear regression was calculated (S_{sample}). As a reference compound, phenalenone (Φ_{ref} ($^1O_2$) = 95 %)[10] was used to obtain S_{ref} Equation (1) was applied to calculate the singlet oxygen quantum yields (Φ_{sample}) for every sample:

$$\Phi_{sample} = \Phi_{ref} * S_{sample}/S_{ref} * I_{ref}/I_{sample} \quad (1)$$

$$I = I_0 * (1 - 10^{-A_\lambda}) \quad (2)$$

I (absorbance correction factor) was obtained from Equation (2), where I_0 is the light intensity of the irradiation source in the irradiation interval and A_λ is the absorbance of the sample.

7. Computational details

7.1 Density functionals

All calculations were performed using a local version of the Gaussian16 program suite[11]. All density functional computations were carried out with the dispersion-corrected B3LYP-D3BJ functional. The Becke-Johnson damped D3 dispersion correction was added given the NADH-**1** interaction complexes studied (*vide infra*). This functional was also calibrated against other functionals with differing amounts of exact exchange for other properties such as complex **1** geometries, isomeric energetics, and excitation energies (relative to experimental band maxima). It performed consistently across these, so was used for all calculations discussed below. The Def2-TZVPP basis was coupled with a Stuttgart-Dresden

(SDD) effective core potential for the iridium (60 core electrons). This basis is property optimized and has previously been shown to give an excellent cost-to-accuracy balance for related properties to those under study in this work[12]. The SMD solvent model was chosen as this can provide robust redox potentials as discussed below. Minima were confirmed by noting a positive definite geometrical Hessian matrix obtained by analytical differentiation.

7.2 Ground and excited state geometries.

Two isomers of **1** are possible, each distinguished by the phenylisoquinoline N or C *trans* to the Cl. The C-Cl *trans* isomer is 33.5 kJ mol^{-1} lower in energy so was used for all subsequent theoretical investigations. This configuration is observed in the x-ray crystal structure (Fig. 1b). Table S6 shows selected geometrical parameters for each of the ground state singlet and excited triplet geometries. Excited electronic states were obtained via time-dependent (TD) linear response calculations for the first thirty singlet and triplet states. Table S3 shows the excitation energies, oscillator strengths, and characterization for the lowest excited states. Fig. S2 shows a simulated one-photon absorption spectrum of **1** in vacuum and various solvents, while Fig. S6 shows the canonical frontier orbitals.

7.3. Two-photon absorption cross section

The two-photon absorption cross section was calculated using the non-resonant 3-state sum-over-states model of Ågren *et al.*,[13] using the linear response ground-to-excited transition moments, and the approximate excited-to-excited transition moments obtained from the *a posteriori* Tamm–Dancoff approximation (ATDA)[14].

The two-photon absorption spectra of complex **1** were determined over a broad spectral region by the typical two-photon induced luminescence (TPL) method relative to Rhodamine B in methanol as the standard devised by Webb and Xu[15]. The two-photon luminescence data were acquired using an Opolette™ 355II (pulse width ≤ 100 fs, 80 MHz repetition rate, tuning range 700-800 nm, Spectra Physics Inc., USA). Two-photon luminescence measurements were performed in fluorometric quartz cuvettes. The experimental luminescence excitation and detection condition were conducted with negligible reabsorption processes, which can affect TPA measurements. The quadratic dependence of two-photon induced luminescence intensity on the excitation power was verified at an excitation wavelength of 760 nm. The two-photon absorption cross section of the probes was calculated at each wavelength according to equation (3):

$$\delta_2 = \delta_1 \frac{\phi_1 C_1 I_2 n_2}{\phi_2 C_2 I_1 n_1} \qquad (3)$$

where I is the integrated luminescence intensity, C is the concentration, n is the refractive index, and Φ is the quantum yield. Subscript '1' stands for reference samples, and '2' stands for samples.

7.4. Redox and photo-redox potentials

The calculated redox and photo-redox potentials of **1** were obtained from the Gibbs energies of the singlet and triplet states relative to the optimized ionized and attached electronic states.[16] Standard statistical thermodynamics models were used for the entropic contributions to the free energies. Absolute standard potentials were obtained from the solvated free energies at 293 K via:

$$E^0_{Abs} = -\frac{\Delta G_{red}(sol)}{nF} - 0.03766 \qquad (4)$$

where n is the number of electrons transferred (n=1 here), F is the Faraday constant, and $\Delta G_{red}(sol)$ is the Gibbs energy for the solvated reduction half-reaction (obtained directly via the appropriate Born-Haber type cycle), with the last term accounting for the Gibbs free electron correction at 293 K. The particular protocol has previously been used successfully for calculating challenging aqueous copper complex redox potentials[17], and the SMD solvent model in particular has been shown to be robust and provide accurate such properties from DFT calculations. Conversions from absolute potentials to those versus the SCE were made by first correcting to versus SHE via the optimized SMD model shift of +4.28V[18], followed by a standard correction of +0.241V from SHE to SCE.

7.5. Interaction between complex 1 and NADH

DFT calculations provided two structures for the closed interaction complex between **1** and NADH. Several of these were optimized starting at four possible 'clamped' sites with the NADH around each of the conjugated hetero-aromatic units. The structure in Fig. 3d shows the triplet **1**-NADH interaction complex around the phenylisoquinoline (with maximum hole amplitude), and one of two symmetric triplet **1**-NADH interaction complexes around the terpyridine (with maximum particle amplitude). These geometries (which are stable minima in both singlet and triplet states) are likely to facilitate the photo-redox electron transfer processes.

7.6. Photocatalytic reduction of Fe^{3+}-cyt c by complex 1 and NADH. Photocatalytic reduction of oxidized Fe^{3+}-cyt c (11.2 μM) by **1** (0.6 μM) in the presence of NADH (50 μM) was studied by UV-vis spectroscopy at 310 K in the dark or on irradiation with 463 nm light. The PBS solution was degassed by sonication for 10 min followed by purging with N_2 for 30 min. Stock solutions of Fe^{3+}-cyt c (10 mM in PBS), NADH (100 mM in PBS) and complex **1** (1 mM in DMSO) were added under a N_2 atmosphere. TON is defined as the number of moles of Fe^{3+}-cyt c that a mole of **1** can convert within 30 min. TOF was calculated from the difference in Fe^{3+}-cyt c concentration after 30 min divided by the concentration of complex **1**. The concentration of Fe^{3+}-cyt c was determined using the extinction coefficient ε_{550} = 29.5 $mM^{-1}cm^{-1}$; (reduced form), ε_{550} = 8.4 $mM^{-1}cm^{-1}$ (oxidized form).

8. Cell culture and cell assays

8.1. Cell culture

A549 human lung carcinoma and normal human lung fibroblast cell line MRC-5 were obtained from the European Collection of Cell Cultures (ECACC). Human lung cancer cell line NCI-H460, human cervix cancer cell line HeLa and human liver cancer cell line Hep G2 were obtained from the American Type Culture Collection (ATCC, Manassas, VA). Human gastric cancer cells SGC-7901 and the human hepatocyte cell line LO2 were purchased from the Experimental Animal Center, Sun Yat-sen University (Guangzhou, China). A549, MRC-5 and LO2 cell lines were grown in Roswell Park Memorial Institute medium (RPMI-1640) supplemented with 10% fetal calf serum, 100 μg/mL streptomycin and 100 U/mL penicillin. NCI-H460, HeLa, Hep G2 and SGC-7901 cell lines were grown in Dulbecco's Modified Eagle Medium (DMEM) supplemented with 10% fetal calf serum, 100 μg/mL streptomycin and 100 U/mL penicillin. These cells were grown as adherent monolayers at 310 K in a 5% CO_2 humidified atmosphere and passaged at 70-80% confluence.

8.2. Dark- and photo-cytotoxicity assays

For adherent cells, 5000 cells were seeded per well in 96-well plates (Costar) at 310 K in a 5% CO_2/95% air incubator (Thermo) for 24 h. The cells for hypoxic treatment were then transferred to an hypoxic incubator, placed in a biological safety cabinet within a glove box (Lonyue, Shanghai) at 310 K, 1% O_2, 5% CO_2 and 94% N_2 for another 24 h allowing the cells to adapt to hypoxic conditions. Stock solutions of complex **1** was firstly prepared in 5% DMSO (v/v) and a mixture of 0.9% sterilized saline and cell culture medium (1:1 v/v) following serial dilutions with cell culture medium. A stock solution of cisplatin (2 mM) was freshly prepared in sterilized saline, and 5-aminolevulinic acid hydrochloride (5-ALA, 100 mM) was freshly prepared in cell culture medium. The drug exposure period was 2 h for complex **1**, 4 h for 5-ALA and 48 h for cisplatin. After this, the supernatants of cells treated complex **1** and 5-ALA were removed by suction and replaced with fresh medium. For dark treatment after drug exposure, the medium was replaced with drug-free cell culture medium. For light treatment, the cells were then irradiated in phenol-red-free cell culture medium under normoxia (20% O_2, 465 nm, light dose 8.9 J/cm^2) at the University of Warwick or hypoxia (1% O_2, 450 nm, light dose 10.0 J/cm^2) at Sun Yat-sen University. Cisplatin-treated cells were irradiated after 4 h incubation without replacing the medium. After treatment, the cells were left to recover for 46 h in the incubator under 20% O_2 or 1% O_2 at 310 K. Finally, the photo-cytotoxicity under normoxia was determined by the sulforhodamine B (SRB) assay[19] on a GloMax-Multi Microplate Multimode Reader at the University of Warwick. The photo-cytotoxicity under hypoxia was evaluated using the MTT assay[20] on a microplate spectrophotometer (Biorad). All the IC_{50} values (concentrations which caused 50% of cell death) were determined as duplicates of triplicates in two independent sets of experiments and their standard deviations were calculated.

For 3D spheroid models, A549 lung multicellular spheroids (MCSs) were cultured using the liquid overlay method. A549 cells in exponential growth phase were dissociated by trypsin/EDTA solution to gain single-cell suspensions. Aliquots of 3000 A549 cells were transferred to cell-repellent surface U-bottom 96 well plates (650970, Greiner bio-one, Germany) with 200 μL of cell culture medium. These cells were left in an incubator with 5% CO_2 in air at 310 K and gradually formed A549 MCS ca. 800 μm in diameter after 1 week of incubation. After 6 h incubation with various doses of complex **1**，cisplatin or 5-ALA, the spheroids were then either left in the dark or received light irradiation. For light treatment, the MCS were irradiated by 760 nm two photon light (10 s/section, section interval = 3 μm, light dose = 12 J cm^{-2}) using a pulsed laser from confocal microscopy (LSM 710, Carl Zeiss, Göttingen, Germany). After 66 h incubation at 20% O_2, 310 K, the photo-cytotoxicity was determined by CellTitler-Glo® 3D Cell Viability kit (Promega). The results were processed as duplicates of triplicates in two independent sets of experiments and their standard deviations were calculated.

8.3. Cellular localization assays

A549 cells were seeded in a glass-bottom dish (35 mm dish with 20 mm bottom well (Costar) at 310 K in a 5% CO_2/95% air incubator. The cells were incubated with complex **1** (5 μM) at 310 K for 1 h and further stained with 100 nM MTR and LTG. Cell imaging was visualized by confocal microscopy (LSM 710, Carl Zeiss, Göttingen, Germany) with a 63× oil-immersion objective lens immediately. Excitation/emission: **1** one-photon 405/562 nm and two-photon 760/562 nm, LTG 488/520 nm, MTR 633/660 nm.

8.4. ICP-MS assays[22]

Exponentially growing A549 cells were harvested, and the resulting single-cell suspension was plated into 100 mm tissue culture plates (Costar). After 24 h at 310 K 5% CO_2/95% air incubator, the cells were treated with 5 μM complex **1** for 2 h at 310 K in full RPMI-1640 cell culture medium. The cells were rinsed with PBS, detached with trypsin, counted and divided into three portions. Using the first portion, the nuclei were extracted using a nucleus extraction kit (Pierce, Thermo) following the manufacturer's protocol; for the second portion, the cytoplasm was extracted using a cytoplasm extraction kit (Pierce, Thermo); and for the third portion, the mitochondria were extracted using a mitochondrial extraction kit (Pierce, Thermo). The cell fractions were digested with 60% HNO_3 at ambient temperature for one day. Each sample was diluted with MilliQ H_2O to achieve 2% HNO_3 sample solutions. The iridium content was measured using inductively coupled plasma mass spectrometry. The Ir concentrations in different cell components were determined as duplicates of

triplicates, as part of two independent experiments, and the standard deviations were calculated. Statistical significances were determined using Welch's *t*-test.

8.5. Phosphorescence lifetime imaging microscopy (PLIM)[23]

A549 cells were seeded in a 35 mm glass bottom dish (Costar) and treated with complex **1** (5 μM) for 1 h followed by washing with fresh cell culture medium. PLIM was conducted by using a TI: SAPPHIRE pulsed laser (Coherent Chameleon) on a confocal microscope (LSM 710, Carl Zeiss, Göttingen, Germany) combined with a time-correlated single photon counting system (Becher & Hickl). The data were processed using SPCImage software (Becker & Hickl). The two-photon excitation wavelength for complex **1** was 760 nm. Emission filter: 565 ± 20 nm.

8.6. Intracellular ROS measurement

The production of intracellular ROS was detected by DCFH-DA. A549 cells were seeded in a 35 mm glass bottom dish (Costar) for 24 h. For hypoxic treatment, the cells were then transferred to an hypoxic incubator located in a glove box (Lonyue, Shanghai) at 310 K in a 5% CO_2/1% O_2 for another 24 h incubation allowing the cells to adapt to hypoxic conditions. The cells were treated with 2× IC_{50} of **1** (normoxia 3 μM, hypoxia 5 μM) for 2 h. Then the cells received dark- or light-treatment as mentioned for the dark- and photo-cytotoxicity assays. Immediately after treatment, the cells were stained with DCFH-DA (10 μM) in serum-free cell culture medium in the incubator for 30 min at 310 K in the dark, and subsequently washed with serum-free cell culture medium. The ROS fluorescence was imaged by an inverted fluorescence microscope (Zeiss Axio Observer D1, Germany) with $\lambda_{ex}/\lambda_{em}$: 488/520 nm**.**

8.7. Two-photon induced ROS generation in A549 multicellular spheroids (**MCSs)**[20]

ROS generation in A549 MCS was verified by using DCFH-DA. A549 MCS were incubated with complex **1** (2 μM) followed by careful washing with PBS and subjected to two-photon irradiation by laser scanning confocal microscopy LSM 710 (760 nm, 10 s/section, section interval = 3 μm). DCFH-DA (10 μM) was added and incubated with MCS at 310 K for 1 h and then subjected to z-axis stack imaging. Excitation/emission: **1** two-photon 760/562 nm, DCF 488/520 nm.

8.8. Intracellular NADH concentration

1×10^4 cells were seeded per well in 96-well plates (Costar) at 310 K in a 5% CO_2/95% air incubator (Thermo) for 24 h. The cells were treated with complex **1** for 2 h. After this, supernatants were removed by suction and each well was washed with 1× PBS. For light treatment, the cells were then irradiated in phenol red-free cell culture medium under normoxia (20% O_2, 465 nm, light dose 8.9 J/cm^2). The cells were

allowed to recover for a further 6 h in an incubator at 310 K. The NAD/NADH-Glo™ kit (Promega) was used to measure the cellular NADH concentration according to the manufacturer's instructions. The luminescence was recorded using a microplate reader (GloMax-Multi Microplate Multimode Reader). The cellular NADH concentrations were determined as duplicates of triplicates, as part of two independent experiments, and the standard deviations were calculated. Statistical significances were determined using Welch's *t*-test.

8.9. Intracellular ATP concentration

1×10^4 cells were seeded per well in 96-well plates (Costar) at 310 K in a 5% CO_2/95% air incubator (Thermo) for 24 h. The cells were treated with complex **1** (2× light IC_{50}, normoxia 3 μM, hypoxia 5 μM) for 2 h. After this, supernatants were removed by suction and each well was washed with 1× PBS. For light treatment, the cells were then irradiated in phenol red-free cell culture medium under normoxia (20% O_2, 465 nm, light dose 8.9 J/cm^2). The cells were allowed to recover for a further 6 h in an incubator at 310 K. Then CellTiter-Glo reagent (Promega) was added to each well, and then the plate was shaken for 2 min, and incubated for 10 min at ambient temperature. The luminescence was recorded using a microplate reader (GloMax-Multi Microplate Multimode Reader). The cellular ATP concentrations were determined as duplicates of triplicates, as part of two independent experiments, and the standard deviations were calculated. Statistical significances were determined using Welch's *t*-test.

8.10. Intracellular H_2O_2 concentration[20]

1×10^4 cells were seeded per well in 96-well plates (Costar) at 310 K in a 5% CO_2/95% air incubator (Thermo) for 24 h. The cells were treated with complex **1** only, or co-incubated with complex **1** and 5 mM N-acetyl-L-cysteine (NAC) for 2 h. After this, supernatants were removed by suction and each well was washed twice with 1× PBS. For light treatment, the cells were then irradiated in phenol-red-free cell culture medium under normoxia (20% O_2, 465 nm, light dose 8.9 J/cm^2). For dark treatment, after drug exposure, the cells were washed and treated with fresh cell culture medium. After irradiation, ROS-Glo™ H_2O_2 kit (Promega) was used to measure the intracellular H_2O_2 concentration according to the manufacturer's instructions. The luminescence was recorded using a microplate reader (GloMax-Multi Microplate Multimode Reader)**.** The cellular H_2O_2 concentrations were determined as duplicates of triplicates, as part of two independent experiments, and the standard deviations were calculated. Statistical significances were determined using Welch's unpaired *t*-test at the 95% confidence level.

8.11. Formazan formation assay

Approximately 1×10^4 cells/well were seeded in 96-well plates, followed by incubation at 310 K 5% CO_2/95% air for 24 h. The cells were treated with serially diluted solutions of complex **1** for 2 h. The supernatants were removed by suction and each well was washed with PBS. For light treatment, the cells were irradiated (20% O_2, 465 nm, light dose 8.9 J/cm^2) in phenol red-free cell culture medium, and the cells were than left to recover in the incubator for another 46 h. For dark treatment, the cells were placed in fresh cell culture medium and kept in an incubator for another 46 h. Finally, 20 μL of MTT solution (5 mg/mL in 1× PBS) was added to each well, followed by incubation for 4 h at 310 K in the incubator. The cells were then imaged by an inverted fluorescence microscope (Zeiss, Germany).

8.12. Mitochondrial membrane potentials ($\Delta\Psi_m$)

The mitochondrial membrane potential was determined by using JC-1 dye. A549 cells were seeded in a 35 mm glass bottom dish (Costar) for 24 h. For hypoxic treatment, the cells were then transferred to a hypoxic incubator located in a glove box (Lonyue, Shanghai) at 310 K in a 5% CO_2/1% O_2 for another 24 h incubation allowing the cells to adapt to hypoxic conditions. The cells were treated with 2× IC_{50} of **1** (normoxia 3 μM, hypoxia 5 μM) for 2 h. Then the cells received dark- or light-treatment as mentioned for the dark- and photo-cytotoxicity assays. Following this, cells were stained with JC-1 (5 μg/mL) at 310 K for 0.5 h and washed with fresh cell culture medium. The cells were imaged by an inverted fluorescence microscope (Zeiss Axio Observer D1, Germany). Excitation/emission: green 488/530 nm and red 488/590 nm.

8.13. Annexin V/PI assay

Cell apoptosis was detected by Annexin V/PI dual staining. A549 cells were seeded in a 35 mm glass-bottom dish (Costar) for 24 h. For hypoxic treatment, the cells were then transferred to an hypoxic incubator located in a glove box (Lonyue, Shanghai) at 310 K in a 5% CO_2/1% O_2 for another 24 h incubation allowing the cells to adapt to hypoxic conditions. The cells were treated with 2× IC_{50} of **1** (normoxia 3 μM, hypoxia 5 μM) for 2 h. Then the cells received dark- or light-treatment as appropriate for dark- and photo-cytotoxicity assays, and were allowed to recover for a further 6 h in the incubator at 310 K. For dark treatment, cells, after drug exposure, were washed and incubated in drug-free cell culture medium at 310 K for 6 h. The cells were subsequently stained with 5 μL annexin V-FITC and 10 μL PI stock solution in the incubator at 310 K for 30 min in the dark. The fluorescence images were obtained on an inverted fluorescence microscope (Zeiss Axio Observer D1, Germany). Excitation/emission: Annexin V 488/530 nm and PI 530/620.

8.14. Calreticulin Immunofluorescence assay

Immunofluorescence assays for calreticulin were carried out using an Alexa Fluor 488 linked–calreticulin antibody to detect any immunogenic-apoptotic cell death induced

by complex **1** upon light irradiation. A549 cells were treated with complex **1** (3 μM) or cisplatin (200 μM) or oxaliplatin (200 μM) at 310 K for 2 h, washed and irradiated with 450 nm light (10 J/cm^2) followed by recovery for 12 h. Then the cells were stained with Alexa Fluor 488 linked–calreticulin antibody (Abcam, Cambridge, UK) without permeabilization and imaged by confocal microscopy (LSM 710, Carl Zeiss, Göttingen, Germany). Excitation/emission: 488/520 nm.

8.15. HMGB1 ELISA assay

An enzyme-linked immunosorbent assay (ELISA) of high mobility group box 1 protein (HMGB1) was performed to check the possibility of immunogenic-apoptotic cell death induced by complex **1** upon light irradiation. A549 cancer cells were incubated with complex **1** (3 μM), cisplatin (200 μM) or oxaliplatin (200 μM) at 310 K for 2 h, washed with PBS and irradiated with 450 nm light (10 J/cm^2) followed by recovery for 12 h. The amount of HMGB1 released from the cells was detected by a HMGB1 ELISA kit according to the manufacturer's instructions (Cloud-clone, Wuhan, China). Statistics were calculated using the two-tailed t-test with unequal variances (Welch's unpaired t-test). $^{*}p < 0.05$, $^{**}p < 0.01$ $^{***}p < 0.001$

Supplementary Table 1. X-ray crystal data and structure refinement for [**1]PF6 1.5(toluene)**

Identification code	sb10
Empirical formula	$C_{47.5}H_{39}ClF_6IrN_4P$
Formula weight	1038.44
Temperature/K	150(2)
Crystal system	triclinic
Space group	P-1
a/Å	12.4658(2)
b/Å	13.2099(2)
c/Å	14.7786(2)
α/°	82.1100(10)
β/°	73.2830(10)
γ/°	64.049(2)
Volume/Å^3	2095.57(6)
Z	2
ρ_{calc}g/cm^3	1.646
μ/mm^{-1}	3.354
F(000)	1030.0
Crystal size/mm^3	0.3 × 0.06 × 0.04
Radiation	MoKα (λ = 0.71073)
2θ range for data collection/°	4.108 to 60.826
Index ranges	-17 ≤ h ≤ 17, -18 ≤ k ≤ 18, -20 ≤ l ≤ 20
Reflections collected	101409
Independent reflections	11731 [R_{int} = 0.0663, R_{sigma} = 0.0363]
Data/restraints/parameters	11731/52/599
Goodness-of-fit on F^2	1.037
Final *R* indexes [$I>=2\sigma(I)$]	R_1 = 0.0332, wR_2 = 0.0763
Final *R* indexes [all data]	R_1 = 0.0432, wR_2 = 0.0823
Largest diff. peak/hole / e Å^{-3}	1.70/-1.36

Supplementary Table 2. Selected x-ray crystallographic bond lengths (Å) and angles (°) for [**1]PF$_6$·1.5(toluene)**.

Bond lengths (Å)	Ir(1)-N(33)	2.051(2)
	Ir(1)-N(17)	2.047(2)
	Ir(1)-N(1)	2.074(3)
	Ir(1)-N(23)	1.949(3)
	Ir(1)-N(33)	2.051(2)
	Ir(1)-Cl(1)	2.4643(8)
Bond angles (°)	C(16)-Ir(1)-N(33)	91.90(10)
	C(16)-Ir(1)-N(17)	91.36(10)
	C(16)-Ir(1)-N(1)	80.33(9)
	C(16)-Ir(1)-Cl(1)	175.09(6)
	N(33)-Ir(1)-N(1)	101.52(10)
	N(33)-Ir(1)-Cl(1)	87.38(8)
	N(17)-Ir(1)-N(33)	160.47(11)
	N(17)-Ir(1)-N(1)	98.01(10)
	N(17)-Ir(1)-Cl(1)	90.93(8)
	N(1)-Ir(1)-Cl(1)	95.05(8)
	N(23)-Ir(1)-C(16)	94.15(10)
	N(23)-Ir(1)-N(33)	80.24(10)
	N(23)-Ir(1)-N(17)	80.32(10)
	N(23)-Ir(1)-N(1)	174.22(10)
	N(23)-Ir(1)-Cl(1)	90.52(8)

Supplementary Table 3. Selected singlet-singlet (S_0–S_n) and singlet-triplet (S_0–T_m) excitations calculated with TD-DFT (in CH_2Cl_2): vertical excitation energies (nm [eV]), response eigenvector coefficients (|c| > 0.18), orbitals involved in the transitions, and oscillator strengths (f) for complex **1** (with f > 0.05), for states up to 4.0 eV.

States	Transitions
Singlet excited states S_n	*n = 1 (LLCT/MLCT)* 525.4 [2.36] (*f* = 0.0089) H→L (0.68) *n = 3 (LLCT/MLCT)* 424.8 [2.92] (*f* = 0.2298) H-1→L (0.62) H→L+1 (0.27) *n = 9 (LLCT/MLCT)* 353.4 [3.51] (*f* = 0.2572) H-4→L (0.68) *n = 11 (LLCT/MLCT)* 343.2 [3.61] (*f* = 0.1480) H→L+3 (0.65) *n = 18 (LLCT/MLCT)* 322.4 [3.85] (*f* = 0.0885) H-8→L (0.50) H-5→L (0.40) H-4→L+1 (0.19)
Exp. em. λ_{max} [b] (nm)	562
Calc. em. λ_{max} [c] (nm)	567
Triplet excited states T_m	*m = 1 (LLCT/MLCT)* 547.9 [2.26] H→L (0.65) H-2→L (0.23) *m = 2 (LLCT/MLCT)* 519.0 [2.39] H-1→L (0.64) *m = 3 (LLCT/MLCT)* 505.9 [2.45] H→L+2 (0.47) H-3→L+2 (0.36)

[a] H = HOMO, L = LUMO [b] recorded at ambient temperature in CH_2Cl_2 [c] calculated as the energy difference between the DFT optimized ground state and lowest triplet stat

Supplementary Table 4. Photophysical properties of complex **1** in various solvents at ambient temperature (293 K).

Solvent	Absorption /nm (log ε)	Emission /nm[a]	Emission quantum yield[b] /%	Emission lifetime/ns air	N_2
CH_2Cl_2	279 (4.89), 320 (4.66), 328 (4.62), 352 (4.20), 410 (4.32)	562	17.84	n.d.	n.d.
CH_3CN	277 (4.89), 321 (4.63), 330 (4.54), 348 (4.23), 375 (4.26)	566	9.74	743.7	1390.3
CH_3OH	277 (4.97), 319 (4.73), 327 (4.67), 350 (4.30), 375 (4.33)	560	11.92	n.d.	n.d.
H_2O	272 (4.78), 320 (4.50), 324 (4.46), 350 (4.30), 405 (3.95)	565	3.89	330.8 (171.6)[c]	382.3

[a] Excitation wavelength 405 nm. [b] In aerobic acetonitrile. [c] In the presence of NADH.

Supplementary Table 5. Electrochemical properties of complex **1** and related complexes in acetonitrile.

Complex	Ground state [a] /V $E_{1/2}$ ($[M]^+/[M]$)	I: $E_{1/2}$	Excited State /V $E_{1/2}$($[M]^+/[M^*]$)[b]	$E_{1/2}$($[M^*]/[M]^-$)[b]
Complex **1**	+1.71	-0.97	-0.48	+1.22
$[Ir(ppy)_2(bpy)]^{+}$ [c]	+1.21	−1.51	−0.85	+0.68
fac-$[Ir(ppy)_3]$ [c]	+0.77	−2.19	−1.73	+0.31
$[Ir(dF(CF_3)ppy)_2(dtbbpy)]^{+}$ [c]	+1.69	−1.37	−0.89	+1.21
$[Ru(bpy)_3]^{2+}$ [c]	+1.29	−1.33	−0.81	+0.77
$[Ru(phen)_3]^{2+}$ [c]	+1.26	−1.36	−0.87	+0.82

[a] All measurements in 0.1 M NBu_4PF_6-CH_3CN, errors in potentials ±0.02 V; T = 293 K scan rate = 100 $mV{\cdot}s^{-1}$ under N_2. Potentials in V vs SCE. [b] Excited state reduction potentials: $E([M^*]/[M]^-) = E_{1/2} + E_{\lambda em}$. Hppy: 2-phenylpyridine; *fac*, facial; bpy, 2,2′-bipyridine; $dF(CF_3)ppy$, 2-(2,4-difluorophenyl)-5-trifluoro-methylpyridine; dtbbpy, 4,4′-di-*tert*-butyl-2,2′-dipyridyl; phen, 1,10-phenanthroline; $E_{1/2}$, half-wave potential (reduction of metal complex), based on peak current I; M, metal complex or photoredox catalyst; * refers to excited state. [c] Values from *Chem. Rev.* **2013**, *113*, 5322-5363.

Supplementary Table 6. DFT optimized parameters for the singlet ground state and first triplet excited state of **1** (atom numbering shown in Supplementary Fig. 11).

		singlet ground state	first triplet excited state
Bond lengths (Å)	Ir – C6	2.030	1.986
	Ir – N3	2.051	2.063
	Ir – N4	1.957	1.962
	Ir – N5	2.051	2.050
	Ir – N58	2.086	2.103
	Ir – Cl	2.471	2.430
Bond angles (°)	Cl – Ir – N3	89.42	87.12
	Cl – Ir – N4	87.78	89.05
	Cl – Ir – N5	89.36	91.44
	Cl – Ir – N58	94.55	93.76
	N3 – Ir – N4	80.42	80.06
	N3 – Ir – N58	99.55	100.95
	N3 – Ir – C6	91.44	89.30
	N4 – Ir – N5	80.42	80.67
	N4 – Ir – C6	97.50	96.46
	N5 – Ir – N58	99.60	98.36
	N5 – Ir – C6	91.53	93.98
	N58 – Ir – C6	80.17	80.81

Supplementary Table 7. Computed redox potentials for complex **1**

Redox	SMD H_2O vs SCE / V
$[M]^+/[M]^0$	-1.362
$[M^*]^+/[M]^0$	+0.657
$[M]^+/[M]^{2+}$	+1.053
$[M^*]^+/[M]^{2+}$	-0.967

Supplementary Table 8. Photocatalytic oxidation of NADH by complex **1** in PBS buffer under various conditions.

Entry	Complex **1** μM	NADH μM	NADH/**1**	Light nm	TON	TOF h^{-1}
1	0	120	-	dark	0	n.a.
2	0	120	-	463	0	n.a.
3	0.6	120	200	dark	0	n.a.
4	3	120	40	dark	0	n.a.
5	6	120	20	dark	0	n.a.
6	0	120	-	463	0	n.a.
7	0.6	120	200	463	20.1	40.2
8	3	120	40	463	16.8	33.6
9	6	120	20	463	11.8	23.6
10	6	240	40	463	22.3	44.6
11	6	360	60	463	26.7	53.4
12	6	480	80	463	32.5	65.1
13	10	480	48	463	50.2	100.4
15	10	480	48	517	18.3	36.6
16	10	480	48	593	1.4	2.8

n.a.= not available.

Supplementary Table 9. Dark- and photo-toxicity towards cancer and normal cell lines (IC_{50}/μM).

Treatment	Normoxia			Hypoxia		
	Dark	Light	PI	Dark	Light	PI
Cell line	**NCI-H460**					
1[a]	16.6±0.9	1.0±0.1	16.6	31.6±3.8	8.7±1.0	3.6
Cisplatin[b]	8.7±0.3	10.4±0.9	n.a.	30.8±0.8	27.0±0.5	n.a.
5-ALA[c]	>10000	>10000	n.a.	>10000	>10000	n.a.
Cell line	**HeLa**					
1[a]	35.4±1.9	1.9±0.3	18.6	43.6±3.3	5.2±0.4	8.3
Cisplatin[b]	7.1±0.8	6.0±0.5	n.a.	15.9±0.8	16.7±0.7	n.a.
5-ALA[c]	>10000	2510±280	>4.0	>10000	>10000	n.a.
Cell line	**SGC7901**					
1[a]	19.9±1.2	1.1±0.1	18.1	23.6±1.5	5.8±0.4	4.0
Cisplatin[b]	10.2±0.7	9.7±0.9	n.a.	26.6±2.5	23.1±1.9	n.a.
5-ALA[c]	>10000	2800±300	>3.5	>10000	>10000	n.a.
Cell line	**Hep G2**					
1[a]	>50	1.9±0.1	>25	>50	3.5±0.3	>14
Cisplatin[b]	9.3±0.8	10.4±1.3	n.a.	28.5±1.4	30.1±2.4	n.a.
5-ALA[c]	>10000	>10000	n.a.	>10000	>10000	n.a.
Cell line	**A549**					
1[a]	43.6±2.5	1.6±0.1	27.2	42.5±2.3	2.3±0.3	18.5
1 + NaN_3[a]	47.3±3.7	3.5±0.4	12.7	44.8±2.3	2.5±0.2	17.9
1 + D-mannitol[a]	44.5±1.6	5.0±0.6	9.5	48.3±1.9	2.2±0.3	22.0
1+NaN_3+D-mannitol[a]	43.5±1.8	7.3±0.8	5.9	46.1±3.2	2.6±0.1	17.8
Cisplatin[b]	8.3±1.2	8.6±0.9	n.a.	25.3±2.6	23.2±2.0	n.a.
5-ALA[c]	>10000	>10000	n.a.	>10000	>10000	n.a.
Cell line	**A549 spheroids**					
Treatment	Normoxia					
	Dark	Light	PI			
1[d]	12.6±1.9	1.3±1.9	9.7			
Cisplatin[d]	61.5±2.8	64.2±2.8	n.a.			
5-ALA[d]	>10000	>10000	n.a.			
Cell line	**MRC-5**			**LO2**		
Treatment	Normoxia			Normoxia		
	Dark[a]	Light[b]	PI	Dark[a]	Light[b]	PI
1[a]	43.2±4.1	2.8±0.2	15.4	31.9±2.0	2.8±0.2	11.4
Cisplatin[b]	12.7±2.2	11.2±1.9	n.a.	13.4±0.9	13.2±1.5	n.a.
5-ALA[c]	>10000	2819±390	>3.5	>10000	3019±420	>3.3

[a]Cells were treated with complex **1** for 2 h, replaced with fresh medium and keep in the dark or received irradiation following 46 h incubation under normoxia or hypoxia at 310 K. [b]Cells

were treated with cisplatin kept in the dark or received irradiation after 4h incubation without replacing the medium and following 44 h under normoxia or hypoxia at 310 K. [c]Cells were treated with 5-ALA for 4 h, replaced with fresh medium and keep in the dark or received irradiation following 44 h incubation under normoxia or hypoxia at 310 K. Light dose: under normoxia 465 nm, 8.9 J/cm^2, under hypoxia 450 nm, 10.0 J/cm^2. [d] Spheroids were incubated with compounds for 6 h without replacing the medium, followed by irradiation with a pulsed laser (760 nm, 10 s/section, section interval = 3 μm, light dose = 12 J/cm^2) by a two-photon confocal microscope, and a further 66 h incubation under normoxia at 310 K. PI = dark IC_{50} / light IC_{50} ; n.a.: not available. All the experiments were performed as duplicates of triplicates (n=6 biologically independent experiments). The error bars were calculated as the S.D. from the mean.

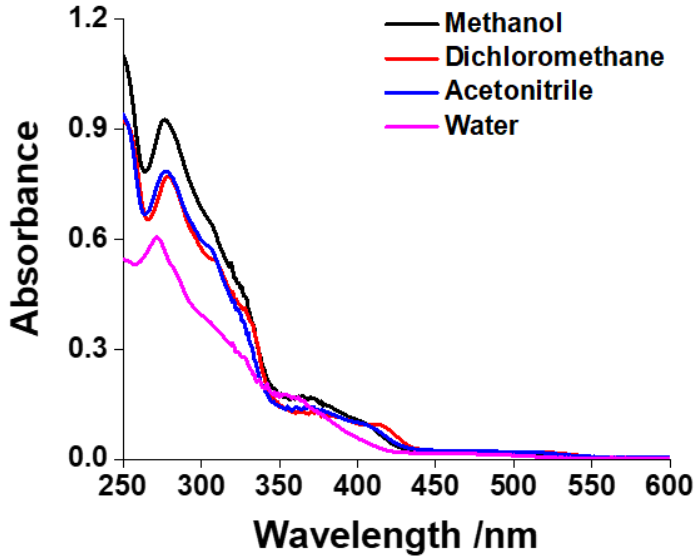

Supplementary Figure 1. UV–vis spectra of complex **1** (10 μM) in various solvents. These experiments were repeated three times independently with similar results.

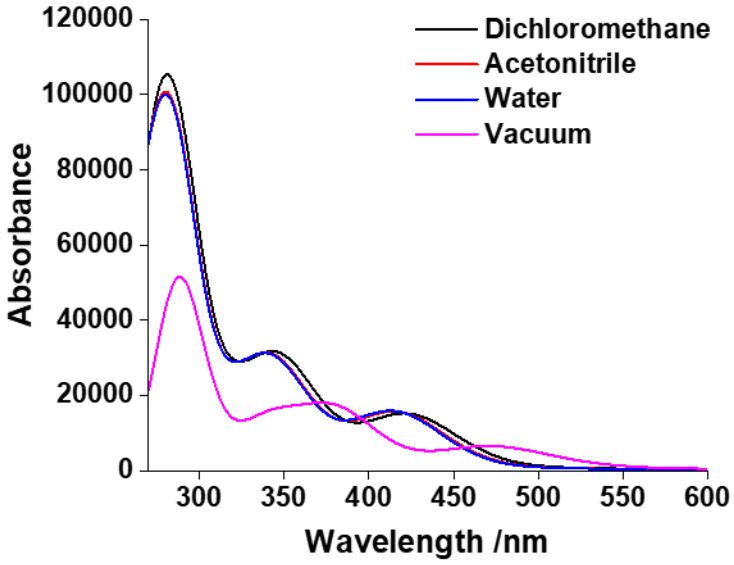

Supplementary Figure 2. Simulated electronic absorption spectrum for **1** in various media obtained with TD-DFT coupled with the SMD solvent model convoluted over 30 singlet electronic states.

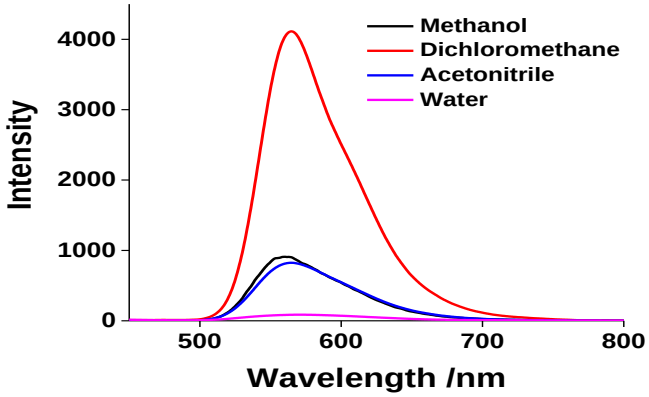

Supplementary Figure 3. Phosphorescence spectra of complex **1** (10 μM) in various solvents, excitation wavelength: 405 nm. These experiments were repeated three times independently with similar results.

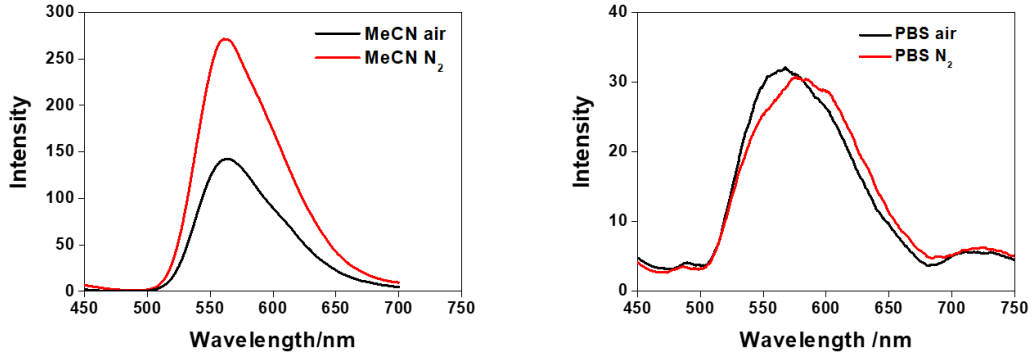

Supplementary Figure 4. Phosphorescence spectra of complex **1** in air or nitrogen-saturated acetonitrile and in PBS at 293 K. Excitation 405 nm. These experiments were repeated three times independently with similar results.

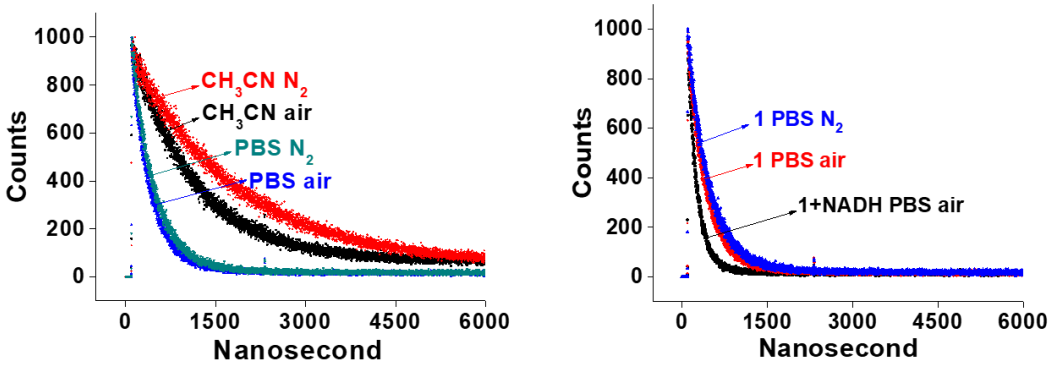

Supplementary Figure 5. Left: Phosphorescence decay curves of complex **1** in N_2-saturated or air-saturated acetonitrile and PBS at 293 K. **Right:** Phosphorescence lifetime spectra of complex **1** in PBS in the presence and absence of NADH. These experiments were repeated three times independently with similar results.

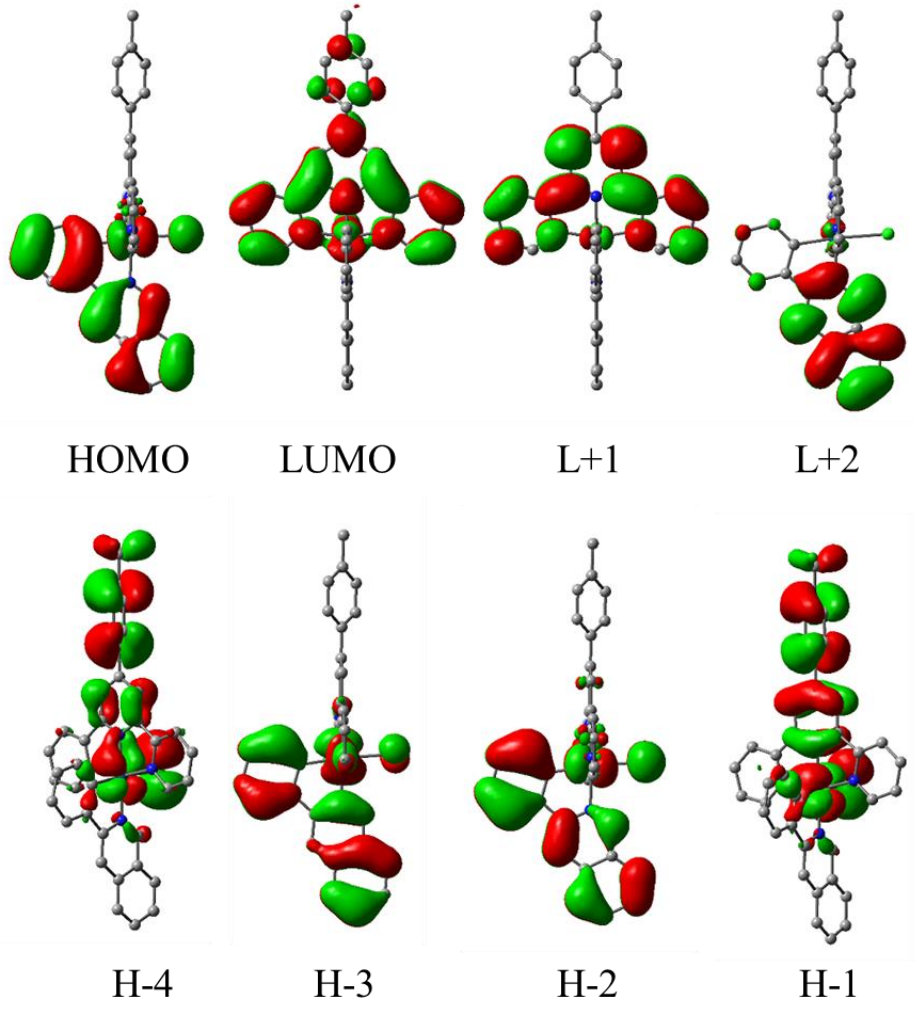

Supplementary Figure 6. Spatial plots of selected frontier orbitals of the DFT optimized ground state of complex **1** (from a single point calculation with CPCM/CH_2Cl_2).

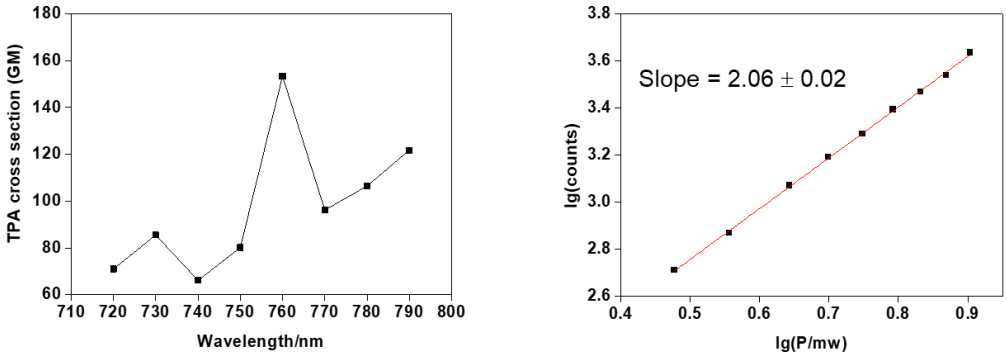

Supplementary Figure 7. Left: Two-photon absorption (TPA) cross-sections of complex **1** in methanol at excitation wavelengths between 700 and 800 nm. **Right**: plot of log intensity versus log power showing quadratic dependence of two photon absorption. These experiments were repeated twice independently with similar results.

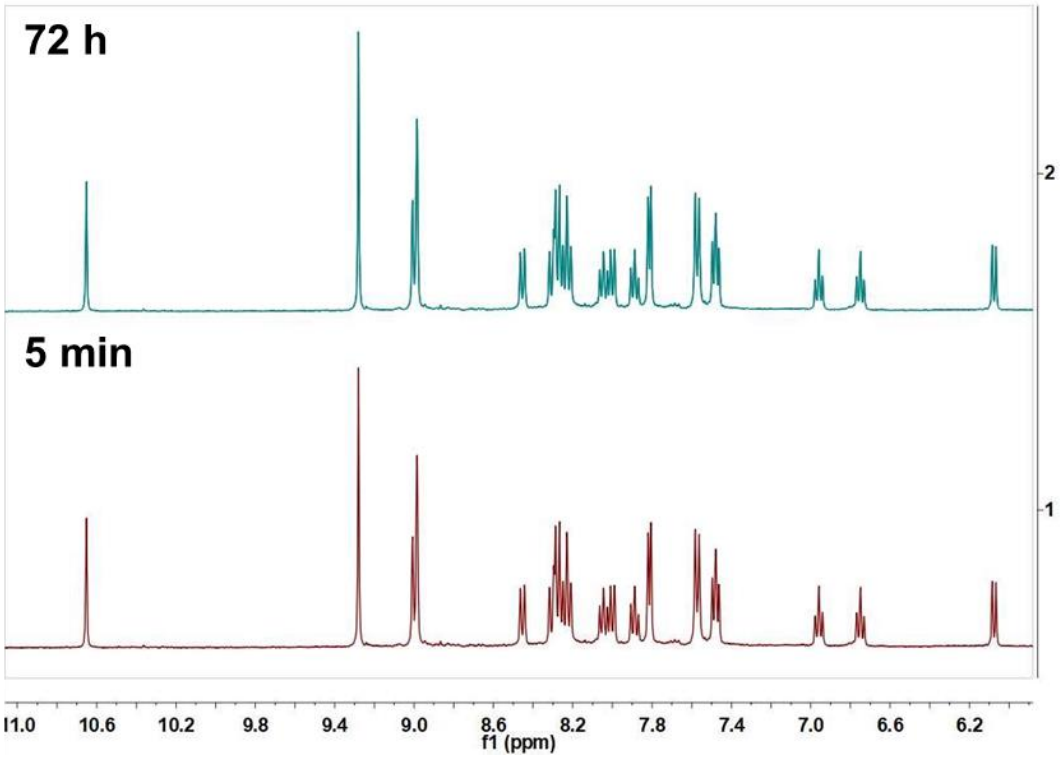

Supplementary Figure 8. Dark stability of complex **1** in a d_6-DMSO stock solution monitored by 400 MHz ^{1}H NMR spectroscopy at 293 K. These experiments were repeated five times independently with similar results.

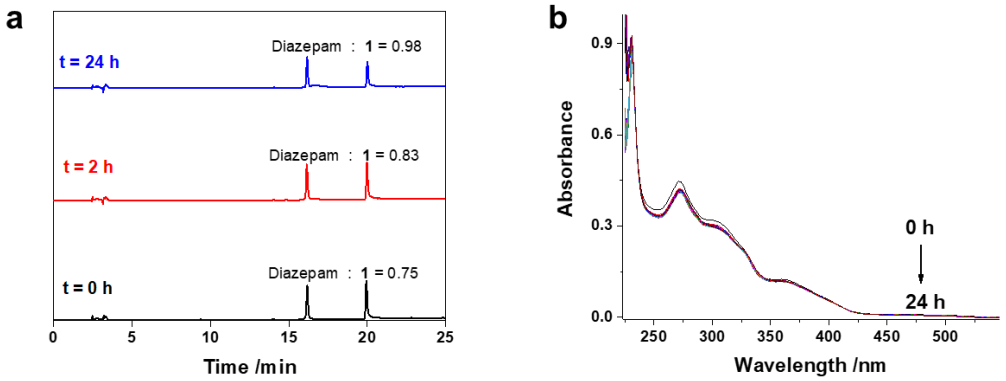

Supplementary Figure 9. Stability of **1** in human serum. (a) High performance liquid chromatography (HPLC) traces (254 nm) for analysis of complex **1** (20 μM) stability in human serum at t = 0, 2 and 24 h. Diazepam was used as internal standard. Ratios of peak area of diazepam/**1** are given with the UV traces. Complex **1** remains stable and did not interact significantly with the blood proteins even after 24 h. (b) UV-vis traces of complex **1** in human serum from 0 to 24 h indicating its prolonged stability. These experiments were repeated twice independently with similar results.

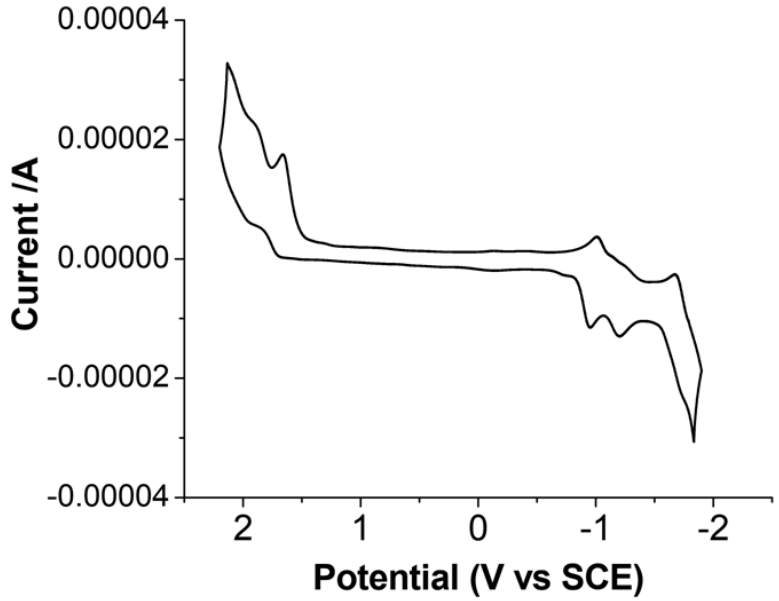

Supplementary Figure 10. Cyclic voltammogram of complex **1** in N_2-saturated acetonitrile containing 0.10 M $(n\text{-Bu})_4NPF_6$, recorded at 0.10 V/s using a three electrode system. Potentials are referenced to SCE via an internal ferrocene standard (Fc/Fc^+= 0.40 V). These experiments were repeated three times independently with similar results.

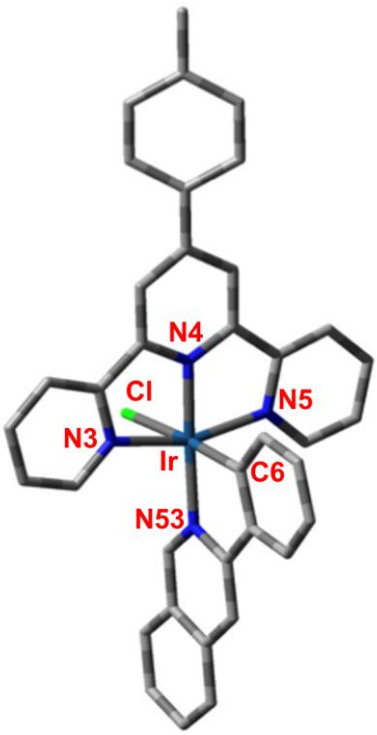

Supplementary Figure 11. DFT-optimized structure for the ground state of **1**. The calculated bond lengths are listed in Table S6.

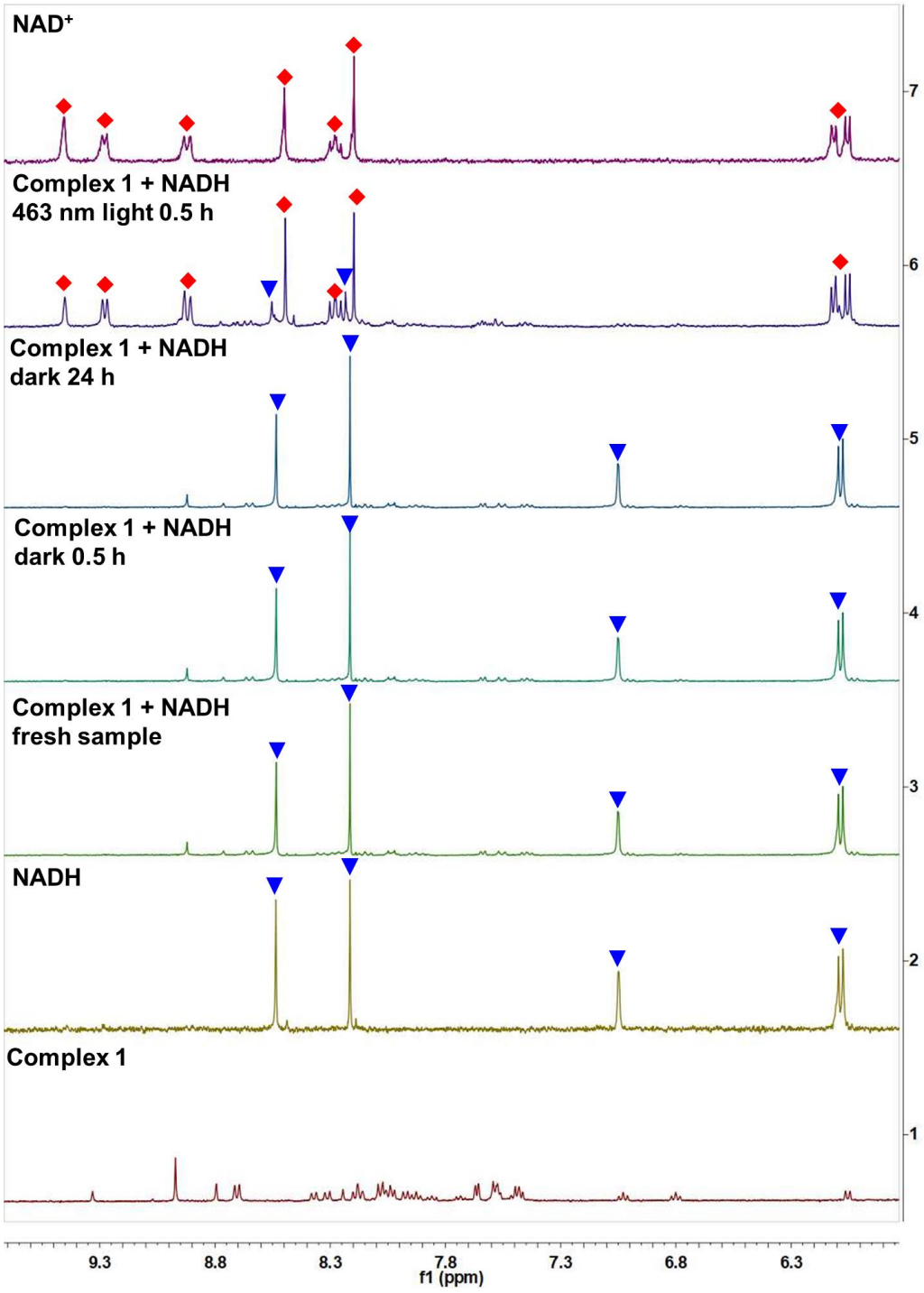

Supplementary Figure 12. Catalytic photo-oxidation of NADH (3 mM) by complex **1** (0.25 mM) in $H_2O/D_2O/d_4$-CD_3OD (0.5/49.5/50, v/v) containing NaCl (4 mM), in the dark or on irradiation with 463 nm blue light for 10 min. The spectra were monitored by 400 MHz ^1H NMR spectroscopy at 293 K. Peaks labelled with blue triangles represent NADH and peaks labelled with red diamonds represent NAD^+. After irradiation, the disappearance of blue triangle peaks and appearance of red diamond peaks confirmed conversion of NADH to NAD^+. These experiments were repeated five times independently with similar results.

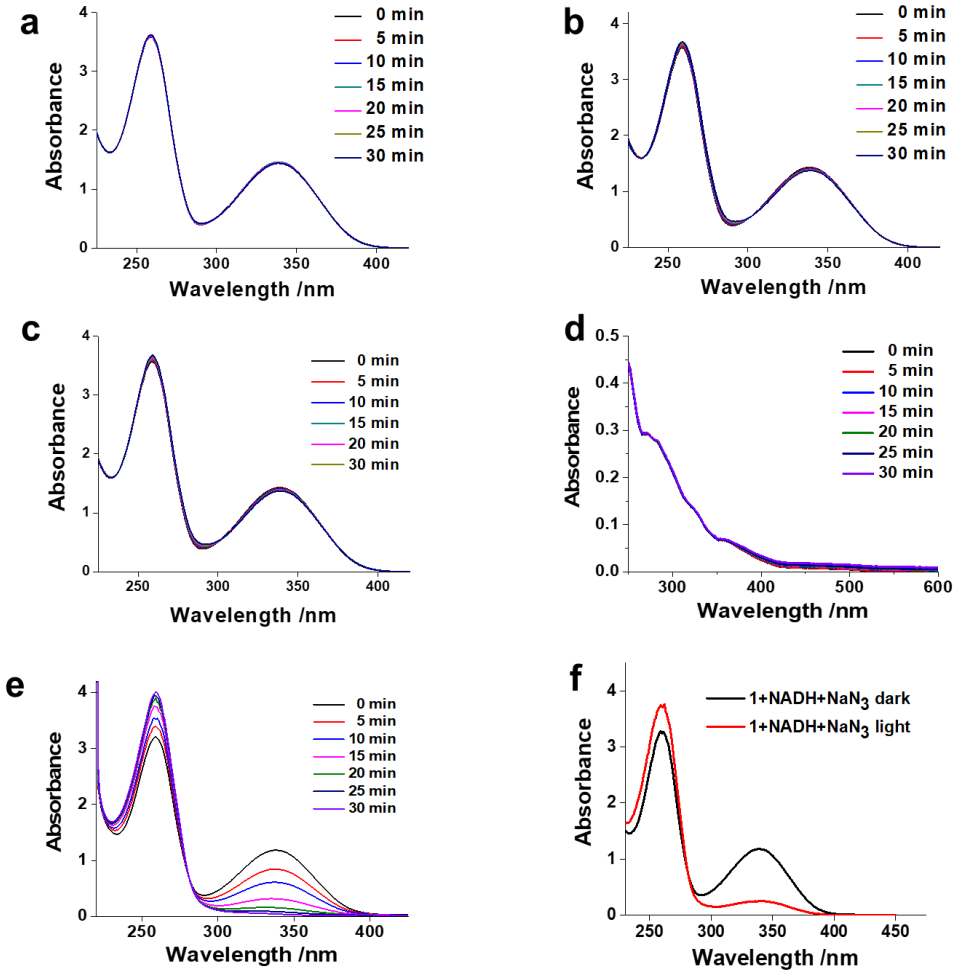

Supplementary Figure 13. UV-vis spectra for the photocatalytic oxidation of NADH (240 μM) by complex **1** (6 μM) in PBS at 293 K.

NADH stability: (a) NADH alone in the dark for 30 min. The spectrum did not change, confirming the high dark stability of NADH. (b) NADH alone under continuous 463 nm blue light irradiation. The spectra remained almost unchanged, showing that NADH was not oxidized during irradiation.

Dark catalytic reaction: (c) UV-vis spectra of NADH in presence of complex **1** in the dark for 30 min. The spectrum of NADH showed no significant change indicating no NADH oxidation in the dark. (d) UV-vis spectra of complex **1** in presence of NADH in the dark. The spectrum remained unchanged indicating that complex **1** did not react with NADH in the dark.

Photo catalytic reaction: (e) UV-vis spectra of NADH in presence of complex **1** in deionized water under continuous 463 nm light irradiation. The decrease of absorbance at 339 nm shows that complex **1** has similar NADH photo-catalytic oxidative activity in deionized water as in PBS. (f) UV-vis spectra of NADH in PBS in presence of complex **1** and 1 mM NaN_3. The significant decrease of absorbance at 339 nm shows that photo-catalytic oxidation of NADH is not induced by singlet oxygen since NaN_3 is an efficient singlet oxygen inhibitor. These experiments were repeated five times independently with similar results.

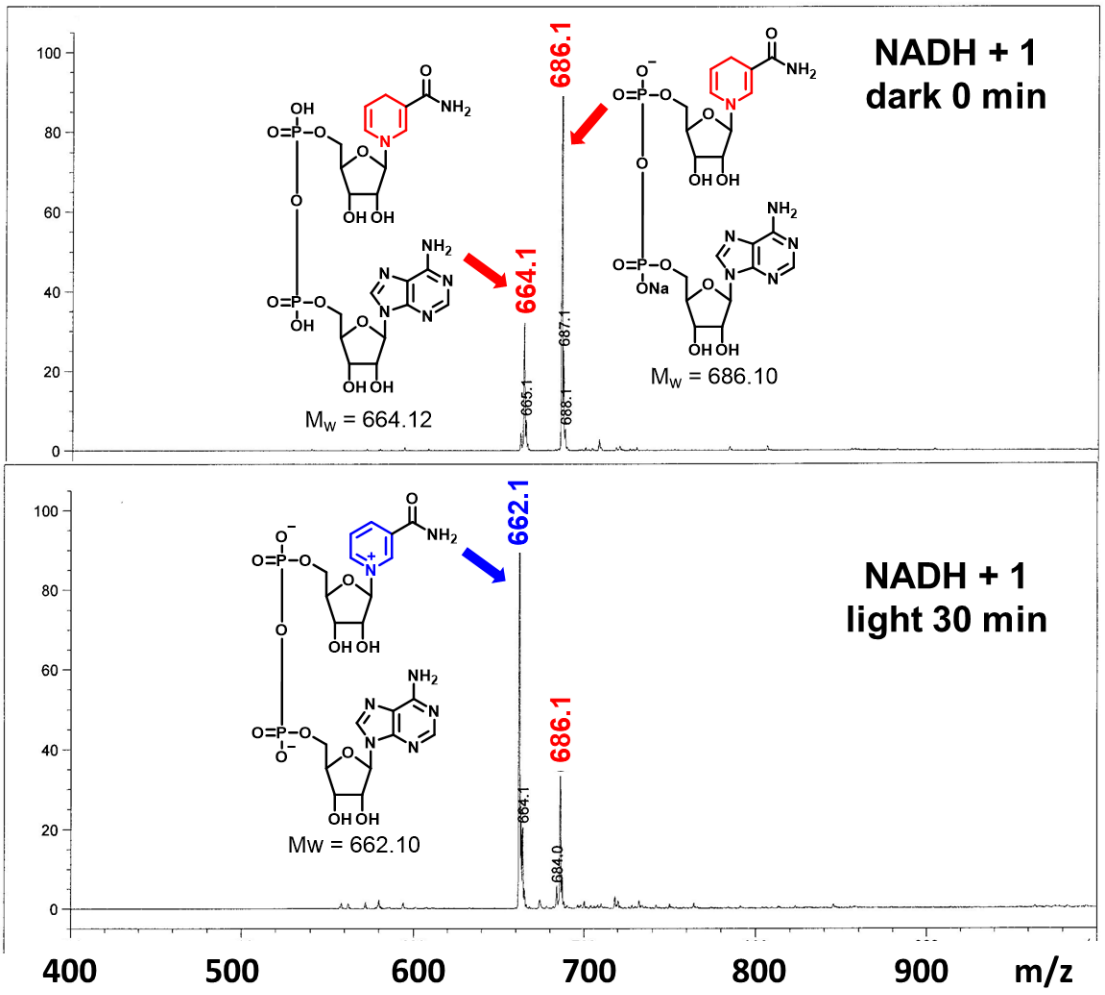

Supplementary Figure 14. Mass spectra (negative mode) monitoring the photocatalytic oxidation of NADH (240 μM) by complex **1** (6 μM) in deionized water upon 463 nm light irradiation at 293 K. These data confirm the generation of NAD^+ after irradiation. These experiments were repeated five times independently with similar results.

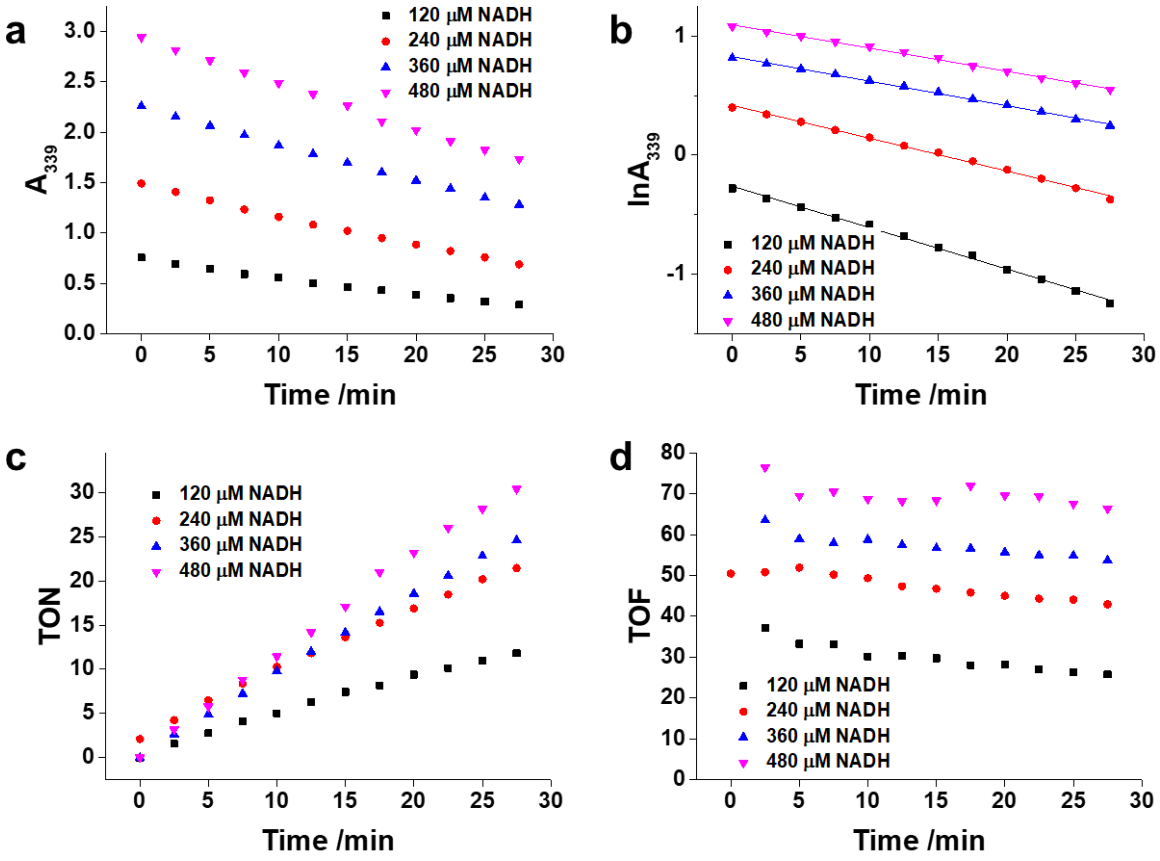

Supplementary Figure 15. Concentration dependence of photo-catalytic reaction of NADH with complex **1** (6 μM) in PBS at 293 K, monitored by UV-vis spectroscopy. a) Time dependence of NADH absorption at 339 nm. b) Plots of lnA_{339} against time, suggesting NADH oxidation follows pseudo first-order kinetics (large excess of NADH). c) Plots of the TON against time. d) Dependence of TOF on NADH concentration. With increasing NADH/**1** ratio, the TOF increased. These experiments were repeated three times independently with similar results.

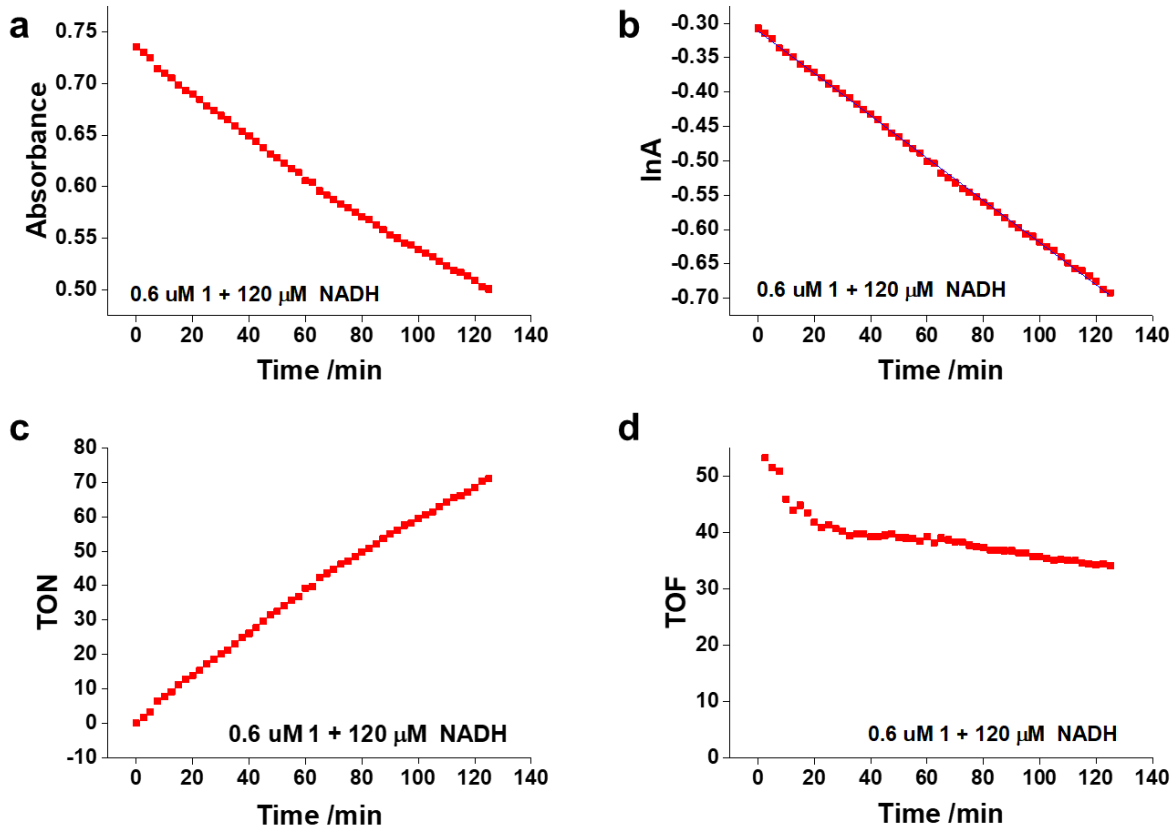

Supplementary Figure 16. Long-term (120 min) photocatalytic oxidation of NADH (120 μM) by complex **1** (0.6 μM) monitored with UV-vis spectroscopy. a) Time dependence of NADH absorption at 339 nm. b) Plots of $\ln A_{339}$ against time suggest that conversion of NADH exhibits first-order kinetics. c) Plots of the TON against time with a large excess of NADH. d) Time dependence of the TOF. During long-term irradiation, complex **1** exhibits excellent photostability since the TON increased linearly with with extension of irradiation time. The TOF decreased slightly during irradiation due to the depletion of NADH. During long-term photocatalysis, complex **1** exhibited extremely high photo stability and TOF (2 h; Fig. S16). The slight decrease in TOF at the end of irradiation was due to consumption of NADH substrate. These experiments were repeated three times independently with similar results.

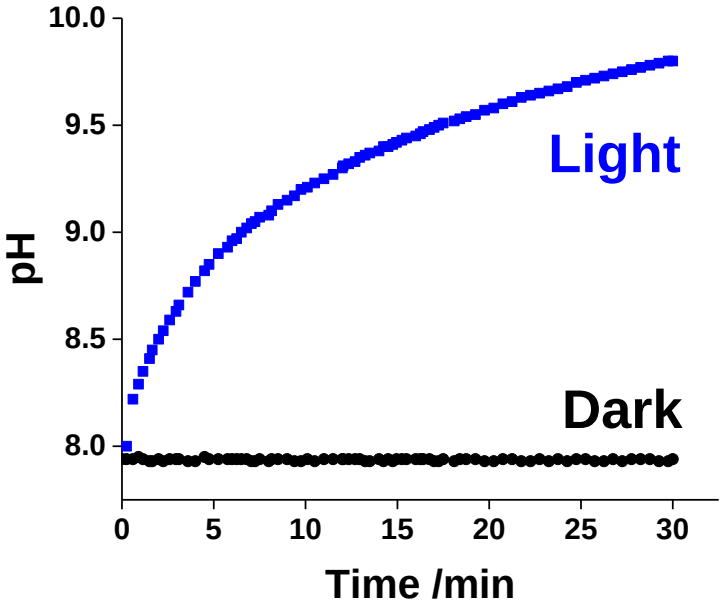

Supplementary Figure 17. pH change during the reaction of NADH (240 μM) with complex **1** (6 μM) in deionized water at 293 K, in the dark and during irradiation with 463 nm blue light. These experiments were repeated three times independently with similar results.

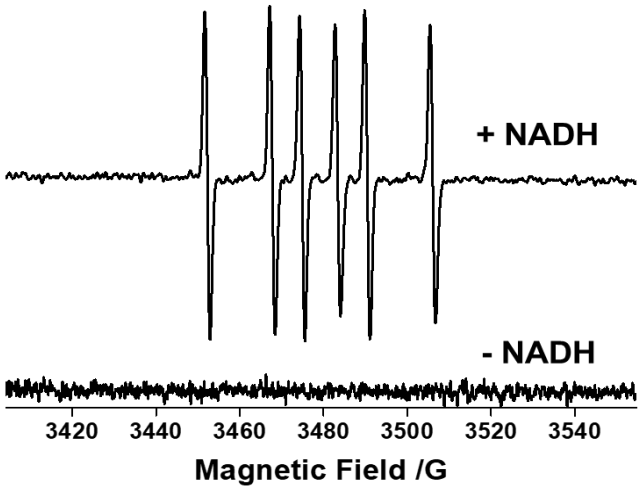

Supplementary Figure 18 X-band EPR spectra of a solution containing complex **1** (500 μM) and DMPO (10 mM) in methanol and PBS (1:1, v/v) in the presence or absence of NADH (5 m M) after irradiation with 463 nm light for 10 min. The DMPO-CH_3 signal was trapped only after irradiation indicating that H_2O_2 is a photocatalytic product. No peaks were observed in the absence of NADH. These experiments were repeated three times independently with similar results.

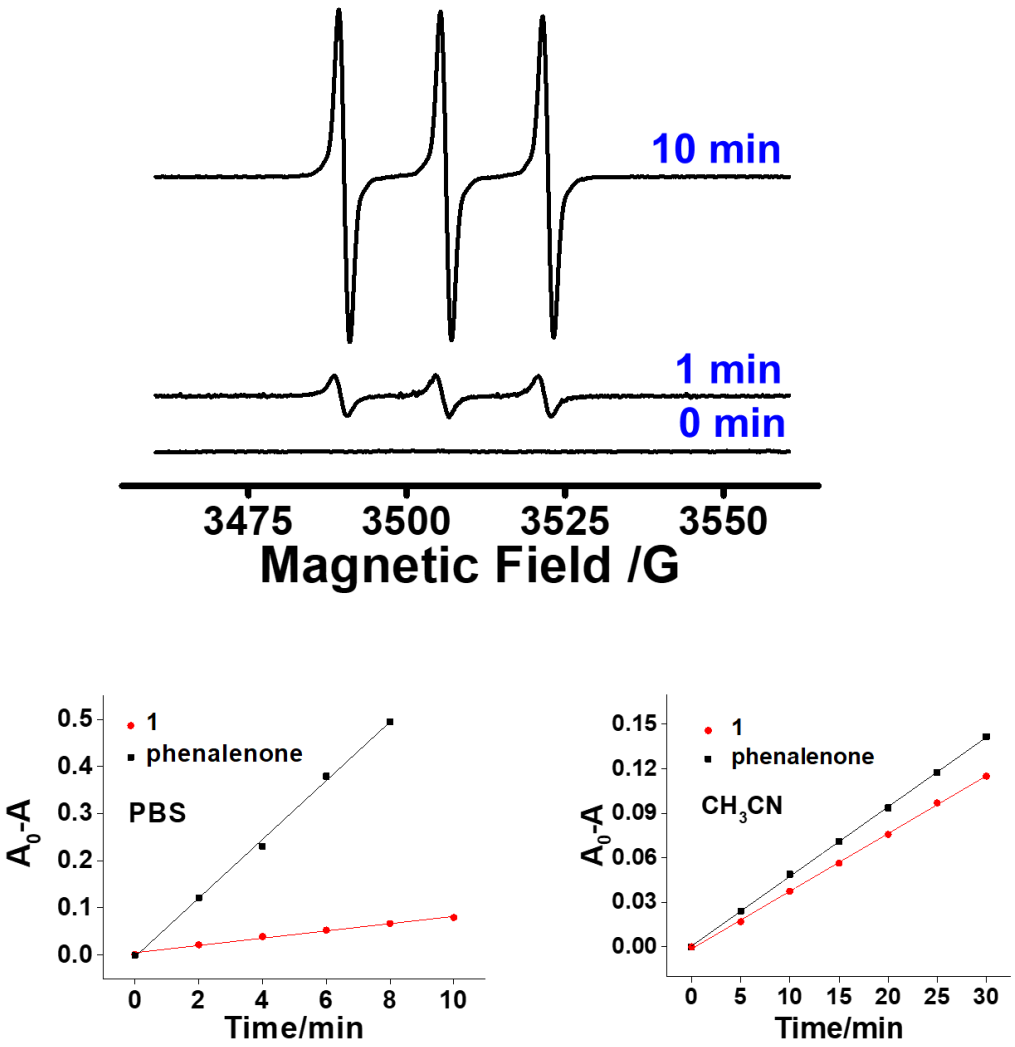

Supplementary Figure 19. Top: X-band EPR spectra of $^1O_2$ trapped by TEMP as TEMP-$^1O_2$ radicals (α_N = 16.12G) in acetonitrile. **Bottom:** Determination of the quantum yield for singlet oxygen generation by complex **1** in PBS solution (left) and in acetonitrile (right) under 463 nm continuous irradiation. The quantum yield was further determined by an indirect method in both PBS (left) and acetonitrile (right). The quantum yield in acetonitrile (Φ = 0.71) is 7x higher than in PBS (Φ = 0.11). The low quantum yield in PBS is due to the lower phosphorescence quantum yield and shorter lifetime in water than in acetonitrile. These experiments were repeated three times independently with similar results.

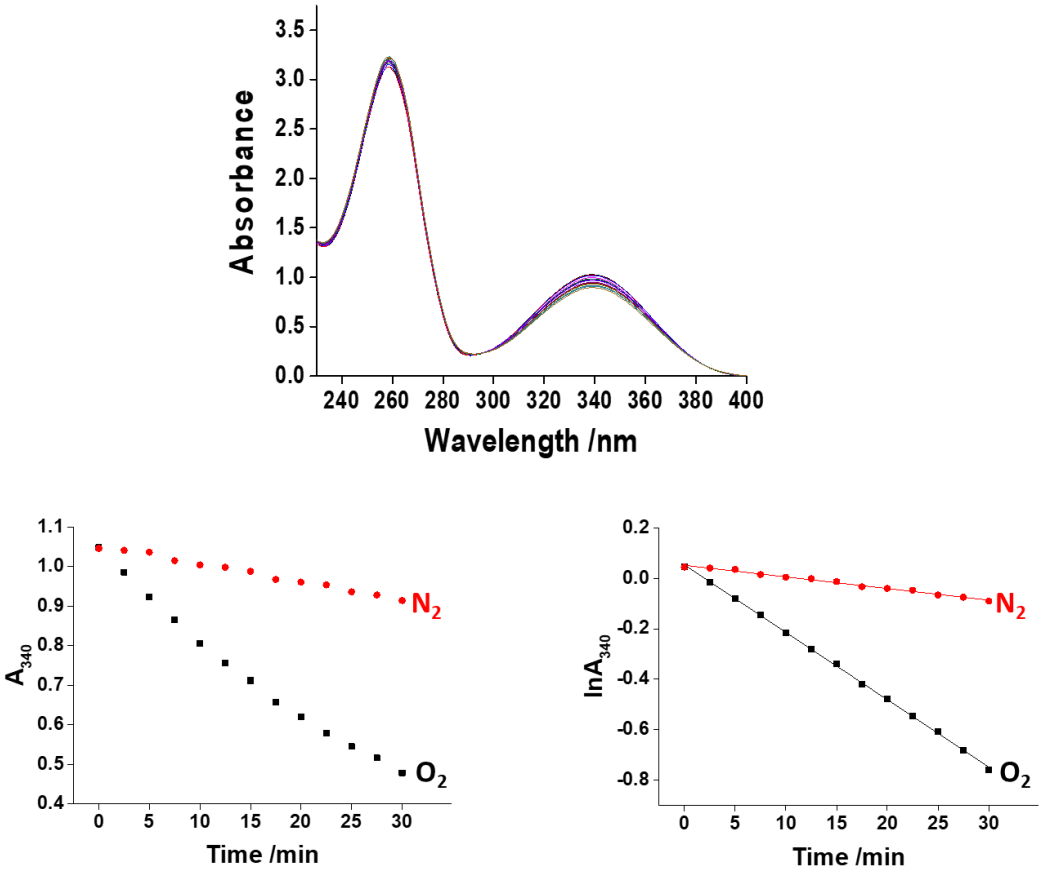

Supplementary Figure 20. Top: UV-vis spectra of NADH (180 μM) and complex **1** (6 μM) in PBS solution under nitrogen during 460 nm light irradiation at 293 K. **Bottom:** Comparison between NADH photocatalytic oxidation under nitrogen and in air. Under nitrogen, the NADH oxidation rate decreased significantly compared with air. A small amount of NADH was oxidized under nitrogen, showing the high oxidative excited state nature of complex **1** and electron transport from NADH to complex **1** as the first step of this photoredox catalytic reaction. These experiments were repeated three times independently with similar results.

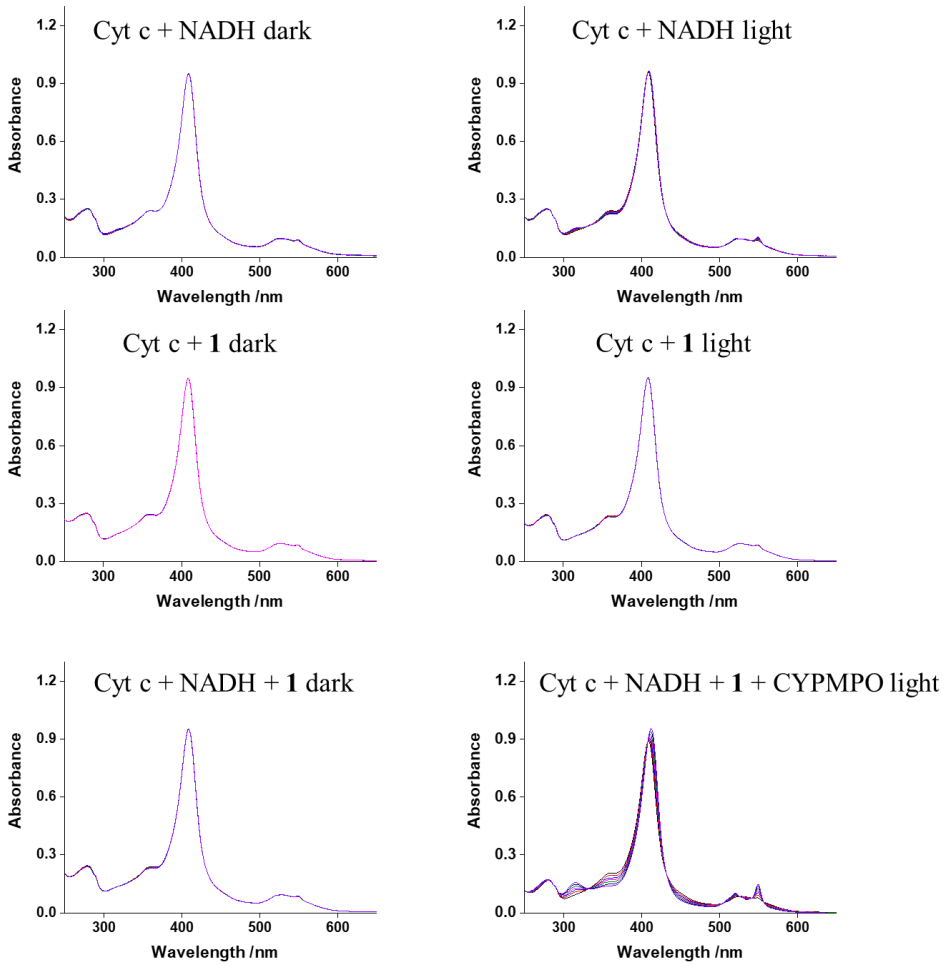

Supplementary Figure 21. Photocatalytic reduction of oxidized Fe^{3+}-cyt c (11.2 μM) by NADH (50 μM) and complex **1** (0.6 μM) under various conditions. Light irradiation: 463 nm. These experiments were repeated three times independently with similar results.

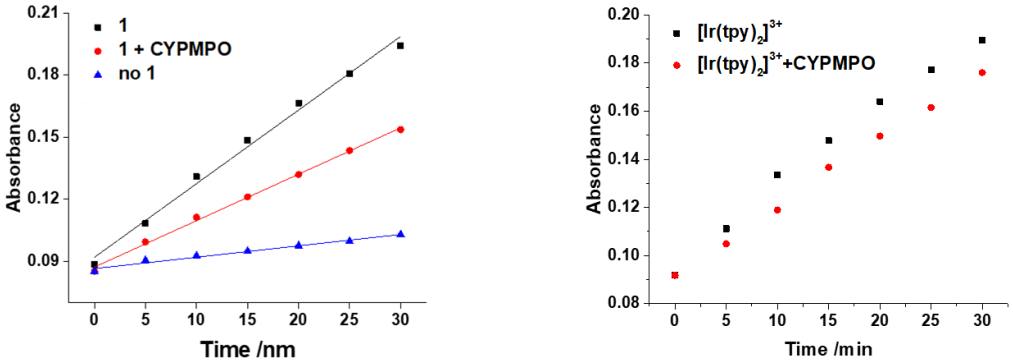

Supplementary Figure 22. Photo-reduction of Fe^{3+}-cyt c (11.2 μM) by complex **1** (0.6 μM, 463 nm) or $[Ir(tpy)_2]^{3+}$ (0.6 μM, 365 nm) in the presence of NADH (50 μM),

and effect of the radical trapping agent CYPMPO (120 μM). These experiments were repeated three times independently with similar results.

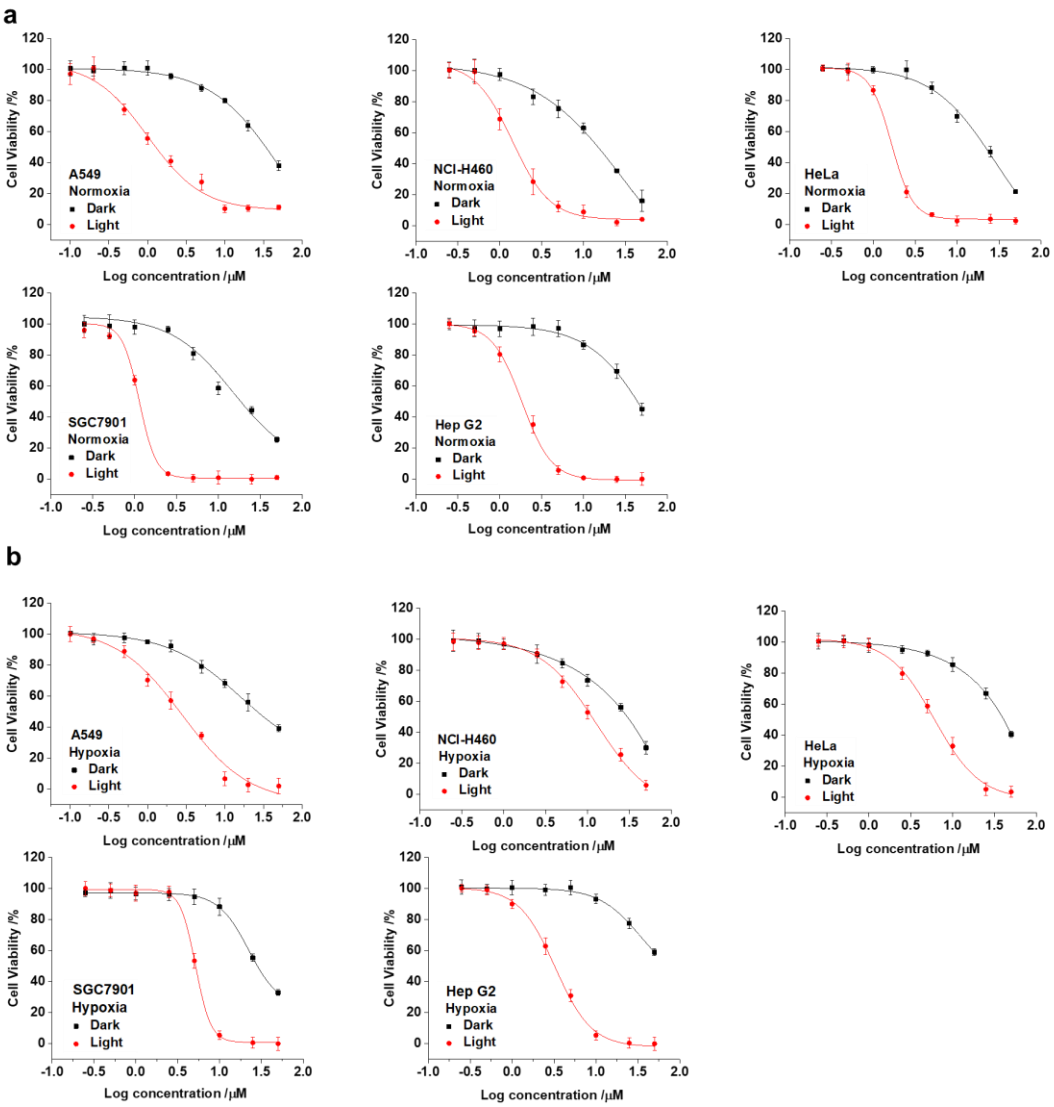

Supplementary Figure 23. Dose-response curves for dark- and photo-toxicity of complex **1** against different cancer cell lines under normoxia (a, 20% O_2) and hypoxia (b, 1% O_2). All the experiments were performed as duplicates of triplicates (n=6 biologically independent experiments). The error bars are ±1 S.D. from the mean.

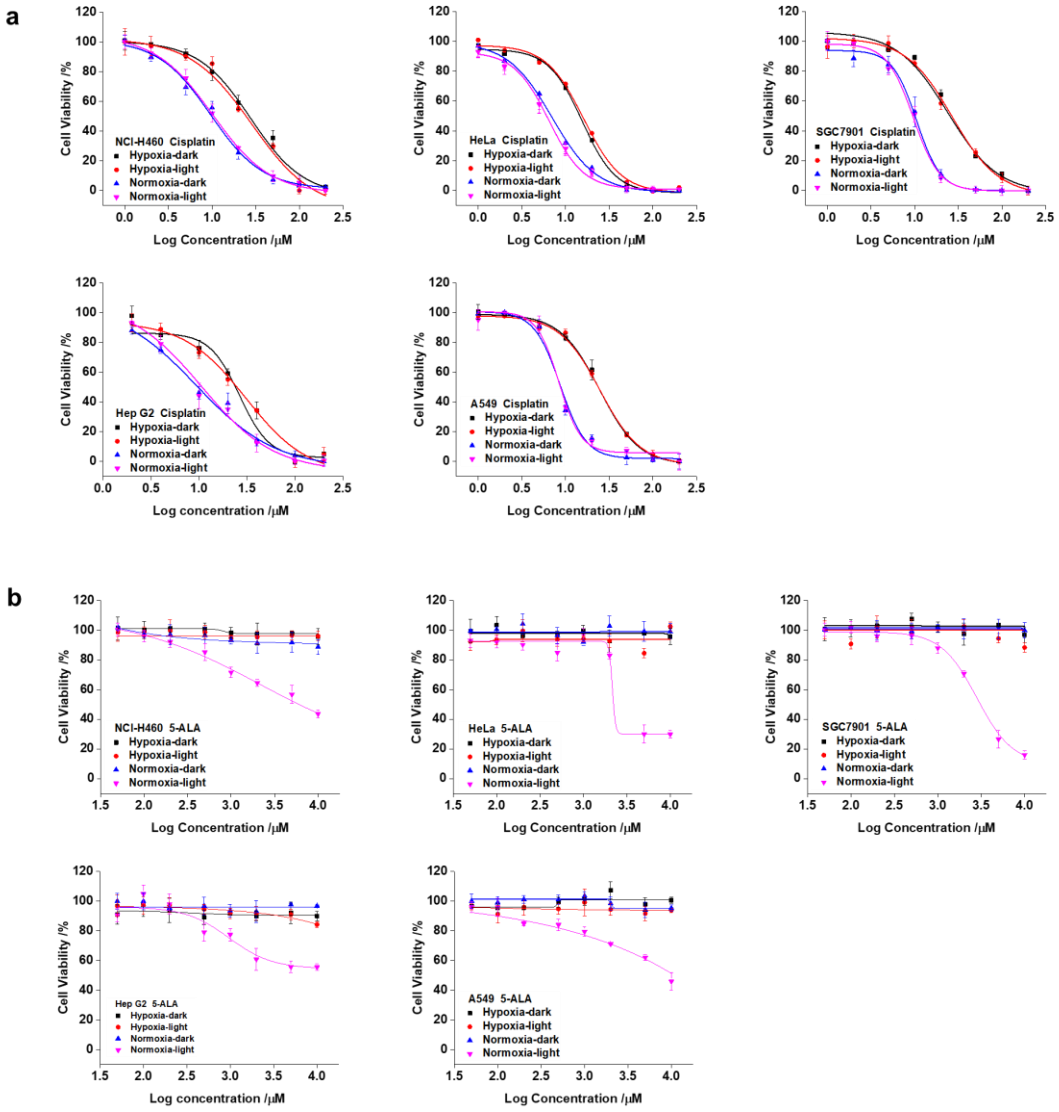

Supplementary Figure 24. Dose-response curves for dark- and photo-toxicity of (a) cisplatin, and (b) 5-ALA towards various cancer cell lines under normoxia (20% O_2) and hypoxia (1% O_2). All the experiments were performed as duplicates of triplicates (n=6 biologically independent experiments). The error bars are ±1 S.D. from the mean.

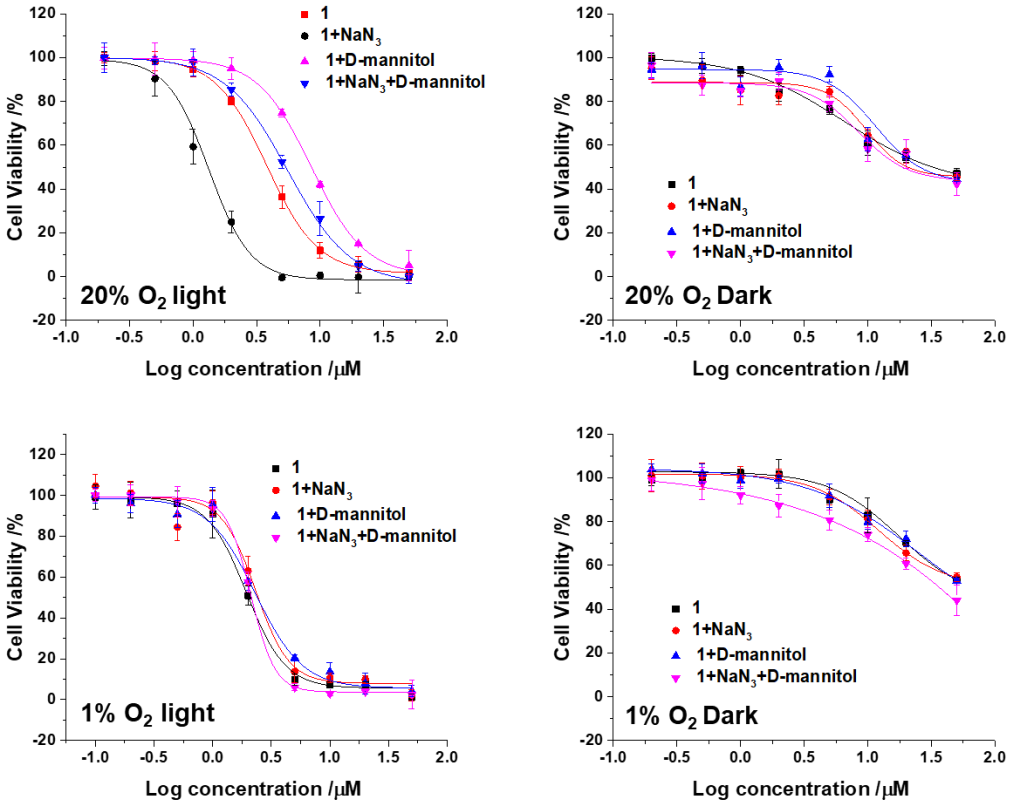

Supplementary Figure 25. Dose-response curves for dark- and photo-toxicity of complex **1** towards the A549 cancer cell line in the presence of different ROS inhibitors under normoxia (20% O_2) and hypoxia (1% O_2). All the experiments were performed as duplicates of triplicates (n=6 biologically independent experiments). The error bars are ±1 S.D. from the mean.

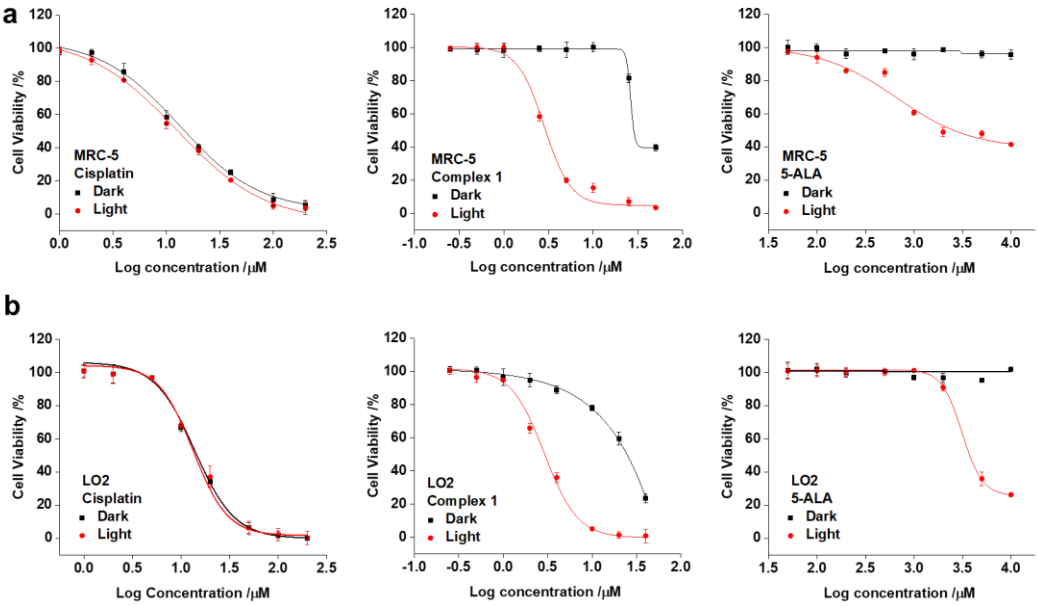

Supplementary Figure 26. Dose response curves for dark- and photo-toxicity of cisplatin, complex **1** and 5-ALA towards (a) MRC-5 normal lung cells, and (b) LO2 normal liver cells under normoxia (20% O_2). All the experiments were performed as duplicates of triplicates (n=6 biologically independent experiments). The error bars are ±1 S.D. from the mean.

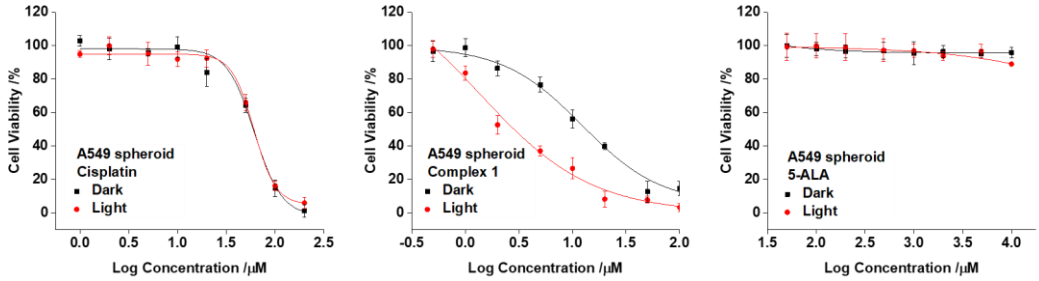

Supplementary Figure 27. Dose-response curves for dark- and photo-toxicity of cisplatin, complex **1**, and 5-ALA towards A549 lung cancer spheroids (ca. 800 μm in diameter). All the experiments were performed as duplicates of triplicates (n=6 biologically independent experiments). The error bars are ±1 S.D. from the mean.

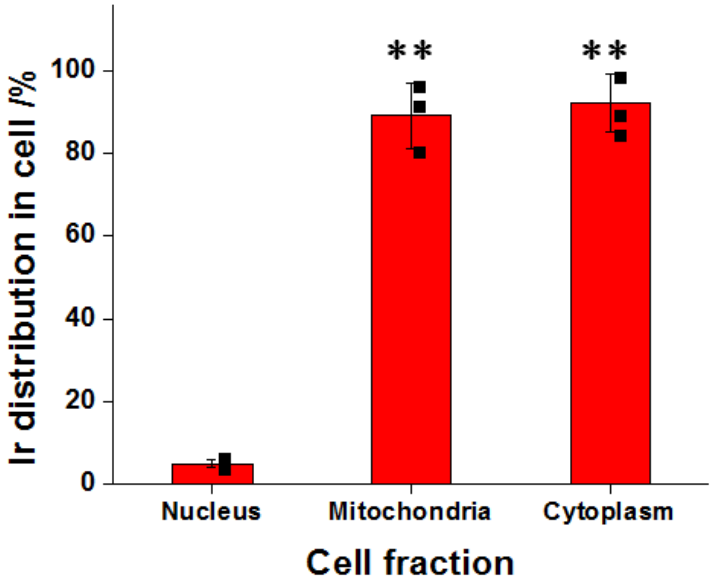

Supplementary Figure 28. ICP-MS quantification of the internalized Ir in A549 lung cancer cells. A549 cells were treated with complex **1** (5 μM) at 310 K for 2 h in the dark and the various cell fractions were separated. All the experiments were performed as duplicates of triplicates (n=6 biologically independent experiments). Error bars show ±1 s.d. from the mean. Statistics were calculated using the two-tailed t-test with unequal variances (Welch's unpaired t-test). $^{*}p < 0.05$, $^{**}p < 0.01$ $^{***}p < 0.001$. p values: mitochondria = 0.0044, cytoplasm = 0.0058.

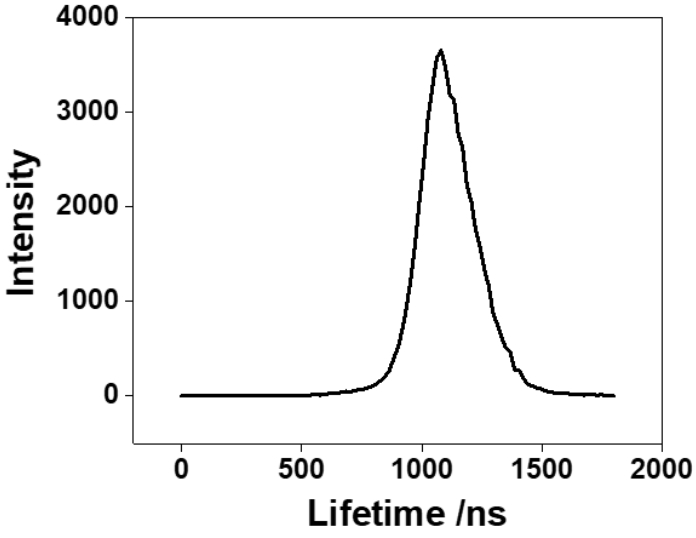

Supplementary Figure 29. Phosphorescence lifetime histogram of complex **1** in A549 cancer cells. Excitation at 760 nm with a pulsed laser. These experiments were repeated twice independently with similar results.

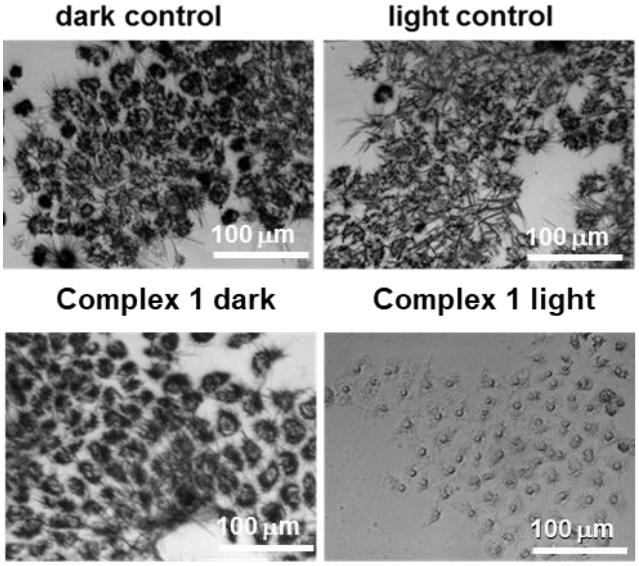

Supplementary Figure 30. Formazan formation in A549 lung cancer cells. The cells were treated with complex **1** (3 μM, 2× IC_{50}) for 2 h, followed by washing and replacing with fresh cell culture medium, and then irradiated (463 nm, 8.9 J/cm^2) or kept in the dark under normoxia. Cells were left to recover for 46 h before adding MTT. Control: without drug treatment. NAD(P)H-dependent cellular oxidoreductase enzymes in mitochondria of living cells are capable of reducing MTT to purple insoluble formazan. Formazan is generated in A549 cells treated with complex **1** in the dark similarly to untreated cells. For the cells receiving irradiation, the formation of formazan reduced significantly, attributable to photocatalytic NADH depletion by complex **1**. These experiments were repeated three times independently with similar results.

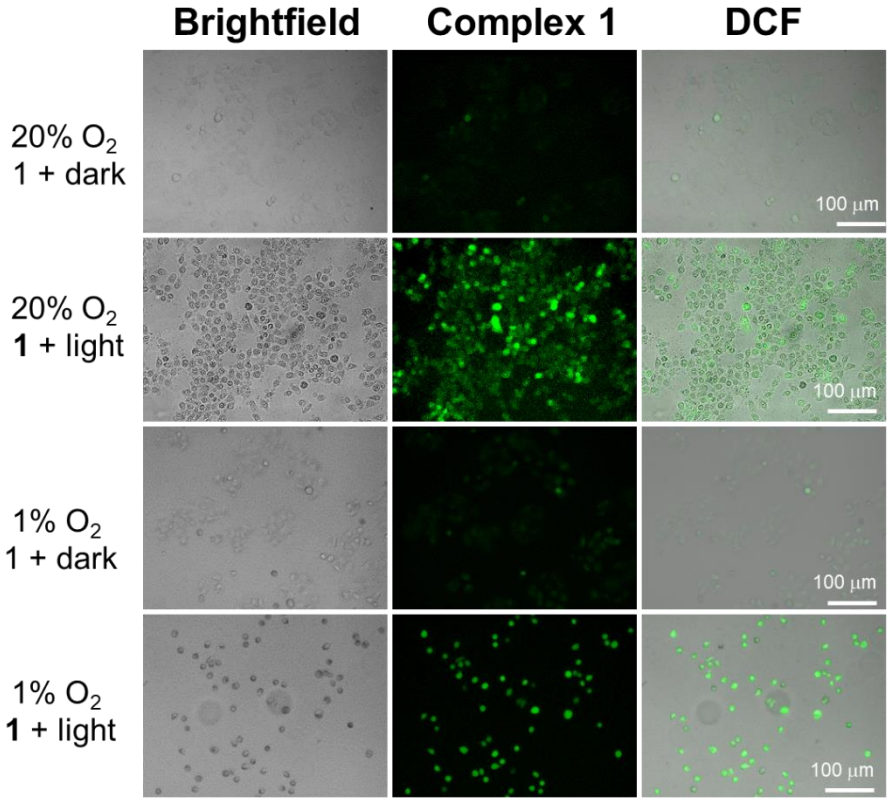

Supplementary Figure 31. Complex **1** generates ROS in A549 cancer cells after light irradiation under normoxia (3 μM, 2× light IC_{50}) and hypoxia (5 μM, 2× light IC_{50}). The cells were treated with complex **1** for 2 h, washed and then irradiated with 463 nm light under normoxia (20% O_2, 8.9 J/cm^2) and 450 nm light under hypoxia (1% O_2, 10.0 J/cm^2). After irradiation, cells were stained with DCFH-DA for 0.5 h at 310 K and then imaged by inverted fluorescence microscopy (Zeiss, Germany). Excitation wavelengths: 488 nm, emission filter: 520±20 nm. In the absence of light, the cells were not stimulated by complex **1** since only weak ROS signals could be observed. After light irradiation, complex **1** effectively generates ROS in A549 cancer cells under both normoxia and hypoxia. Non-fluorescent DCFH-DA is transformed into green fluorescent DCF after reaction with ROS in cells. These experiments were repeated three times independently with similar results.

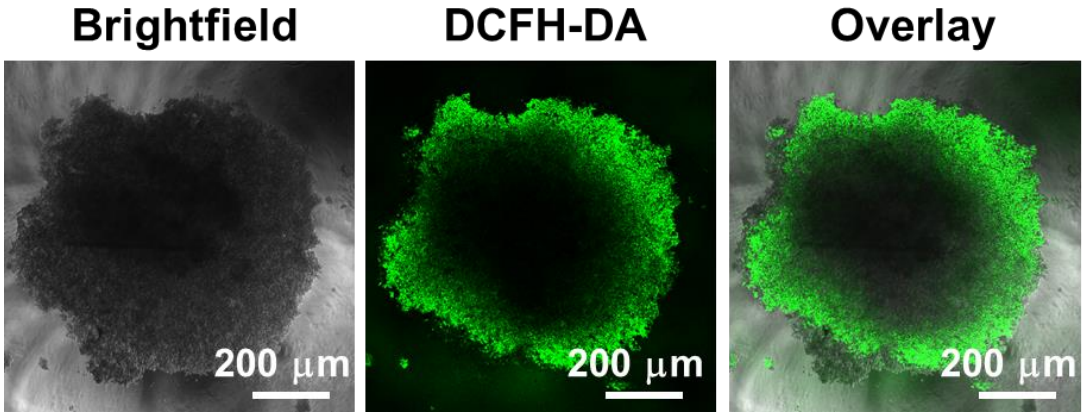

Supplementary Figure 32. ROS generation in multicellular A549 cancer spheroids (MCS) treated with complex **1** (2 μM) after two-photon light irradiation. Excitation wavelengths: complex **1** 760 nm; DCF 488 nm, emission filter: 565±20 nm (complex **1**), 520±20 nm (DCF). In contrast to the normal adherent cultured cancer cells, MCS are 3D cell aggregates which mimic the microenvironment of solid tumours *in vivo* (hypoxia core and nutrition gradient). The green ROS signal appeared only in the outer region of the spheroids, while became extremely low in intensity in the inner portion of A549 MCS, illustrating hypoxic core formation at the centre of the spheroids. These experiments were repeated three times independently with similar results.

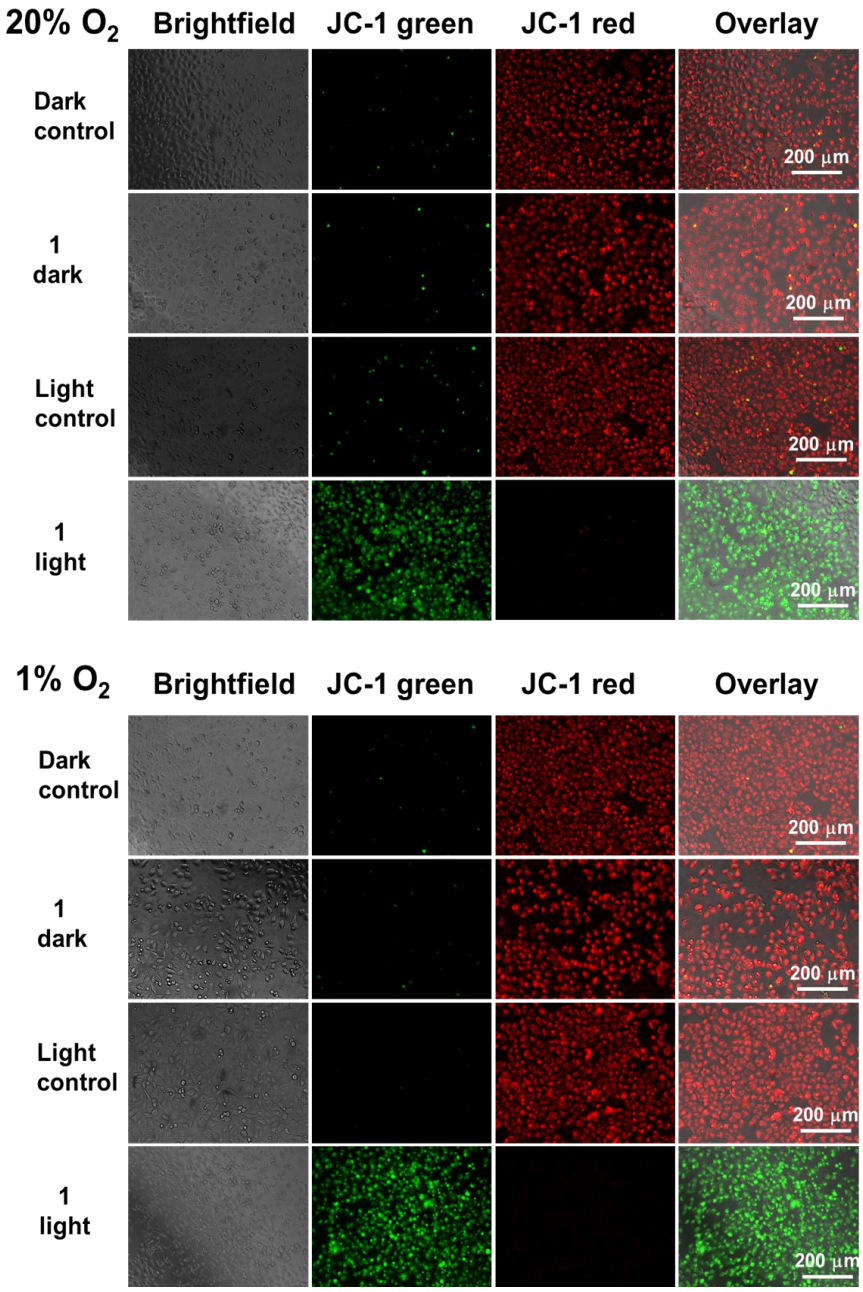

Supplementary Figure 33. Determination of mitochondrial membrane potentials for A549 cancer cells treated with complex **1** (2× IC_{50}, 3 μM under normoxia and 5 μM under hypoxia) for 2 h, which then received irradiation followed by staining with JC-1. The cationic dye JC-1 exhibits potential-dependent accumulation in mitochondria. At low MMP, JC-1 emits green fluorescence while at high MMP, the dye emits red fluorescence. After irradiation under normoxia and hypoxia, both normoxic and hypoxic cells treated with complex **1** emitted strong green fluorescence indicating significant mitochondria depolarization, while the cells without irradiation emit red fluorescence similar to the control (untreated) samples. JC-1 was excited at 488 nm with 530 nm and 585 nm bandpass emission filters. These experiments were repeated three times independently with similar results.

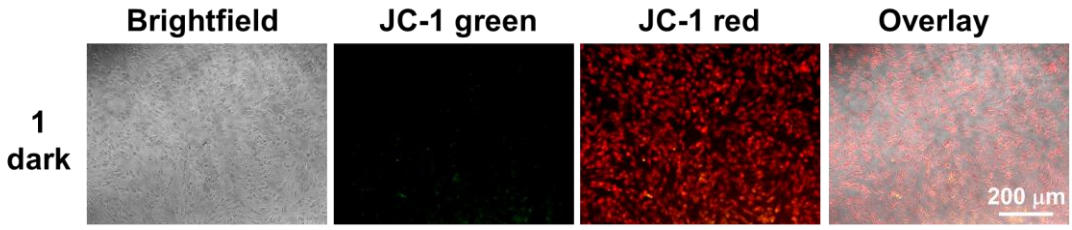

Supplementary Figure 34. Unaltered mitochondrial membrane potentials in MRC-5 normal cells on treatment with complex **1** in the dark, determined by JC-1 staining. MRC-5 normal cells were incubated with complex **1** (10 μM) under normoxia for 2 h followed by staining with JC-1. JC-1 was excited at 488 nm, with 530 nm and 585 nm bandpass emission filters. These experiments were repeated three times independently with similar results.

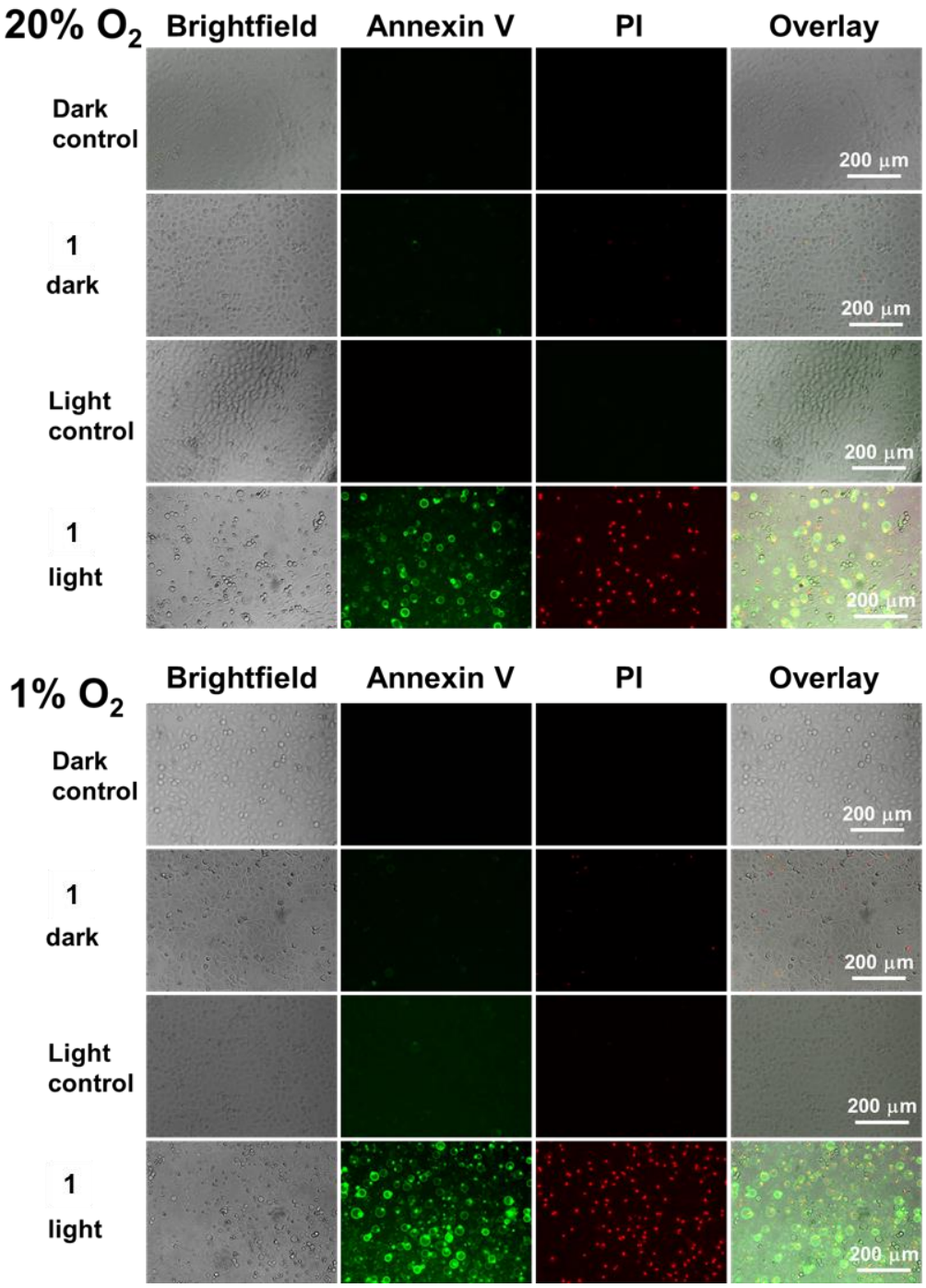

Supplementary Figure 35. Apoptosis of A549 cells under normoxia and hypoxia photo-induced by complex **1** detected by Annexin V/PI staining. A549 cancer cells were treated with complex **1** (2× light IC_{50}, 3 μM under normoxia and 5 μM under hypoxia) for 2 h, then washed, and irradiated under normoxia (20% O_2, 463 nm, 8.9 J/cm^2) or hypoxia (1% O_2, 450 nm, 10.0 J/cm^2), followed by recovery for 6 h. In the absence of light or drug treatment, no significant fluorescence was observed. After light irradiation, cancer cells growing under normoxia or hypoxia exhibited green and red fluorescence, indicating severe cell apoptosis and necrosis induced by complex **1**. These experiments were repeated three times independently with similar results.

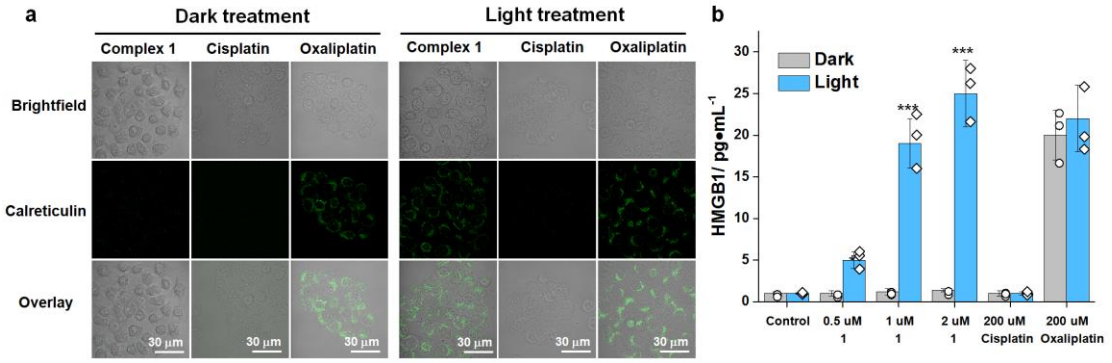

Supplementary Figure 36. Response to the immunogenic-apoptotic cell death mechanism in A549 cancer cells. Cells were treated with complex **1** (3 μM) or cisplatin (200 μM) or oxaliplatin (200 μM) at 310 K for 2 h, washed and irradiated with 450 nm light (10 J/cm^2) followed by recovery for 12 h. (a) Immunofluorescence of calreticulin was detected with Alexa Fluor 488-linked–calreticulin antibody. Excitation/emission: 488/520 nm. These experiments were repeated three times independently with similar results. (b) Enzyme-linked immunosorbent assay (ELISA) for high mobility group box 1 protein (HMGB1). The amount of HMGB1 released to the outside of the cells was detected by the HMGB1 ELISA kit. All the experiments were performed as duplicates of triplicates (n=6 biologically independent experiments). Error bars show ±1 s.d. from the mean. Statistics were calculated using the two-tailed t-test with unequal variances (Welch's unpaired t-test). $^{*}p < 0.05$, $^{**}p < 0.01$ $^{***}p < 0.001$. p values 0.5 μM (p = 0.0045), 1.0 μM (p = 0.0005), 2.0 μM (p = 0.0004).

References

1. Dolomanov, O. V. Bourhis, L. J. Gildea, R. J. Howard, J. A. K. & Puschmann, H. OLEX2: a complete structure solution, refinement and analysis program. *J. Appl. Cryst.* **42**, 339-341 (2009).

2. Bourhis, L. J. Dolomanov, O. V. Gildea, R. J. Howard, J. A. & Puschmann, H. The anatomy of a comprehensive constrained, restrained refinement program for the modern computing environment–Olex2 dissected. *Acta Cryst.* **A71**, 59-75, (2015).

3. Sheldrick, G. M. Crystal structure refinement with SHELXL. *Acta Cryst.* **C71**, 3-8 (2015).

4. Porras, J. A. Mills, I. N. Transue, W. J. & Bernhard, S. Highly fluorinated Ir(III)–2, 2′: 6′, 2″-terpyridine–phenylpyridine–X complexes via selective C–F activation: robust photocatalysts for solar fuel generation and photoredox catalysis. *J. Am. Chem. Soc.* **138**, 9460-9472 (2016).

5. Caspar, J. V. & Meyer, T. J. Photochemistry of tris 2, 2'-bipyridine ruthenium(2+)

ion $Ru(bpy)_3^{2+}$. Solvent effects. *J. Am. Chem. Soc.* **105**, 5583-5590 (1983).

6. Wang, J. & Hanan, G. S. A facile route to sterically hindered and non-hindered 4′-aryl-2,2′:6′,2″-terpyridines. *Synlett.* **8**, 1251-1254 (2005).

7. Liu, Z. *et al.* The potent oxidant anticancer activity of organoiridium catalysts. *Angew. Chem. Int. Ed.* **53**, 3941-3946 (2014).

8. Margoliash, E. & Frohwirt, N. Spectrum of horse-heart cytochrome c. *Biochem. J.* **71**, 570-572 (1959).

9. Matsuzaki, S. Kotake, Y. & Humphries, K. M. Identification of mitochondrial electron transport chain-mediated NADH radical formation by EPR spin-trapping techniques. *Biochemistry* **50**, 10792-10803 (2011).

10. Mari, C. *et al.* DNA intercalating Ru(II) polypyridyl complexes as effective photosensitizers in photodynamic therapy. *Chem. Eur. J.* **20**, 14421-14436 (2014).

11. Frisch, M. J. T. *et al.* Gaussian 16, Revision A. 03 (2016).

12. Rappoport, D. & Furche, F. Property-optimized Gaussian basis sets for molecular response calculations. *J. Chem. Phys.* **133**, 134105-134110 (2010).

13. Cronstrand, P. Luo, Y. & Ågren H. Generalized few-state models for two-photon absorption of conjugated molecules. *Chem. Phys. Lett.* **352**, 262-269 (2002).

14. Nayyar, I. H. Masunov, A. E. & Tretiak, S. Comparison of TD-DFT methods for the calculation of two-photon absorption spectra of oligophenylvinylenes. *J. Phys. Chem. C* **117**, 18170–18189 (2013).

15. Xu, C. & Webb, W. W. Measurement of two-photon excitation cross sections of molecular fluorophores with data from 690 to 1050 nm. *J. Opt. Soc. Am. B.* **13**, 481-491 (1996).

16. Baik, M. H. & Friesner, R. A. Computing redox potentials in solution: Density functional theory as a tool for rational design of redox agents. *J. Phys. Chem. A* **106**, 7407-7412 (2002).

17. Repiščák P. PhD Thesis, Heriot-Watt University (2017).

18. Isse, A. A. & Gennaro, A. Absolute potential of the standard hydrogen electrode and the problem of interconversion of potentials in different solvents. *J. Phys. Chem. B* **114**, 7894-7899 (2010).

19. Venkatesh, V. *et al*. Supramolecular photoactivatable anticancer hydrogels. *J. Am. Chem. Soc.* **139**, 5656-5659 (2017).

20. Huang, H. *et al.* Highly Charged ruthenium(II) polypyridyl complexes as lysosome‐localized photosensitizers for two-photon photodynamic therapy. *Angew. Chem. Int. Ed.* **54**, 14049-14052 (2015).

21. Huang, H. *et al*. Synthesis, characterization and biological evaluation of labile

intercalative ruthenium (II) complexes for anticancer drug screening. *Dalton Trans.* **45**, 13135-13145 (2016).

22. Liu, J. *et al.* Enhanced cancer therapy by the marriage of metabolic alteration and mitochondrial-targeted photodynamic therapy using cyclometalated Ir(III) complexes. *Chem. Commun.* **53**, 9878-9881 (2017).

23. Jin, C. *et al.* Rational design of NIR-emitting iridium (iii) complexes for multimodal phosphorescence imaging of mitochondria under two-photon excitation. *Chem. Commun.* **53**, 10374-10377 (2017).